MOLECULAR DYNAMICS

- INVESTIGATED BY PLASMON RULERS -

Dissertation
zur Erlangung des Grades
“Doktor der Naturwissenschaften”
im Promotionsfach Chemie

am Fachbereich Chemie, Pharmazie und Geowissenschaften
der Johannes Gutenberg-Universität Mainz

Laura Tüting

geb. in Bad Kreuznach

Mainz, 2017

D77 (Dissertation Johannes Gutenberg-Universität Mainz)

Tag der mündlichen Prüfung: 13.04.2018

ABSTRACT

Plasmon rulers consisting of two connected gold nanoparticles respond to molecular distance changes with a spectral shift in resonance wavelength accompanied with a total intensity change. Here, I introduce the use of plasmon rulers as a single-molecule technique for the elucidation of conformational and stiffness changes in single polymers and proteins. The equilibrium fluctuations of a molecule's extension are governed by intrinsic molecular properties. Monitoring plasmon ruler trajectories, I obtain the stiffness and extension of polyethylene glycol in varying salt concentrations of different cations. I observe a transition above about $1.2\,mM\,K^{+}$ ion concentration which is specific to potassium ions and does not occur in the presence of sodium ions. Further I investigate the conformational cycle of the molecular machine Hsp90. With the help of the plasmon ruler's unprecedented observation bandwidth, I detect a third state inaccessible with other methods. This new state is characterized by dwell times in the order of dozens of seconds which are rare events only occurring in 1 % of the cases. Further the influence of nucleotides on the protein is studied leading to a clear shift of the equilibrium.

ABSTRACT (GERMAN)

Das Plasmonenlineal bestehend aus zwei verbundenen Goldnanopartikeln reagiert auf molekulare Distanzänderungen mit einer spektralen Verschiebung der Resonanzwellenlänge, die mit einer Änderung der Gesamtintensität einhergeht. Hier stelle ich die Nutzung des Plasmonenlineals als Einzelmolekültechnik für die Aufklärung von Konformations- und Steifigkeitsänderungen in einzelnen Polymeren und Proteinen vor. Die Gleichgewichtsfluktuationen der Ausdehnung eines Moleküls sind von den intrinsischen Moleküleigenschaften bestimmt. Indem ich Trajektorien eines Plasmonenlineals beobachte, erhalte ich die Steifigkeit und die Ausdehnung von Polyethylenglykol in verschiedenen Salzkonzentrationen unterschiedlicher Kationen. Ich beobachte einen Übergang bei ungefähr $1.2\,mM\,K^+$ Ionenkonzentration, der spezifisch für Kaliumionen ist und nicht in Gegenwart von Natriumionen auftritt. Weiterhin untersuche ich den Konformationszyklus der molekularen Maschine Hsp90. Mit Hilfe der beispiellosen Beobachtungsbreite von Plasmonenlinealen detektiere ich einen dritten Zustand von Hsp90, der mit anderen Methoden nicht zugänglich ist. Dieser neue Zustand wird durch eine Verweildauer in der Größenordnung von Duzenden von Sekunden und durch sehr seltenes Auftreten der Ereignisse (nur in 1 % der Fälle) charakterisiert. Außerdem wird der Einfluss von Nukleotiden auf das Protein studiert, was zu einer klaren Änderung des Gleichgewichts führt.

Contents

List of Figures

List of Tables

1 INTRODUCTION

The static structure of most macromolecules and even proteins is solved on a routine basis in our days with the help of techniques like x-ray crystallography and NMR. However, the role of a biological macromolecule comes from its dynamics. Thus, the elucidation of the molecule's conformational dynamics is essential to understand its function. [1] Integrating over time or molecule ensembles is inherent in many measurement principles leading to averaging out of conformational dynamics. Monitoring one molecule at a time in so-called 'single-molecule-experiments' overcomes this issue. In the past years, single-molecule methods have shed light on protein function, e.g. optical tweezers, FRET (Förster or fluorescence resonance energy transfer). [2, 3]

About a decade ago, a new single-molecule technique called plasmon ruler emerged. [4] Here, the plasmonic properties of metallic nanoparticles are exploited. Light induces a collective oscillation of the conduction band electrons relative to the fixed positive metal ions in the metal nanoparticle leading to the plasmon resonance. When two plasmonic nanoparticles are brought into proximity their plasmons couple which results in a shift of the plasmon resonance in a distance-dependent manner. Assuming the distance between the particles is only influenced by a molecule linking the two particles, one can study dynamical processes by monitoring the plasmon resonance over time.

Plasmon rulers offer many advantages as an addition to the single-molecule toolbox. The scattering of plasmonic nanoparticles is, unlike fluorescent dyes, of indefinite lifetime due to the absence of blinking or bleaching in plasmonic light scattering. Plasmons show a higher photon flux than fluorescent probes or quantum dots. [5] Thus, a new observation bandwidth of single-molecules is accessible, including higher time resolution and longer observation time.

Plasmon rulers have not been used to the full extent possible as most studies focus on DNA. The main reason is that the functionalization and assembly of plasmonic nanoparticles with DNA is well-understood. [6, 7] In my thesis, I show the potential of plasmon rules to determine the cation-induced stiffness variations of a polymer and the elucidation of new dynamic conformational states of an important protein. With these purposes, I developed new reliable functionalization and assembly strategies to form single-molecule plasmon rulers without the need of DNA molecules.

An overview of the state of the art in single-molecule methods, the application of plasmon rulers and the physical chemistry of plasmon ruler fabrication is given in chapter 1. I will derive a new simple linear formula for plasmon ruler calibration for varying types of spectroscopic read-out as shown in chapter 2. Possible different routes for the assembly of plasmon rulers will be presented in chapter 3. Plasmon rulers as a single-molecule technique will be applied to different molecules: In chapter 4, DNA-Hairpins will be investigated; in chapter 5, I will show how plasmon rulers elucidate polymer dynamics under different salt conditions and in chapter 6, I will probe protein dynamics with plasmon rulers with the example of the molecular machine Hsp90.

1.1 COMMON SINGLE-MOLECULE METHODS HAVE LIMITATIONS

All single-molecule methods rely on an output signal generated by an intrinsic change of the molecule under investigation. To study the conformational dynamics of a molecule and obtain the kinetic constants that govern the process, we need to record the output signal continuously over time in so-called 'timetraces'.

The output signal depends on the measurement principle of the method. Here I describe the following single-molecule measurement principles: the patch-clamp technique in electro-physiology, force-spectroscopy methods (e.g. atomic force microscopy, optical or magnetic tweezers) and Förster resonance energy transfer.

1.1.1 PATCH-CLAMP TECHNIQUE IS ONLY APPLICABLE FOR MEMBRANE PROTEINS

The patch-clamp technique in electro-physiology was the first experimental single-molecule method able to study dynamic behavior of ion channels in cell membranes. The technique was developed by Nobel Laureates Erwin Neher and Bert Sakmann in the 1970s. [8, 9] A conformational change in a membrane protein functioning as an ion channel directly determines whether a specific ion can pass through the cell membrane (open conformation) or if it is trapped on one side of the cell membrane (closed conformation). The current through the membrane is dependent on the conformation of the ion channel and can, thus, be measured as output signal for the conformational change in the protein.

In order to study single membrane proteins, the cell membrane area under investigation has to be limited. A small patch of a cell membrane is isolated electrically by applying slight suction with a micro-pipette (see **Figure 1.1B**). [8] The current through the patch can be recorded over time with a resolution of up to 10 kHz. [9] In **Figure 1.1A** an example timetrace of current changes triggered by the conformational change in an ion channel dependent on acetylcholine is shown. Upon acetylcholine binding, the ion channel opens, resulting in a current change. The timetrace shows discrete current changes as expected for single molecules.

However, the patch-clamp technique is only suitable for the investigation of cell membrane proteins that induce a current change through the membrane upon conformational change. Hence, other techniques applicable in a more general context were developed.

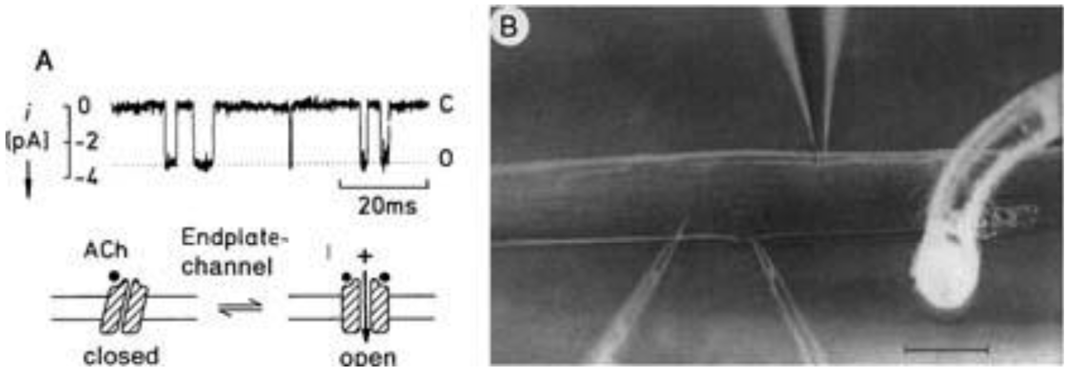

Figure 1.1: **Patch-clamp technique for single ion channels.** a) Individual ion channels open when ACh (acetylcholine) binds. Timetrace showing discrete current changes corresponding to conformational changes of one single ion channel. b) 'Patch pipette' sucking at the end-plate membrane of a frog muscle fiber in order to perform the patch-clamp current measurement. Figure reprinted with permission from [9]. © The Nobel Foundation 1991.

1.1.2 Force-Spectroscopy Does Not Investigate in Equilibrium

Force spectroscopy describes a set of techniques that investigate a single molecule by applying force to its ends and measuring the corresponding displacement. [10] Thus, force spectroscopy does not operate under equilibrium conditions because the molecule needs to be stretched. This non-equilibrium measurement of work can then be related to the equilibrium free energy difference according to the Jarzynski equality. [11]

The molecule under investigation is spanned between a surface and a probe. Force is applied to the molecule through the probe and the extension of the molecule is resolved by the position of the probe relative to the surface. Hence, the exact determination of the probe position is crucial, where the biggest source for measurement error is thermal drift.

Each force spectroscopy method uses a different probe. The most common ones are atomic force microscopy (AFM), optical tweezers and magnetic tweezers (see **Figure 1.2**). [10]

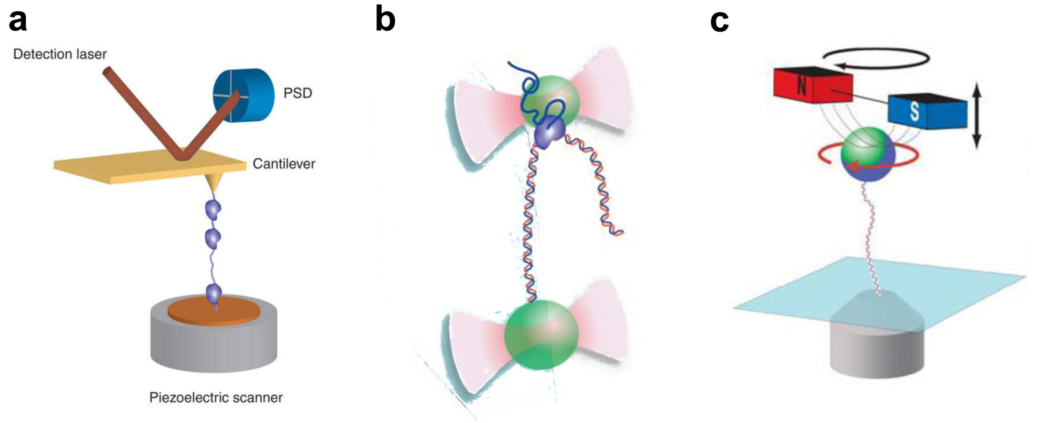

Figure 1.2: **Techniques for force spectroscopy.** a) In atomic force microscopy (AFM), a tip applies force on the molecule and the extension is detected by a position-sensitive detector (PSD) b) Optical tweezers pull the molecule tethered between two optically trapped microbeads apart. c) In magnetic tweezers the force to the molecule is generated by a magnetic field acting on a magnetic bead. Figure adapted with permission from [10].

For the utilization of an atomic force microscope in force spectroscopy, a single molecule needs to be attached with one end to the substrate and with the other end to the cantilever. The cantilever is then moved vertically (perpendicular to the imaging plane) pulling up the molecule. Although AFM is the technically simplest force spectroscopy method, it is more limited in the employable force range and, thus, not suitable for all biological applications.

Optical tweezers are the combination of two optically trapped microspheres. The molecule under investigation is tethered in between such two beads. Typically, one of the trapped beads is hold constant whereas the other trap moves pulling the molecule apart. The disadvantages are that the beads are in the micrometer range relatively big compared to the very small molecule (only a few nanometers) under investigation. Further, the beads need to be separated by hundreds of nanometers (above the diffraction limit), requiring very large linkers for the molecule. The laser intensities used for optical trapping induce local heating that can affect measurement accuracy and induce damage on the molecule under investigation. On the one hand, optical traps are the most versatile force spectroscopy tool, but on the other hand, they require the most challenging technical skills.

In magnetic tweezers the optical trap in optical tweezers is substituted by a magnetic trap avoiding heating and photodamage. Instead of a dielectric bead, the molecule under investigation is attached to a magnetic bead that can be manipulated by an applied magnetic field. Since magnetic tweezers rely on video-based displacement detection, they are not as sensitive to fast or small displacements than the other force spectroscopy techniques.

The first application of force spectroscopy methods was the mechanical unfolding of Titin, a muscle protein, demonstrated by AFM and optical tweezers. [12, 13] Both methods show a typical 'sawtooth' pattern in their force-extension curves. First, the force increases linearly with the extension of the molecule until a rupture (in the structure of the molecule) occurs, decreasing the force. This process is repeated several times until the molecule is completely unfolded. This type of measurement gives insight in the folding landscape of the protein. Recently also the hidden dynamics at a constant applied force have been investigated more carefully. [14]

1.1.3 FRET HAS LIMITED OBSERVATION BANDWIDTH

In contrast to force spectroscopy, single molecule FRET operates under equilibrium conditions. FRET stands for Förster resonance energy transfer, a non-radiative dipole-dipole-coupling between fluorescent dyes. [15, 16, 17] The molecule under investigation needs to be labeled with two different dyes, a donor and an acceptor dye. If the two dyes are further apart than the Förster radius, only the donor dye will be excited. The closer the two dyes get in respect to each other, the more light is emitted by the acceptor dye and the less light can be collected from the donor channel (see **Figure 8.2**).

The distance decay follows an inverse sixth power relationship, generally limiting the observation range to approximately 10 nm. [18] As FRET relies on fluorescent dyes, that are prone to bleaching, the overall absolute observation time is limited to a few minutes. Thus, to get reasonable single-molecule data, many different molecules need to be investigated and there is a need of averaging.

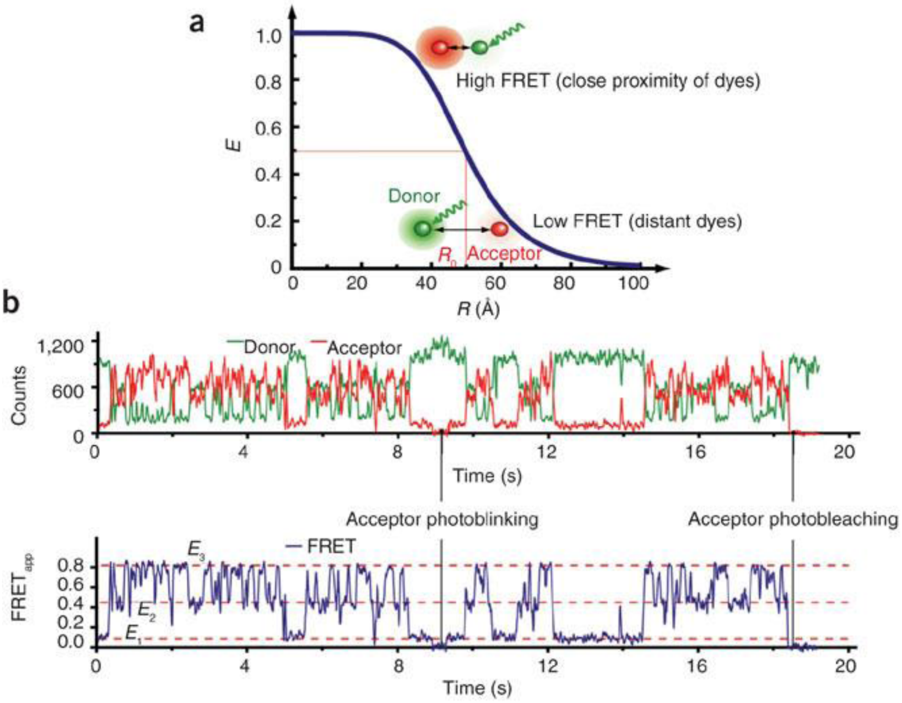

Figure 1.3: **Single molecule FRET.** a) FRET efficiency as a function of inter-dye distance. The fluorescence that is transferred from donor to acceptor dye decreases with increasing inter-dye distance. b) .Example of a single-molecule FRET timetrace where the molecule alternates in between three distinct conformations, also photo-blinking and photo-bleaching is observed. Figure reprinted with permission from [18].

1.2 PLASMON RULERS CAN OVERCOME DRAWBACKS

Plasmon rulers rely on the principle of plasmon coupling between two plasmonic nanoparticles. [19, 20] The closer two plasmons get in respect to each other, the stronger their coupling efficiency becomes shifting the resonance wavelength of the particle pair to lower energies ('red-shift'). In order to prepare a molecular ruler taking advantage of plasmon coupling, a molecule needs to be labeled with two plasmonic nanospheres on its opposite ends. Thus, the resonance wavelength of the ruler as optical readout depends solely on the extension of the molecule. If this molecule shrinks (or enlarges), the plasmon coupling between the two spheres will be enhanced (or decreased), shifting the resonance wavelength to lower energies (or to higher energies), respectively.

The plasmon ruler is a single-molecule technique operating in equilibrium, unlike the force spectroscopy methods described in **Section 1.1.2**, and is, thus, more comparable to the patch-clamp technique and single-molecule FRET (see **Section 1.1.1** and **Section 1.1.3**, respectively). Patch-clamp is superior to FRET in respect to the longer observation time and higher time resolution because the fluorescent dyes in FRET bleach after a few minutes. FRET out-competes patch-clamp with regards to versatility, since patch clamp can only be applied to ion channels in cell membranes, whereas almost any (bio)molecule can be labeled with two fluorescent dyes for FRET. Plasmon rulers are as versatile as FRET concerning the labeling strategies and offer comparable observation times to patch-clamp, in view of the unlimited lifetime of plasmons as labels.

In this chapter, I will give a brief literature review about what has been studied with plasmon rulers. The previous studies can be separated into two main subjects: one is concerning DNA dynamics and the other one is about plasmon ruler applications in cell studies.

1.2.1 PLASMON RULERS CAN ELUCIDATE DNA DYNAMICS

Plasmon rulers as a dynamic single-molecule technique have been demonstrated experimentally for the first time in 2005. [4] Here, a single strand of DNA was linked to two nanospheres comprising a plasmon ruler. The assembly procedure is shown in **Figure 1.4A**. First, streptavidin coated nanospheres were immobilized in a microfluidic flow cell. These monomeric particles appear greenish under dark-field illumination (see left image in **Figure 1.4B**). Next, nanospheres functionalized with biotinylated DNA are reacted with the monomers forming dimers that appear orange in dark-field (see right image in **Figure 1.4B**). The dimer formation process can be monitored by collecting single particle dark-field scattering spectra. Upon dimer formation the resonance wavelength is shifted to higher wavelength compared to single nanospheres (see **Figure 1.4C**). The formed dimers can be utilized as plasmon rulers because the interparticle distance is defined by the DNA extension.

If single-stranded DNA is incubated with another complementary single strand of DNA, the two strands will hybridize leading to a length extension. This process can be probed by the scattering spectrum of a single plasmon ruler as shown in **Figure 1.4D**. The spectrum in red corresponds to a plasmon ruler linked with single-stranded DNA whose resonance wavelength is shifted to lower wavelength upon incubation with a complementary DNA strand. This 'blue-shift' is attributed to an increase in interparticle distance stemming from the enlargement of the DNA after double-strand formation.

Dynamic reversible DNA extension changes could be observed qualitatively by recording a time series of the resonance wavelength of a plasmon ruler in different salt environments. In a higher salt concentration the DNA shrinks due to a reduced Debye screening length indicated by a red-shift of the plasmon ruler resonance wavelength. When changing to a lower salt concentration the DNA enlarges leading to higher inter-particle distance and, thus, a blue-shift of the resonance wavelength. This is the proof-of -principle for reversible dynamic distance changes probed by plasmon rulers.

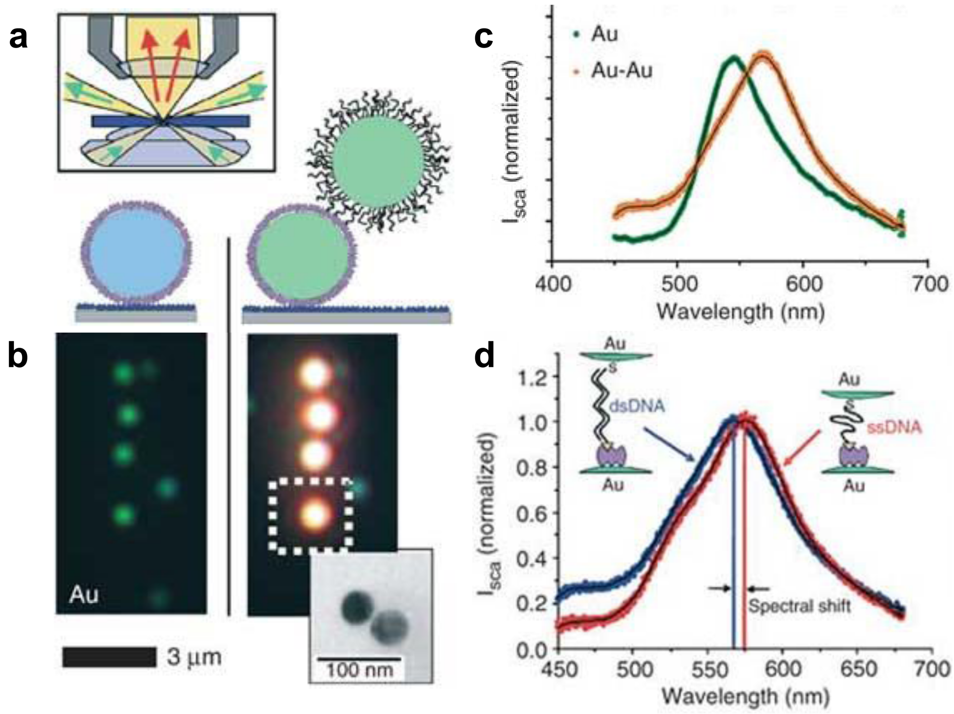

Figure 1.4: **Plasmon ruler for DNA hybridization.** a) Scheme of the assembly for DNA linked plasmon ruler. The first nanosphere is coated with Streptavidin and immobilized. Then the second particle functionalized with DNA-biotin is linked to the first nanoparticle. b) Real color images obtained by dark-field microscopy of single nanospheres (left) and dimers (right). c) Normalized scattering spectra of a single nanosphere (green) and a dimer (orange). d) Normalized scattering spectra of a plasmon ruler linked with single-stranded DNA (red) and a plasmon ruler linked with double-stranded DNA (blue). Figure reprinted with permission from [4].

The concept of the single-stranded DNA plasmon ruler is useful for additional applications. One example is the investigation of DNA cleavage by restriction enzymes. [6] In **Figure 1.5A**, I show a sketch of the interaction of a restriction enzyme with a plasmon ruler linked by a single DNA strand. First the enzyme binds unspecifically to the DNA, until the enzyme sticks to its specific DNA recognition site. The enzyme bends the DNA and then cleaves the strand. After cleavage the enzyme falls off the strand and the now loose nanosphere is removed. These events can be probed by the intensity time series of the plasmon ruler (confer to **Figure 1.5B**). The bending of the DNA reduces the inter-particle distance resulting in a slight intensity increase. The cleavage of the DNA can be read out by a large intensity drop since the plasmon ruler gets rid of one particle.

Similar implementation of plasmon rulers were used to investigate the cleavage of RNA by ribonuclease [21], the bending of DNA due to the binding of transcription factors [22], DNA elongation by telomerase [23] and peptide cleavage by caspase [24, 25].

Another interesting study was conducted using plasmon rulers for measuring the stiffness of single-stranded and double-stranded DNA. [7] The extend of a molecule's temporal length fluctuations determines its stiffness. The length fluctuations can be probed by spectral fluctuations of plasmon rulers. The more the spectral response varies over time, the less stiff is the molecule. In **Figure 1.5C**, we see sketches of a DNA plasmon ruler's equilibrium fluctuations (left) and the probability distribution of the inter-particle separation (right) of multiple types of DNA. The probability distribution is transformed in an extension potential that can be described by the Hookean model. The stiffest extension potential (orange) corresponds to double-stranded DNA of 30 base pairs, the medium potential (green) stems form double-stranded DNA of 52 base pairs and the softest potential (blue) is attributed to DNA comprised of single-stranded (40 base pairs) and double-stranded DNA (60 base pairs).

The previous studies found in literature presented here show the potential of plasmon rulers for detection of bending, elongation and cleavage of biomolecules such as DNA, RNA and peptides.

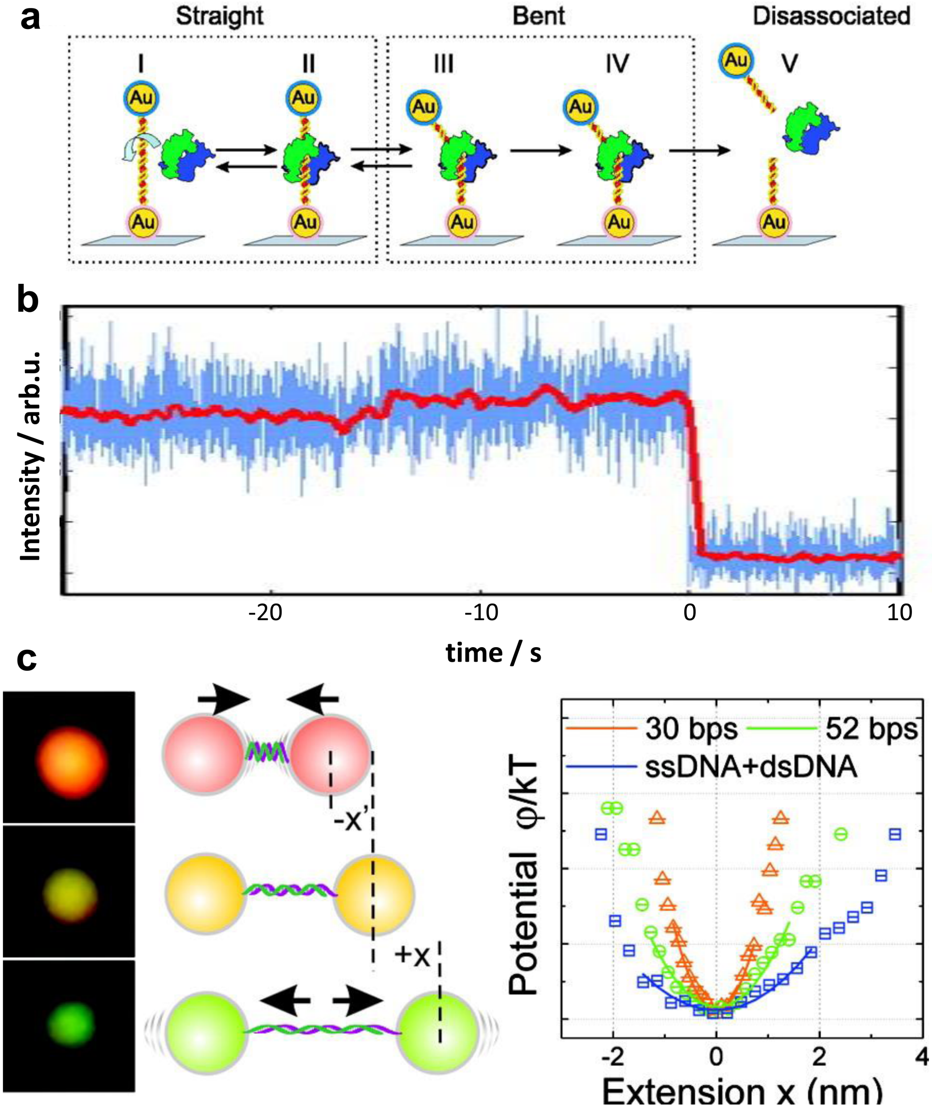

Figure 1.5: **Plasmon ruler for DNA bending and cleavage.** a) Sketch of the interaction of a restriction enzyme with single-stranded DNA linking a plasmon ruler. First the enzyme binds to the DNA, then bends and lastly cleaves the DNA. b) Timetrace showing DNA bending by an increase of intensity and DNA cleavage by a decrease in intensity. c) The amplitude of the time-dependent intensity fluctuations of DNA plasmon rulers can be related to DNA stiffness. Figure adapted with permission from [6, 7].

1.2.2 Plasmon Rulers Are Useful for Cell Studies

Single protein detection is achieved on individual nanorods for a protein of 450 kDa. [26] However, most proteins excreted by cells are of lower molecular weight, e.g. the matrix metalloproteinase 3 (MMP-3) with 54 kDa. Aptamers are an alternative to antibodies comprised of DNA that specifically bind certain target molecules. [27] The aptamer for MMP-3 undergoes a conformational change upon protein binding. Constructing a plasmon ruler where the aptamer is sandwiched between two nanospheres, the conformational change will result in a reduced inter-particle distance and a corresponding red-shift of the plasmon resonance wavelength (see **Figure 1.6A**). The plasmon ruler's resonance wavelength is monitored as a time series shifting to higher wavelength when the protein is present and shifting to lower wavelength when the protein is absent. The sensor reacts to the target within 1 s and reversibility is achieved within the same time.

This plasmon ruler as binding sensor is further applicable to detect excreted MMP-3 in the proximity of a cell. The plasmon resonance wavelength of a population of plasmon rulers is detected near a cell that is expressing MMP-3 (see **Figure 1.6B**) and in proximity to a cell with MMP-3 knocked down (see **Figure 1.6C**). The real-color images resulting from dark-field illumination visualize the color change of the plasmon ruler in the presence of secreted MMP-3 from yellowish orange to orange. The color change is due to the reduced inter-particle separation provoked by the conformational change in the aptamer upon protein binding. Quantitatively, the probability distributions of the plasmon resonance wavelength of the individual plasmon rulers shows a red-shift of 10 nm for a cell secreting MMP-3 compared to the knocked down cell. The magnitude of the spectral shift for a single protein is increased 30-fold compared to plasmonic sensing on nanorods and, thus, more conveniently detected in cellular environments. [26] In the future, it would be worthwhile to actually determine excreted protein levels in response to drug targets in real time.

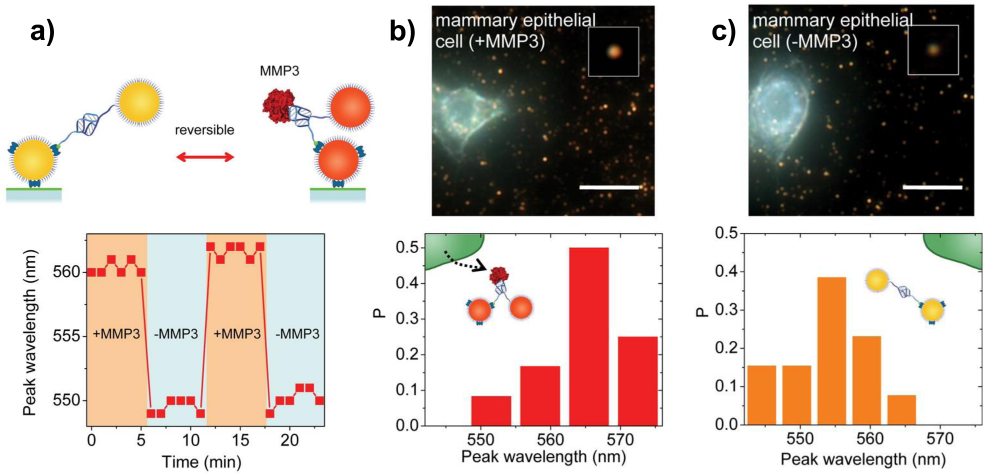

Figure 1.6: **Plasmon ruler for single-protein detection in cells.** a) Sketch of a plasmon ruler linked with an aptamer undergoing a conformational change upon binding of a single protein. Resonance wavelength of a plasmon ruler displayed over time while a solution containing the target protein and buffer is alternated showing reversibility of the sensor. b,c) Real-color images of plasmon rulers in proximity to a cell expressing the target protein (b, top) and not expressing the target (c, top) and the corresponding probability distribution of the plasmon resonance wavelength (bottom). Figure adapted with permission from [28].

The resolution in particle tracking is restricted by the diffraction limit. Since plasmon coupling occurs well below this limit, it is possible to visualize sub-diffraction limit encounters of nanoparticles by plasmon coupling. [29] Integrin surface receptors diffuse freely in 2D across the cell membrane. Plasmonic nano-spheres functionalized with antibodies can label the surface receptors and be utilized to track receptor diffusion. If two receptors co-localize while diffusing, their plasmonic labels will couple resulting in a red-shift of the plasmon resonance wavelength.

Tracking multiple nanospheres with full spectral resolution is difficult to achieve in the time frame of diffusing particles. Therefore, the imaging process is reduced to two wavelength (see **Figure 1.7A,B**). If a receptor labeled with a nanosphere is single within the plasmon coupling range, the lower wavelength (530 *nm*) will show the highest relative intensity (as in **Figure 1.7A**). In contrast, when two labeled receptors co-localize on the cell membrane, the higher wavelength (580 *nm*) will have the highest relative intensity (as in **Figure 1.7B**).

A time series with two illumination channels of receptor diffusion on a cell membrane is shown in **Figure 1.7C**. First the receptors are single and then co-localize below the diffraction limit.

The plasmon coupling tracking microscopy has further been applied to study cell membrane confinement [30], co-localization of epidermal growth factor receptors [31] and co-localization of different types thereof [32].

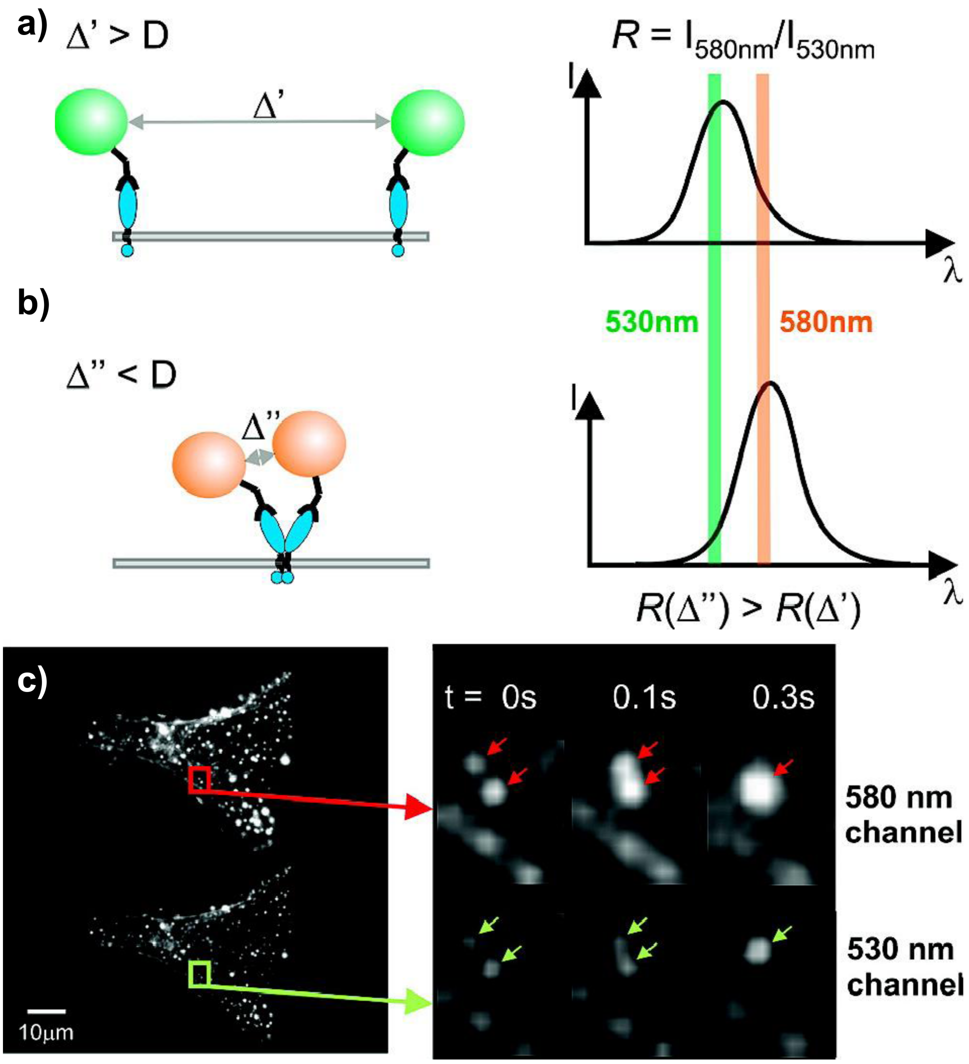

Figure 1.7: **Plasmon ruler for analyzing co-localization of cell membrane receptors.** a,b) Sketch of cell receptors labeled with nanospheres (left) and corresponding scattering spectra (right). When the membrane receptors are separated above the plasmon coupling distance the resonance wavelength seen in the scattering spectrum is blue-shifted (a) compared to co-localized membrane receptors (b) where the plasmon coupling leads to a red-shift of the plasmon resonance wavelength. c) Image of a cell whose membrane receptors are labeled with nanospheres. A time series recorded simultaneously with two illumination wavelengths: 580 *nm* (top) and 530 *nm* (bottom) visualizes the diffusion of two particles that eventually co-localize on the cell membrane. Figure adapted with permission from [29].

1.3 INTER-PARTICLE FORCES CAN BE DESCRIBED BY DLVO-THEORY

The colloidal stability of a nanoparticle is ensured if the attractive forces between individual nanoparticles outweigh the repulsive forces. The main theory used to describe inter-particle forces is the DLVO-theory (named after Derjaguin, Landau, Verwey and Overbeek). [33, 34]

The attractive inter-particle forces are attributed to van-der-Waals interactions (instantaneous dipole-induced dipole forces). The van-der-Waals potential between two spherical particles has been derived by Hamaker with the radius of the two spheres r_1 and r_2, the center-to-center distance z and the material-dependent Hamaker-constant A_H. [35]

$$E_{vdW} = -\frac{A_H}{6}\left(\frac{2r_1r_2}{z^2-(r_1+r_2)^2} + \frac{2r_1r_2}{z^2-(r_1-r_2)^2} + \ln\left[\frac{z^2-(r_1+r_2)^2}{z^2-(r_1-r_2)^2}\right]\right) \tag{1.1}$$

If the inter-particle distance d is much smaller than the radius of the particles ($d \ll r_1$ or $d \ll r_2$), the potential description can be simplified.

$$E_{vdW} = -\frac{A_H}{6}\left(\frac{r_1r_2}{r_1+r_2}\right)\frac{1}{d} \tag{1.2}$$

Assuming both nanospheres have the same radius r, the formula reduces further.

$$E_{vdW} = -\frac{A_H}{12}\frac{r}{d} \tag{1.3}$$

For gold nanospheres, the Hamaker.constant is commonly set to $A_H = 2.5 \cdot 10^{-19}\ J$. [36] Thus, the van-der-Waals potential only depends on the radius of the nanosphere. In **Figure 1.8**, I show exemplary potentials for nanospheres with diameters of 40, 50 and 60 nm. The potential energy increases with increasing radius of the nanospheres and for all sizes the energy increases with decreasing inter-particle distance. Hence, two nanoparticles approaching each other will fall into a potential well and will irreversibly bind to each other, if not avoided by additional repulsion.

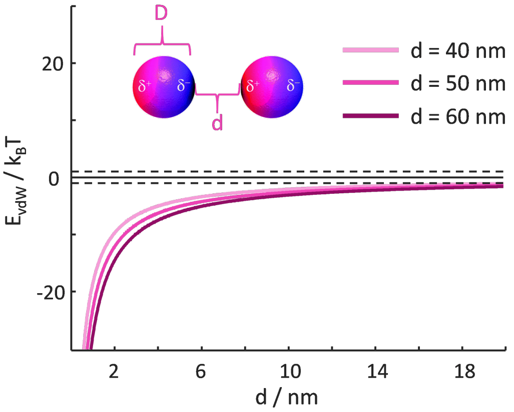

Figure 1.8: **Van-der-Waals potential for gold nanospheres.** The potential energy described as van-der-Waals interaction between two gold nanospheres (inset showing the induced dipoles) against the inter-particle distance for nanospheres with a diameter of 40 *nm* (light pink), 50 *nm* (medium pink) and 60 *nm* (dark pink). The black dashed lines represent the thermal energy of $\pm 1\ k_B T$. Sketch of the particle pair reprinted with permission from [37].

Electrostatic repulsion hinders the approach of two like-charge nanoparticles. The repulsive potential energy E_{rep} depends on the radius of the nanosphere r, the inter-particle distance d, the absolute salt concentration c_0, the Debye length κ and the scaled surface potential of the nanoparticles γ.[38, 39]

$$E_{rep} = \frac{64\pi k_B T c_0 \gamma^2 r}{\kappa^2} \exp\left(-\kappa d\right) \tag{1.4}$$

The Debye length κ is characterized by the absolute concentration of the ions in solution c_i and their respective valencies z_i.

$$\kappa = \frac{\sum_i \left(z_i e\right)^2 c_{i,0}}{\epsilon\epsilon_0 k_B T} \tag{1.5}$$

For mono-valent ionic solutions ($z_i = 1$) we can derive a shorter formula for the Debye length. Taking into account all the constants, the Debye length only depends on the concentration of the salt solution c.

$$\kappa = \frac{\sqrt{c}}{0.304\ nm\sqrt{\frac{mol}{L}}} \tag{1.6}$$

The scaled surface potential γ depends on the surface potential of the nanoparticle Ψ_0, that is approximately equal to a parameter accessible by measurement, the ζ-potential. [40, 41]

$$\gamma = \tanh\left(\frac{ze\Psi_0}{4k_BT}\right) \tag{1.7}$$

All in all, the repulsive potential mainly depends on the ionic strength of the surrounding medium as shown in **Figure 1.9A** and on the ζ-potential as shown in **Figure 1.9B**. The ions dissolved in the surrounding medium of the nanoparticles screen the surface charges of the particles. The higher the ionic strength of the solution, the shorter the distance until the repulsion potential gets negligible. For higher ζ-potential of the nanoparticles, the screening of the surface charges takes place at longer distances.

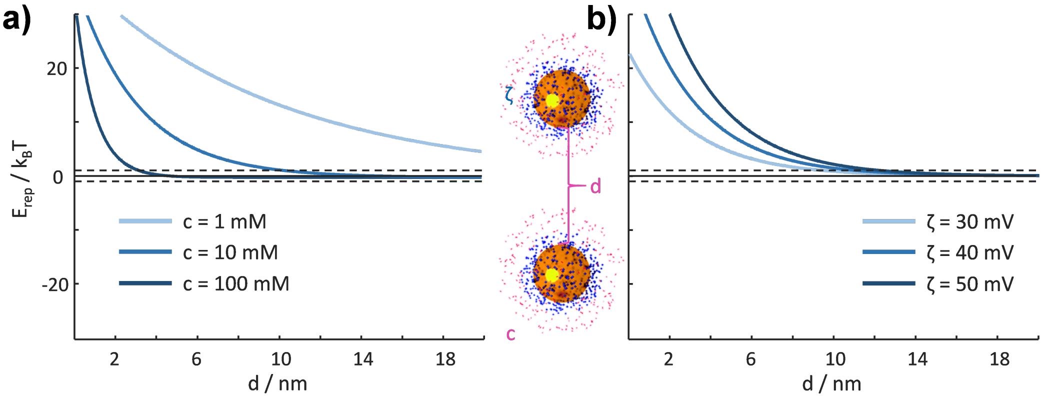

Figure 1.9: **Repulsive potential for gold nanospheres.** The potential energy described as repulsive interaction between two gold nanospheres with diameters of 50 nm (inset showing the charge clouds of the particles with their respective screening from free ions of the solution) against the inter-particle distance. a) The repulsive energy for varying concentration of a mono-valent salt concentration of 1 mM (light blue), 10 mM (medium blue) and 100 mM (dark blue) at fixed ζ-potentials of nanoparticles with 40 mV. b) The repulsive energy for varying ζ-potentials of nanoparticles with 30 mV (light blue), 40 mV (medium blue) and 50 mV (dark blue) at a fixed salt concentration of 10 mM. The black dashed lines represent the thermal energy of $\pm 1\ k_BT$.Sketch of the particle pair adapted with permission from [37].

According to DLVO-theory, the total interaction potential E_{tot} between two nanoparticles is the sum of the attractive (van-der-Waals) potential E_{vdW} and the repulsive potential E_{rep}. [33, 34]

$$E_{tot} = E_{vdW} + E_{rep} \tag{1.8}$$

In **Figure 1.10**, I show the total energy potential (violet) as the sum of the attractive energy (pink) and the repulsive energy (blue). We observe a primary minimum for the total energy at short inter-particle distances followed by a potential barrier and a secondary minimum. If the thermal energy of nanoparticles is lower than the potential barrier, aggregation of nanoparticles is unlikely.

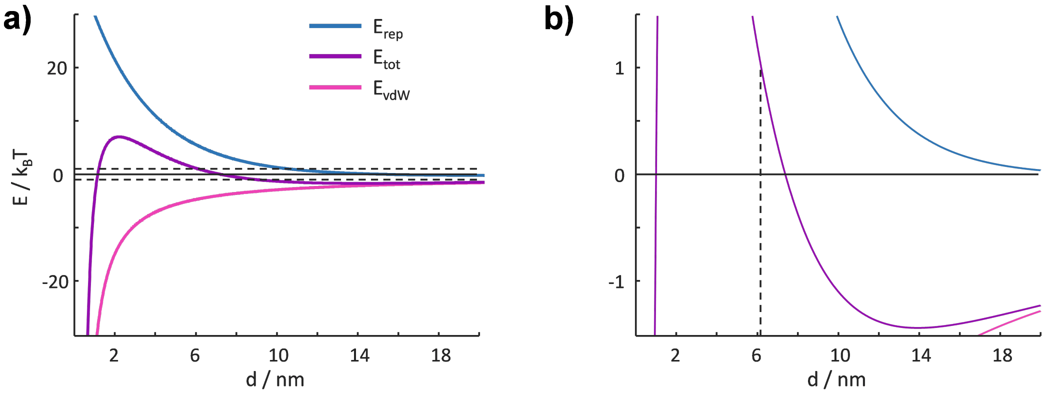

Figure 1.10: **Total potential for the interaction of gold nanospheres.** a) The total energy (violet) described as the sum of the repulsive (blue) and the attractive (pink) interactions between two gold nanospheres against the inter-particle distance for a particle pair with a diameter of 50 nm with a ζ-potentials of nanoparticle surface of 40 mV dissolved in solution with a salt concentration of 10 mM. For interparticle distances above 6 nm the potential lies within the thermal energy of ± 1 $k_B T$ (represented by the two dashed black lines). b) The same values as in a) are shown as a zoom-in.

So far, I have only considered the energy contributions from classical DLVO-theory, the attractive van-der-Waals-energy and the repulsive electrostatic energy. However, it is possible to stabilize nanoparticles against the attractive energy with other sources of repulsion, e.g. steric or electro-steric. [37]

Steric repulsion is achieved by grafting a polymer layer to the surface of each nanoparticle. Due to steric hindrance the nanoparticles are repelled from each other and can not get close enough avoiding aggregation. This repulsion is entropic, since two approaching polymer chains reduce the degree of freedom of each other. [42]

Electro-steric stabilization is achieved by taking advantage of both repulsion effects, steric and electrostatic. Therefore, polymer chains containing charged groups are grafted to nanoparticles.

The nanospheres used in this work for plasmon rulers are mainly stabilized due to steric repulsion. The plasmon ruler technique is only practicable for inter-particle distance above $6\,nm$ because if the particles come closer together they will irreversibly stick. The plasmon ruler is supposed to be a force-free technique, thus, this minimum distance should be ensured. A $3\,nm$ functionalization layer on either of the two particles forming the dimer would be enough. In this work, the PEG and also the DNA ligands exceed this limit enabling the investigation under force-free conditions.

2 PLASMON COUPLING IS QUANTIFIED BY THE SENSITIVITY OF DISTANCE *L*

Coupling of plasmons can be described by the plasmon hybridization model in analogy to the hybridization of atomic orbitals in molecules. [43] When two metal nanoparticles are brought into proximity their plasmon modes hybridize, leading to a lower energy bonding plasmon mode (red-shift of the resonance wavelength).

The red-shift of the bonding plasmon mode increases almost exponentially with decreasing inter-particle distance. [19, 44] This relationship can be exploited to determine the inter-distance from the plasmon resonance wavelength of a particle pair.

However, from the used formula so far, it is not intuitive to directly estimate the expected shift in the resonance wavelength for a given change in inter-particle distance, caused e.g. by a length change in the molecule linking the particles (plasmon ruler).

Here I derive a new simple formula defining a sensitivity of the particle pair for the length change of a molecule, I call L. I form the first derivation of the exact exponential description for the relationship and linearize it. Thus, one needs to simply divide the resonance wavelength shift of the particle pair by the factor L to deduce the length change of an investigated molecule.

This new simple formula can be easily and fast used for calculating molecular length changes. Using only a proportionality factor will help to open the way for the technique of plasmon rulers employed for single-molecule studies to a broader audience, e.g. to biochemical laboratories.

2.1 THERE ARE THREE SPECTROSCOPIC READ-OUT METHODS FOR PLASMON RULERS

The shrinking of a linker connecting a plasmon ruler leads to a shorter inter-particle distance and, thus, to higher resonance wavelength ('red-shift') and an increase in absolute intensity due to stronger coupling efficiency. There are three different ways to determine the interparticle distance spectroscopically (see **Figure 2.1**):

1. Determination of the resonance wavelength
2. Determination of the change in an intensity ratio
3. Determination of the change at a single wavelength

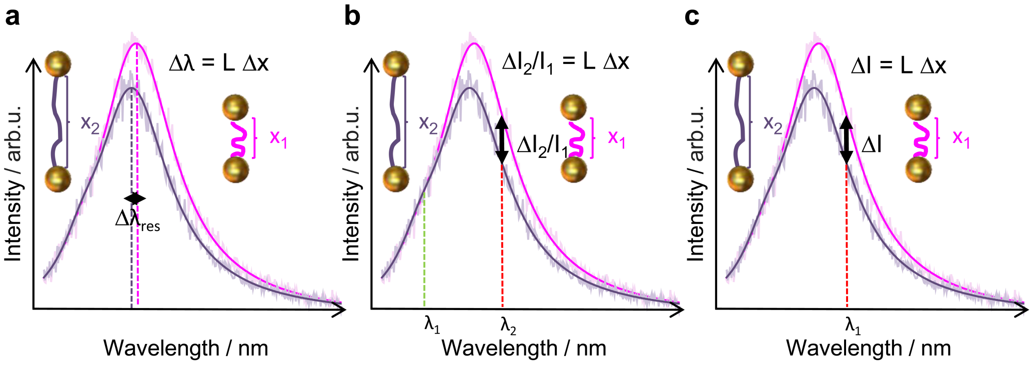

Figure 2.1: **Spectroscopic methods to determine interparticle distance.** a) Resonance wavelength method. The difference of the resonance wavelength of the stretched (left) and shrunk (right) dimer is proportional to the inter-particle distance. b) Dual-wavelength method. One wavelength (green) does not change during linker dynamic and can, thus, serve as internal reference correcting instrumental drift. The other wavelength (red) increases with decreasing interparticle distance. The change in the ratio of the two normalized wavelength is proportional to the distance. c) Single-wavelength method. The reference wavelength can be omitted for drift-free measurements and the absolute intensity is used to convert to distance changes.

In order to monitor the time-dependent dynamics of the molecule I need to record the resonance wavelength or the intensity of a single dimer over time, measuring a so-called timetrace. In **Figure 2.2**), I compare the spectroscopic readout of both methods investigating a similar plasmon ruler. The resonance wavelength shift detection is performed in a conventional single particle dark-field microscope acquiring spectra over time of one single particle at a time. [27, 45] The intensity time-trace was collected with the help of a spectral imaging setup, where many of such timetraces can be collected in parallel (brief description of the setup in Appendix **Section 8.1**). [*]

Both methods are suitable to visualize the distance change of a molecule while it continuously reversibly shrinks and expands. However, the noise level of the intensity method is lower than that of the resonance wavelength method as can be seen by comparing the histograms in **Figure 2.2**. The bisected histogram from the wavelength method (**Figure 2.2A**) is masked by setup noise more pronounced than that measured by the intensity method (**Figure 2.2B**).

Considering the advantages of intensity-based detection, lower noise level and parallel recording of many timetraces improving the statistical quality of the plasmon ruler as a single-molecule method, the main results in this work were obtained by measuring spectral imaging timetraces.

---

[*] The setup was developed by Weixiang Ye

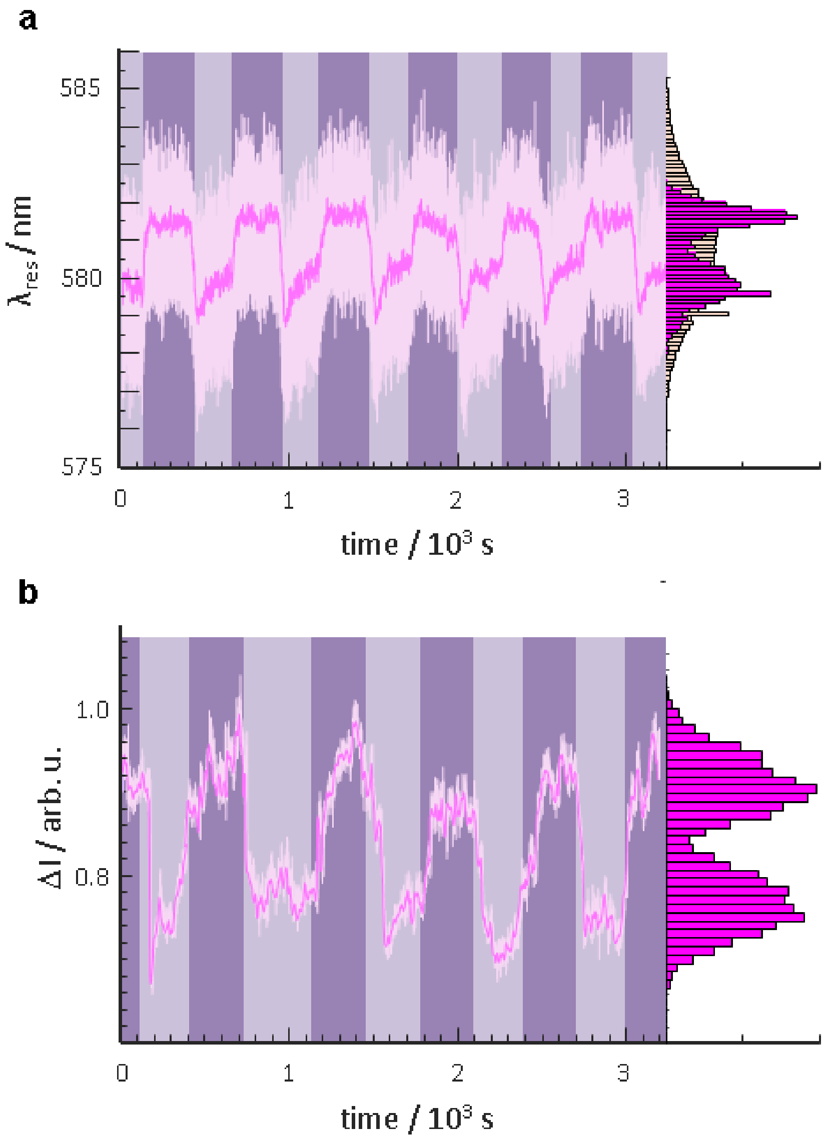

Figure 2.2: **Comparison of dynamic plasmon ruler investigated with full spectral resolution and with intensity detection.** a) Monitoring the resonance wavelength of a plasmon ruler while a molecule is altered continuously between shrunk (dark-colored regions) and stretched (light-colored regions) conformation clearly resolves the two conformations b) The same experiment was repeated only detecting the intensity change at a specific wavelength leading to similar results, but less noisy data visualized in the higher separation of the histogram b) compared to a).

2.2 Plasmon Coupling Can Be Described as an Exponential Decay

The distance-dependency of the inter-particle separation of two nanoparticles has been probed experimentally. In one experiment, nanodisks were lithographically created with varying separations (see **Figure 2.3A**). [19] Here a universal exponential decay could be fitted when the resonance wavelength shift was plotted against the fraction of inter-particle separation divided by the nanodisk diameter.

Another study showed a similar exponential decay function by linking nanospheres with DNA of varying length (see **Figure 2.3B**). [44] This relationship is well-described also by the universal scaling law suggesting that also flexibly linked plasmon rulers can be calibrated with an exponential decay.

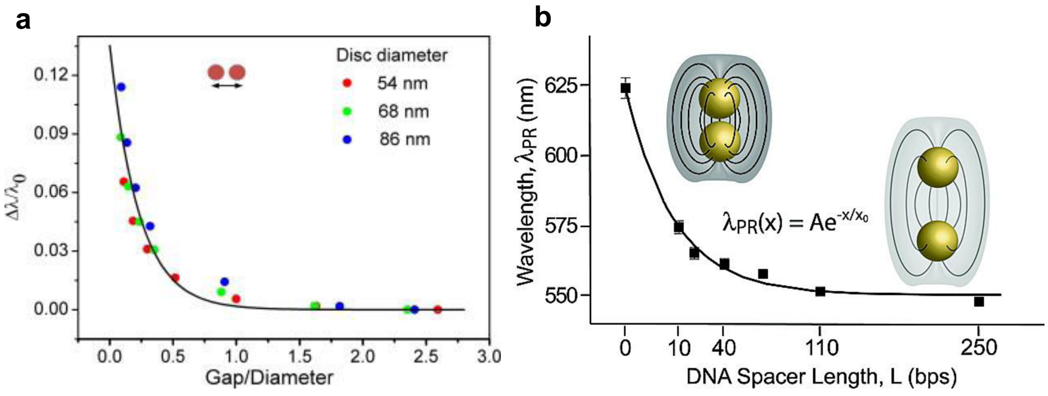

Figure 2.3: **Relationship of the plasmon resonance wavelength of a particle pair depending on their separation.** a) Nanodisks prepared by lithography show a distance-dependent exponential decay. Figure reprinted with permission from [19]. b) The same relationship is experimentally suggested by particles pair linked by DNA of varying length. Figure reprinted with permission from [44].

I use this universal exponential decay function fitted to both experimental data sets for deriving the plasmon coupling sensitivity.

2.3 PLASMON COUPLING SENSITIVITY FOR RESONANCE WAVELENGTH SHIFTS IS LINEARIZABLE

In plasmonic biosensing, the shift of the plasmon resonance wavelength of a single nanoparticle is linearly related to the change in refractive index (see **Figure 2.4A**). The first derivative of a linear function is a constant factor, that is defined as the sensitivity *S* (see **Figure 2.4B**). [46] This makes the plasmon resonance wavelength shift in biosensing easily linkable to a refractive index change.

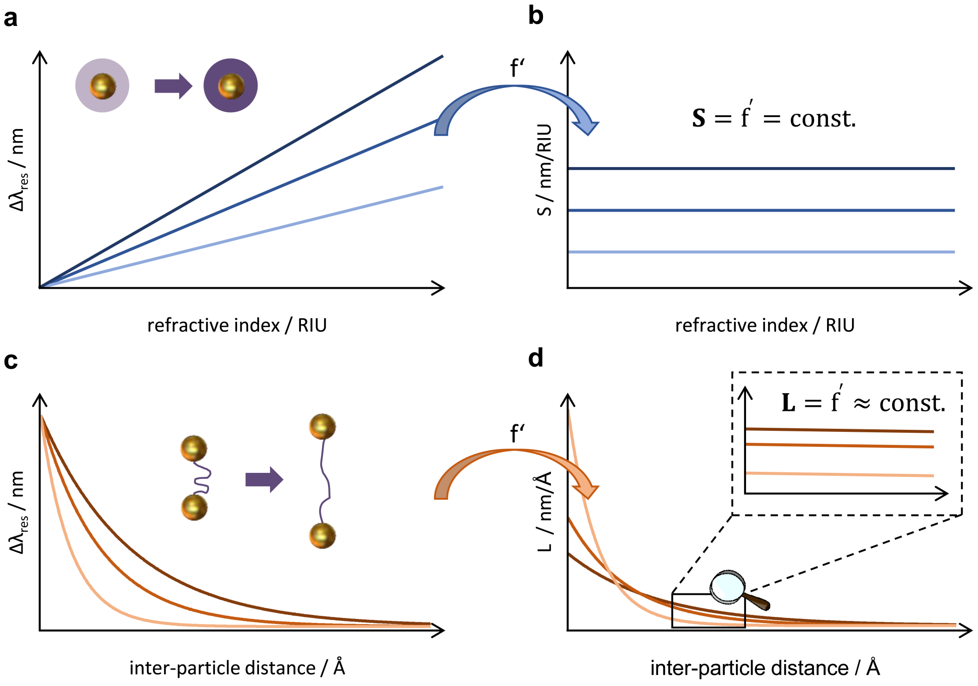

Figure 2.4: **Sensitivity in refractive index sensing and plasmon rulers.** a) When changing the refractive index of the surrounding medium around a plasmonic nanoparticle its resonance wavelength shifts linearly. b) The first derivative for refractive index sensing is a constant factor *S*. c) The inter-particle distance change shifts the resonance wavelength of a particle pair following an exponential decay d) The first derivative for the length sensitivity *L* in plasmon rulers is not a constant, but certain regions can be approximated as constant (see zoom-in).

Such intuitive formula for the sensitivity of plasmon rulers for length changes in molecules is missing. The formula deduced previously is a complicated exponential function, that relates the shift in resonance wavelength $\Delta\lambda$ to the inter-particle distance d depending on the diameter D of the nanospheres the plasmon ruler is constructed of (see **Figure 2.4C**). [19]

$$\Delta\lambda = 100.8\ nm \cdot \exp\left(-\frac{d}{0.23 \cdot D}\right) \tag{2.1}$$

I define the sensitivity of length change L of a molecule linking a particle pair as the derivative of the exponential function (same approach as used for the definition of the refractive index sensitivity).

$$\boldsymbol{L} = \frac{\partial \Delta\lambda}{\partial d} = \frac{44}{D}\ \frac{nm}{\text{Å}} \cdot \exp\left(-\frac{d}{0.23 \cdot D}\right) \tag{2.2}$$

Linearizing the exponential function is possible in some regions (see **Figure 2.4D**). Therefore one needs to know the particle diameter and the approximate medium inter-particle distance.

The sensitivity of molecular length change L depends on the particle diameter of the single nanospheres forming a plasmon ruler and the approximate mean inter-particle distance.

Most common sizes for nanospheres used in plasmon rulers are between 40 and 60 *nm* in diameter because smaller particles are harder to see in dark-field contrast and bigger particles are more likely to influence the molecule under investigation (confer to **Section 1.3**).

In **Figure 2.5** I show exemplary sensitivity values L for 40 *nm* (light colored bars) and 60 *nm* nanospheres (dark colored bars) versus approximated inter-particle distance d mean values. For $d = 112$ *nm*, both particle sizes have the same sensitivity. For inter-particles distances larger than this value, 60 *nm* diameter nanospheres show higher sensitivity and for lower values the 40 *nm* nanospheres are more sensitive.

Thus, the larger the molecule to be studied with plasmon rulers, the bigger the size of nanospheres needed to achieve sufficient sensitivity.

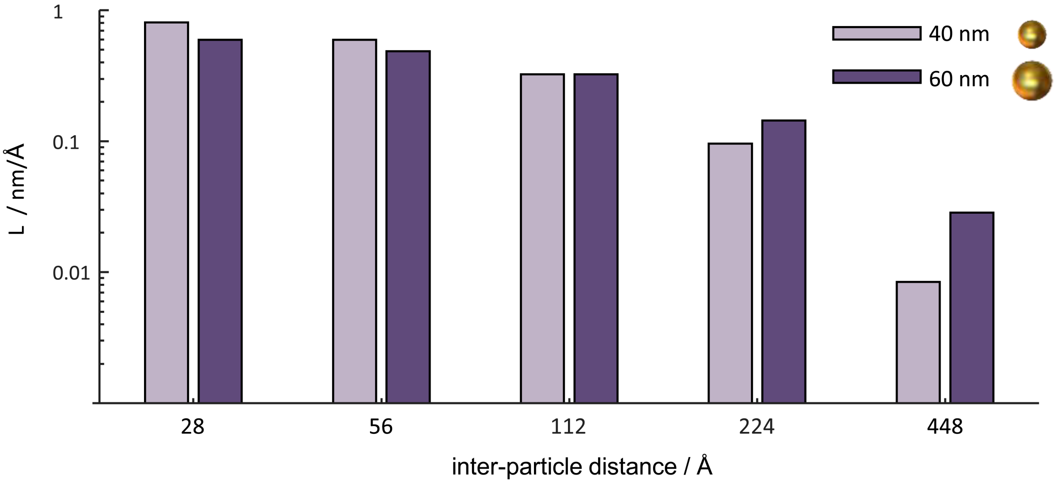

Figure 2.5: **Exemplary length sensitivity *L* for selected plasmon rulers.** Bar plot showing length sensitivity against average inter-particle distance for 40 *nm* (light-colored bars) and 60 *nm* (dark-colored bars) plasmon rulers.

2.4 PLASMON COUPLING SENSITIVITY IS ALSO APPLICABLE IN INTENSITY MEASUREMENTS

In order to transfer the sensitivity of distance valid for resonance wavelength shifts to intensity shifts, simulations with the BEM[†] (boundary element method) were conducted. [47] Spectra for two nanospheres with varying interparticle distances from 5 to 30 *nm* in 1 *nm* steps were simulated. 52 *nm* was used as diameter of the gold spheres in these calculations taking into account the tabulated optical constants for gold. [48] The spheres were supported on a glass substrate ($n = 1.5$) and surrounded by homogeneous medium with a refractive index $n = 1.34$. The simulated spectra are shown in **Figure 2.6A**. An increase of absolute scattering intensity is observed for decreasing inter-particle distance. Thus, not only wavelength shifts can be calibrated to distance changes, but also either the absolute intensity change or the intensity at a specific wavelength are suitable. If one looks at a single wavelength, one should choose one at the lower energy side of the spectrum because this side of the spectrum is stronger affected by inter-particle distance changes (see

---

[†] Simulations using BEM were carried out by Weixiang Ye.

Figure 2.6A).

The universal scaling law for plasmon coupling has only described for resonance wavelength shifts. [19] The intensity changes with decreasing interparticle distance are not predicted because the overall scattering intensity increases with decreasing interparticle separation. **Figure 2.6B** shows the spectra normalized to the spectrum with an expected average interparticle distance $d = 17\ nm$ (approximately the mean equilibrium length of PEG3000 + Streptavidin, confer to **Section 5**). [49, 50]

I only observe tiny changes in the normalized scattering intensity $I_{1,norm}$ at the transverse resonance wavelength of the dimer ($\lambda_1 = 560\ nm$). Hence, I can use this intensity value as an internal reference to a second wavelength $\lambda_2 = 632\ nm$, at which I observe a clear increase of the normalized intensity $I_{2,norm}$ with decreasing interparticle distance. I define the ratio ρ of the normalized intensity λ_2 to the normalized intensity at λ_1 as a measure for the interparticle distance.

The simulated ratio ρ as a function of interparticle distance d looks like an exponential trend ($\rho\,(d) = I_{2,norm}\,(d)\ /\ I_{1,norm}$) as shown in **Figure 2.6C**. This exponential trend is similar to the trend observed for the resonance wavelength but with a constant offset. The calculated values in **Figure 2.6C** are best described by the following equation:

$$\rho\,(d) \approx 0.84 + 4.53 \cdot exp\,(-0.2D) \tag{2.3}$$

In principle, this equation is applicable for converting the measured ρ values to interparticle distances d. However, I should consider the relatively small distance changes expected around the equilibrium position $< d >$ and the uncertainty concerning the exact nanoparticle diameter and the linker length due to their respective size distributions. With these considerations, I conclude that a linear conversion factor L helps to convert ρ values quickly to interparticle distances with negligible error.

$$L = \frac{d\rho}{dx}\ |_{<d>} = 0.906 \cdot exp\,(-0.2\cdot < d >) \approx -0.03/nm \tag{2.4}$$

In **Figure 2.6D**, the linear approximation is depicted as red line and the exact prediction as blue line. Both functions do not differ much within the range of expected interparticle distances. Thus, the sensitivity of length change for plasmon rulers L can be used for plasmon rulers with both read-out types, resonance wavelength shifts and also intensity shifts.

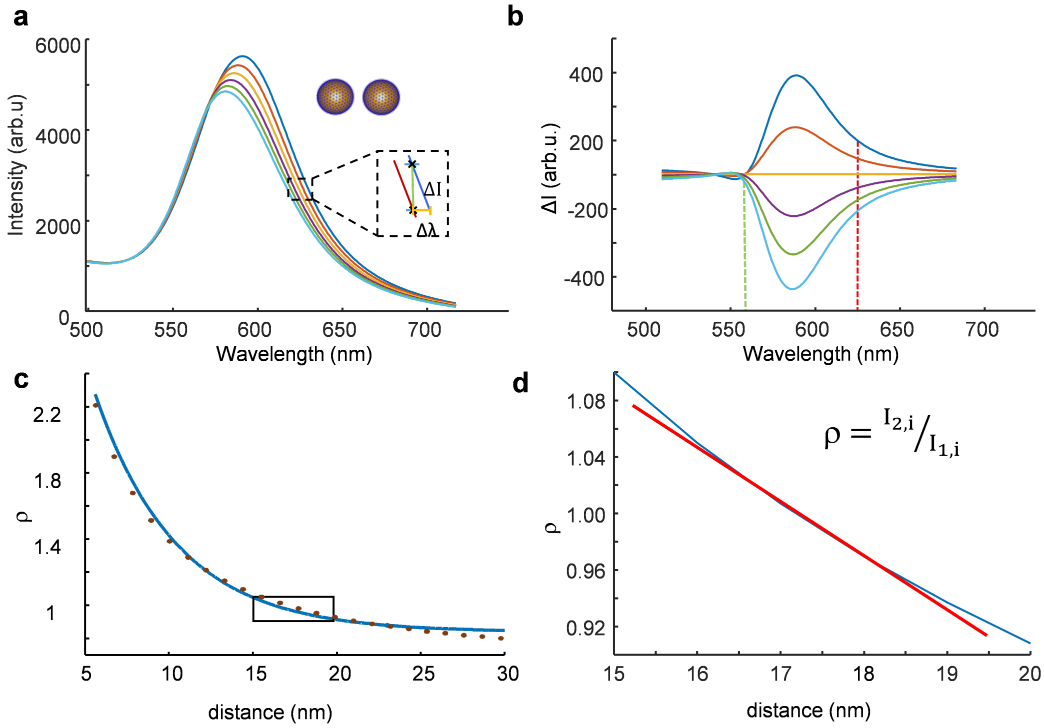

Figure 2.6: **BEM Simulations.** a.) AuNP dimer spectra calculated by BEM with increasing the interparticle distance. b.) Spectra shown in 'a' normalized to the spectrum of the equilibrium particle separation $< d >= 17\ nm$. The green dotted line ($\lambda_1 = 560\ nm$) corresponds to the transverse plasmon mode. It does not react (much) on distance changes and is used as internal reference. The red dotted line ($\lambda_2 = 632\ nm$) corresponds to the longitudinal plasmon mode and changes strongly with particle separation. c.) The ratio ρ of the normalized intensities at the two wavelengths shown in panel b is used as a measure for the interparticle distance d. Its values are shown as dots. The data points are well described by the function $\rho = 0.84 + 4.53 \cdot exp\,(-0.2d)$ (blue line). The area marked by a black box marks the region of values relevant in the experiment. d.) A zoom into the relevant region shows that the trend of $\rho\,(d)$ is well approximated by a linear relation with a slope $L = d\rho/dx \approx -0.03/nm$ (red line) around the equilibrium particle separation $< d >$. Figure included in the manuscript accepted as [51].

3 PLASMON RULER ASSEMBLY IS A KEY CHALLENGE FOR PLASMON RULERS OF PROTEINS

The preparation of plasmon rulers relies on the assembly of two plasmonic nanospheres linked by a single molecule tether. The sandwich-like assembly of this nanostructure faces challenges concerning the functionalization of each nanoparticle, tether molecule stability and the reactivity of the substrate among others. Each nanoparticle from the nanoparticle pair has to be functionalized independently to ensure its specific reactivity with the single molecule tether. Only one of the nanoparticles from the pair should bind to the substrate to ensure mobility of the second nanoparticle. The assembly of the plasmon rulers by using a single DNA molecule has been investigated in the last years (confer to **Section 1.2** for more details). [4, 6, 7, 21, 28]

However, one of the most interesting biomolecules, proteins, have not yet been studied with plasmon rulers. Elucidating protein dynamics is a crucial step in understanding protein function relevant in all living organisms. [52] With the plasmon ruler's, in principle, unlimited lifetime, it would be possible to study proteins for observation times long enough to detect rarely populated conformations.

In this chapter, I will address the challenges faced in plasmon ruler assembly involving proteins. In order to find a suitable assembly route, I will explore two types of assembly routes: assembly in solution and assembly on a surface. I will show that the assembly in solution is advantageous compared to the assembly in solution. Therefore, I will present experiments addressing the assembly in solution with different purification schemes, such as gel electrophoresis, density gradient centrifugation and pull-down assays, in **Section 3.3.1**. All of these purification schemes are inferior to the assembly in surface presented in **Section 3.3.2**. Here, I will show that the assembly on a surface forms less byproducts, needs less amount of sample compared to the assembly in solution. Further, the prepared dimers are directly ready to measure. Therefore, after exploring both assembly methods, in solution and on a surface, I will choose to assemble the plasmon rulers on a surface for plasmon ruler applications.

This assembly route on surface leads to fluctuating protein plasmon rulers using polyethylene glycol (PEG) as protein-repellent coating for the nanospheres and the substrate. The single molecule linkage is ensured by mixing functional PEG with non-functional PEG similar to previous studies. The protein was attached covalently using maleimide-cysteine chemistry.

My results obtained with the model protein Hsp90 might be adapted to other proteins broadening the applicability of plasmon rulers. Mastering plasmon ruler assembly is the key step in order to establish plasmon rulers as a complementary single-molecule technique in biophysical studies. This would allow for testing the influence of different binding partners to the dynamic behavior of proteins. Another possibility would be investigating the effect of drugs on dynamics is interesting for pharmaceutical research.

In our group, Janak Prasad has shown a 30 *min* long investigation of protein conformational changes with plasmon rulers in his PhD thesis. [53] However, in the dimer assembly only about 3 % of the monomers formed dimers and protein fluctuations could only be observed on very few of the assembled dimers. Although this study showed the successful assembly of plasmon rulers with proteins and also single protein fluctuations, the lack of reproducibility and statistics complicated the extraction of statistically meaningful kinetic constants. In order to overcome this, the goal of this work was to develop an assembly technique with higher efficiency. Given the task, higher efficiency, I need to consider the following challenges within the assembly process:

1. Proteins must be functioning after the assembly process of the plasmon ruler for protein studies. Thus, this process is constrained to be not harmful for proteins.

2. As plasmon rulers should be used as a single-molecule method, the occurrence of multiply linked plasmon rulers has to be avoided. This is not trivial, because the two nanospheres might contain multiple linking points.

3. A challenge for establishing plasmon rulers as a routine method in biophysics is to make the assembly fast and efficient. Also the assembly

process should be fast to prevent harming the protein which might not tolerate the assembly conditions.

4. For the read-out in dark-field microscopy, immobilization of the plasmon ruler is required with only one of the spheres forming the plasmon ruler and the other sphere should be mobile in solution.

I will now address the mentioned main four challenges or constraints for using plasmon rulers for protein studies in individual subsections.

3.1 PLASMON RULER ASSEMBLY SHOULD NOT HARM PROTEINS

In order to assemble plasmon rulers, each of the individual nanoparticles needs to be functionalized to couple selectively to each other. Therefore, their original ligand shell (stemming from wet-chemical synthesis) must be replaced. Usually, this is carried out by a linker, that has two different functional groups on both of its ends. One of the ends of the linker is supposed to bind to the nanoparticle surface. For the most common plasmonic nanoparticles, gold nanoparticles, mainly thiol-groups are used. Sulfur forms a covalent bond to gold, [54] stronger than the affinities of other functional groups, such as amine or carboxyl groups, and can replace these other ligands. The second end of the linker contains the functional group, that the nanoparticle needs to carry out its task. This functionality on the exterior of the nanoparticle can be used to couple it to another nanoparticle that has also been functionalized accordingly.

In order to stay correctly folded, proteins only tolerate specific conditions. The plasmon ruler process must be constrained in this respect. Oxidizing or reducing agents need to be avoided, because they could reduce or oxidize amino acids forming the protein sequence. The reagents used in the assembly process have to be water-soluble, because proteins only tolerate aqueous solutions (or maybe a maximum 5 % of an organic solvent, for example DMSO). The plasmon ruler is ideally assembled at room temperature, because elevated temperatures (above 40 °C) denature proteins. Strong bases or acids change the three-dimensional structure of proteins, thus, the pH should be buffered between

$5-8$ depending on the specific protein. Often a specific salt concentration, for example of $150\,mM$ is required to keep the protein intact. The specific values for the protein chosen in this work, Hsp90, are listed in **Table 3.1**

Table 3.1: **Conditions tolerated by Hsp90.**

pH	$6.7 - 7.4$
ϑ / °C	< 37
$c(KCl)$ / mM	$20 - 150$
$c(MgCl_2)$ / mM	10
$\varphi(DMSO)$ / $vol\%$	< 5

3.1.1 LINKING STRATEGIES MUST BE SUITABLE FOR PROTEINS

Other single-molecule techniques, like optical tweezers and atomic force microscopy (AFM), require linking of two probes similar to the plasmon ruler. The main linking schemes used in the mentioned techniques are DNA linkers and biological tags. [10, 55]

Considering the conditions constraining the plasmon ruler assembly with proteins, applicable linking strategies include: [56]

1. Dithiolated linkers
2. Click chemistry
3. DNA linkers utilizing base pairing
4. Biological tags (like streptavidin-biotin, digoxigenin-anti-digoxigenin or His-tag)
5. Bio-conjugate covalent crosslinkers

I will now describe the above listed linking strategies in individual subsections.

3.1.1.1 DITHIOLATED LINKERS

Considering the strong affinity of thiols to gold, the most direct way to bridge two gold nanoparticles is employing a dithiolated linker. This linker could contain the molecule under investigation, for example a protein with two thiol functionalities. In theory, one thiolated end would bind to the first gold nanoparticle and the other thiolated end to the second nanoparticle. This strategy has been used for forming dimer linked by alkanedithiols. [57] Alkanedithiols are suitable for this purpose because they are so rigid that it is unlikely for them to bend in such a way that both thiols bind to the same particle.

I tried to expand this approach using dithiolated polyethylene glycol in order to form plasmon rulers investigating polymer dynamics. Since PEG is a less rigid molecule than alkanes, it is indeed possible for one single PEG to bind with both thiol groups to a single nanoparticle. If PEG molecules are in high excess compared to the nanoparticle concentration, all particles will be fully covered by PEG, before cross-reactions between individual particles take place.

I use a batch assembly approach (confer to **Section 3.3.1**) because both nanoparticles forming the dimers need to be present at the same time. In order to find an optimal ratio of dithiolated PEG to nanoparticles, I added varying concentrations of PEG to a fixed amount of nanoparticle solution. In **Figure 3.1A** I show extinction spectra of dithiopegylated nanospheres with increasing concentration. The resonance wavelength first increases to higher wavelength with increasing PEG concentration indicating dimer formation and then, with even higher ligand concentration, decreases again suggesting dispersion of single nanoparticles fully covered with a ligand shell.

The same conclusions can be drawn from **Figure 3.1B** showing a gel picture from gel electrophoresis. Only the particles pegylated with the highest concentrations (lane 5 and lane 6) move considerably meaning they are smaller than the aggregated particles in the other lanes.

Although dimer formation was achieved here, the purification of those according to **Section 3.3.1** is difficult because the higher-order aggregates are not mobile in gel electrophoresis due to their lack of charge. A possibility to introduce charges would be to use a ligand mixture, but a fine adjustment of the adsorption kinetics of the different ligands would be necessary in order to keep assembling dimers. Maybe the purification with HPLC would be successful.

Our model protein, Hsp90, contains two mutated cysteines, meaning two thiol functions. The direct coupling of the thiols to the gold surface would not be recommended because proteins can denature upon direct contact with a gold surface. [26] Hence, it would be necessary to modify the thiols on the protein with a linker which contains another thiol on the outer end. This scheme is difficult to realize due to unwanted side-reactions with the competing thiols. For other proteins without thiols, the dithiolated linker would be a worthwhile strategy.

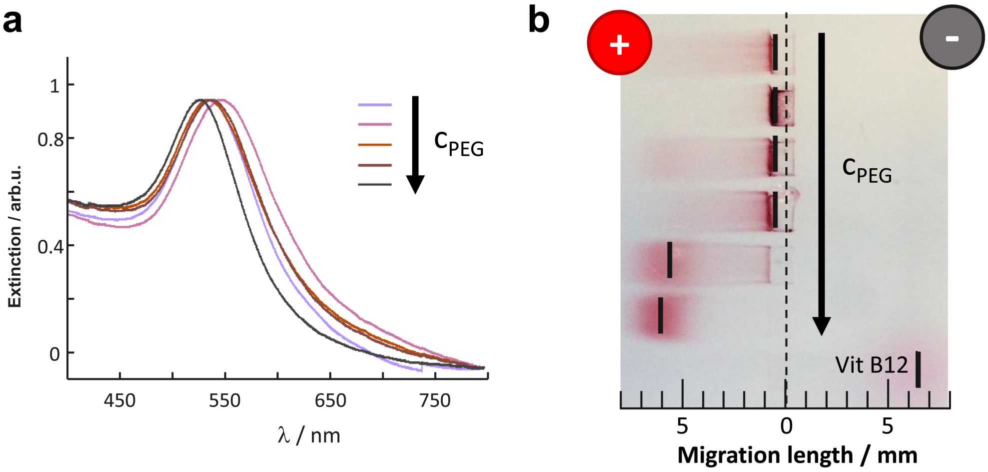

Figure 3.1: **Dimer formation with dithiolated PEG.** a) Extinction spectra of nanospheres pegylated with dithiollinker show first an increase of the resonance wavelength and then a decrease with increasing linker concentration. b) Picture of a gel after gel electrophoresis showing Vitamin B12 in lane 7 as reference. Lanes 1 - 6 show nanospheres coated with increasing ligand concentration. Only the nanospheres coated with high ligand concentrations (lane 5+6) move in the electric field suggesting they are smaller (monomers) than the particles coated with lower ligand concentrations (dimers and other aggregates).

3.1.1.2 CLICK CHEMISTRY

The term click chemistry refers mainly to the copper catalyzed coupling of an azide to an alkyne. It has been successfully used to couple small nanospheres (with a diameter of 14 *nm*, see **Figure 3.2**). [58] To use click chemistry in plasmon rulers, I needed to expand this functionalization to bigger nanospheres (40 *nm*) to improve plasmon ruler sensitivity for our relatively large protein (8 *nm*). [19] To date the commercially available ligands (thiol-linker-azide and thiol-linker-alkyne) are too short to stabilize bigger nanospheres. Thus, it would be needed to synthesize the linkers tailored to the application.

Using click chemistry with proteins requires an attachment point in the protein sequence. Usually, this is achieved by mutation with an unnatural amino acid. Our collaborators tried this mutation on our model protein, Hsp90, but the protein did not tolerate this mutation. Therefore, the approach of click chemistry was not further pursued. For other proteins the mutation might be working and then also the click chemistry assembly strategy for plasmon rulers should be possible.

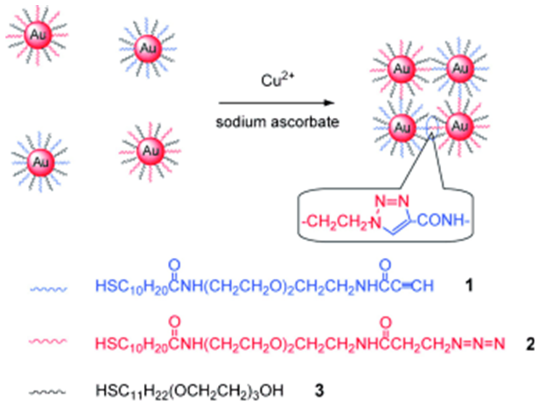

Figure 3.2: **Click chemistry with gold nanoparticles.** Nanoparticles functionalized with an alkyne (blue) can be coupled to nanoparticles functionalized with an azide (red) with sodium ascorbate and Cu^{2+}. Figure reprinted with permission from [58].

3.1.1.3 DNA HYBRIDIZATION

Two strands of DNA can bind to another (hybridization), if their base pair sequence is complementary, and only fall apart again when exposed to elevated temperatures (their strand specific melting temperature). Double-stranded DNA forms so effectively because of π-π stacking of the DNA base pair and hydrogen bond formation. Using DNA-hybridization leads to the coupling of two particles functionalized with matching DNA-strands. Therefore, in some of the plasmon ruler studies for DNA investigation, one set of nanospheres was functionalized with a single DNA strand and the other one with its complementary DNA strand and, thus, the plasmon ruler was formed due to hybridization. [6, 7, 21]

For studying DNA with plasmon rulers, the functionalization of two sets of nanospheres with matching strands, is the most direct way. [7] Since the functionalization strategy is routine and optical tweezers experiment also use DNA as a linker to study protein dynamics, [2] it should, in principle, be possible to use DNA as linkers for studying protein dynamics. For optical tweezers experiments with Hsp90, the protein has been modified with two DNA strands and each of the two beads was modified with a large DNA linker (370 nm) with a small overhang (12 nm). This overhang was complementary to the DNA coupled to Hsp90, so that the DNA strands hybridize and form the optical tweezers.

I tried to use this strategy for plasmon rulers by replacing the large DNA linkers (370 nm) of optical tweezers with a small DNA linker (3 nm). In **Figure 3.3**, I show a sketch drawn to scale for the plasmon ruler with DNA linkers.

In case of our model protein, Hsp90, I observed binding of DNA-functionalized Hsp90 as well as unmodified Hsp90 to DNA-coated nanoparticles (confer to **Figure 3.4**). This unspecific binding is likely caused by the ATP binding domain in Hsp90. [59] For optical tweezers, the linker interaction with the protein is not a problem because the tweezers are tightened before the start of the measurement. This is not possible with plasmon rulers as a force-free method. For other proteins, DNA-linkers might be a good approach.

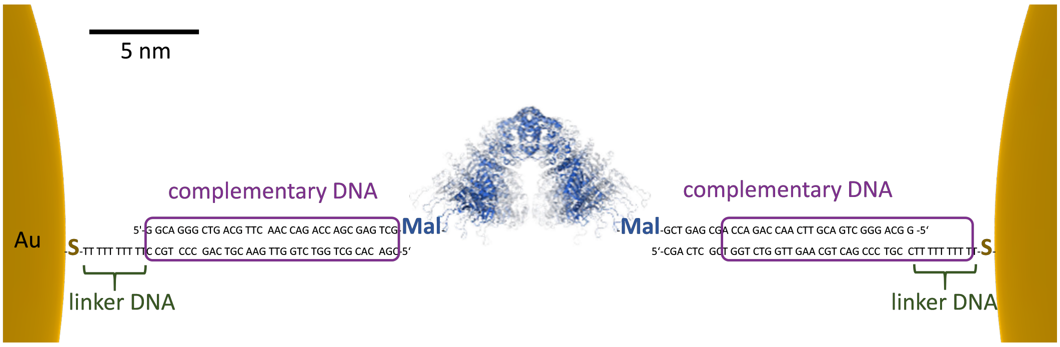

Figure 3.3: **Strategy for Hsp90 plasmon ruler with DNA linkers.** Gold nanospheres are functionalized with thiolated DNA strands consisting of a short linker (3 *nm*) and a complementary part (12 *nm*). The thiols in the cysteines of Hsp90 were reacted with maleimide-DNA that is complementary to the DNA on the gold nanoparticles. Overhang of the DNA sequence is similar to optical tweezers experiments. [2] Hsp90 sketch adapted with permission from [60].

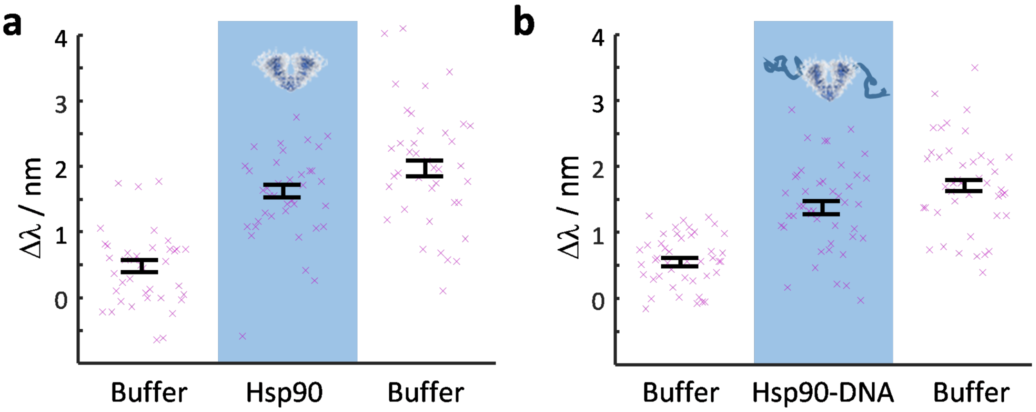

Figure 3.4: **Unspecific binding of Hsp90 to DNA.** Shift in resonance wavelength for individual nanoparticles (each cross) functionalized with DNA incubated with Hsp90 (a) or Hsp90 coupled to complementary DNA (b). Hsp90 can not be washed off indicating unspecific binding.

3.1.1.4 BIOLOGICAL TAGS

Biological tags are employed widely used in biochemistry to specifically connect non-covalently. For connecting probes in other single-molecule techniques, like optical tweezers and atomic force microscopy (AFM), biological tags are the most common attachment schemes. [10, 55] Common biological tags include streptavidin-biotin, digoxigenin-anti-digoxigenin (dig-anti-dig) or NTA-His-tag. [61] An overview of binding affinities and size of the systems is given in **Table 3.2**. For plasmon ruler assembly, a higher binding affinity (lower K_D), a higher association rate (k_{on}), a lower dissociation rate (k_{off}, with $k_{off} = K_D \cdot k_{on}$) and a smaller linker molecule is preferred because the linkage should be stable and as small as possible.

The NTA-His-tag interaction has the smallest size increase in linkage $< 1\,nm$, but the binding affinity ($10^{-6}\,M$) is not as high as in the streptavidin-biotin system ($10^{-14}\,M$). The association rate for streptavidin-biotin ($5 \cdot 10^{8}\,M^{-1}s^{-1}$) is higher compared to NTA-His-tag ($10^{2}\,s^{-1}$) leading to a faster assembly for streptavidin-biotin plasmon rulers. The dissociation rate for streptavidin-biotin ($5 \cdot 10^{-6}\,s^{-1}$) is lower compared to NTA-His-tag ($10^{-4}\,s^{-1}$) leading to a lower frequency of bond disruption for streptavidin-biotin which is preferred in plasmon rulers. The average duration until one bond disrupts is $50\,s$ for dig-anti-dig, $3\,h$ for NTA-His-tag and $56\,h$ ($2.3\,d$) for strep-biotin. The strep-biotin bond has the highest lifetime and is therefore the most suitable of the three biological tag systems. Since the size increase of $5\,nm$ from streptavidin can be accepted in plasmon ruler assembly, the streptavidin-biotin-system is the most suitable from the biological tags.

For plasmon ruler assembly, one set of particles is coated with streptavidin, whereas the other set is functionalized with a bi-functional linker, containing a thiol and a biotin on either end. The thiol attaches to the gold surface and the biotin is the function on the exterior of the particle. Next the biotin particle binds to the streptavidin particle. The most practicable way is that the molecule under investigation serves as linker and, thus, it is necessary to tag this molecule with the two required functionalities (thiol and biotin).

Table 3.2: **Binding affinities and size of different biological tags.**

	strep-biotin [62, 63]	dig-anti-dig [64]	NTA-His-tag [65]
diameter / nm	5	15	< 1
K_D / M	10^{-14}	10^{-9}	10^{-6}
k_{on} / $M^{-1}s^{-1}$	$5 \cdot 10^8$	$2 \cdot 10^7$	10^2
k_{off} / s^{-1}	$5 \cdot 10^{-6}$	$2 \cdot 10^{-2}$	10^{-4}
k_{off} / min^{-1}	$3 \cdot 10^{-4}$	1.2	0.01
k_{off} / h^{-1}	0.02	72	0.36

Many of such bi-functional linkers are commercially available, for example DNA can be modified with thiol and a biotin on either end. In some studies investigating DNA, one nanosphere was functionalized with streptavidin and the other nanosphere with a biotinylated DNA-strand. [4, 28] This strategy was also employed to study DNA-hairpins in this work (confer to **Section 4)**. In this work, I expand the concept to polymer studies, employing as linker a bi-functional polyethylene glycol (see **Section 5**). This concept can, in principle, be extended to proteins where the protein would be biotinylated and then bind to streptavidin coated nanoparticles (see **Figure 3.5**). However, I decided not to follow this strategy for Hsp90.

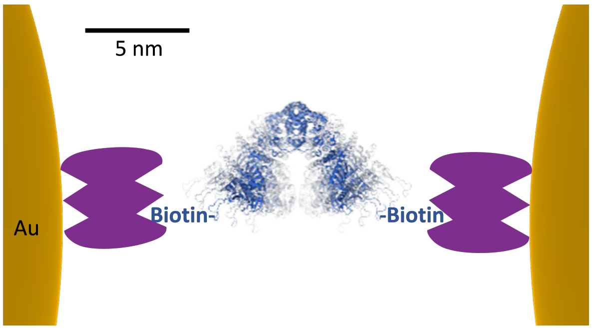

Figure 3.5: **Strategy for Hsp90 plasmon ruler with streptavidin-biotin.** Gold nanospheres are functionalized with thiolated streptavidin (5 *nm*, in violet). The thiols in the cysteines of Hsp90 could be reacted with maleimide-biotin. The biotinylated Hsp90 will then bind to the binding pockets of streptavidin and form the dimer. Hsp90 sketch adapted with permission from [60].

3.1.1.5 COVALENT CROSSLINKERS

A bio-conjugate covalent crosslinker needs to be tailored to the protein under investigation. My model protein, Hsp90, has been genetically mutated with two cysteine residues. Previous FRET experiments have used these two cysteines with their thiol functionality for coupling to two fluorescent dyes. [3] These dyes contained a maleimide that reacts with a thiol in an addition reaction. Having the two thiols as unique attachment points for the two nanospheres, it was necessary to obtain nanospheres containing a maleimide function on their outer end. A direct coating of maleimide linkers to nanospheres is not possible, because the maleimide would react with thiols used to coat the nanosphere. Thus, a two step process is difficult to avoid. An example of a bio-conjugate covalent crosslinkers reacting to thiols is SMCC (Succinimidyl- 4- (N- maleimido methyl) cyclohexane-1- carboxylate), that is able to bridge an amine with a thiol-functionality. Since SMCC is not soluble in water, it needs to be dissolved in an organic solvent like DMSO beforehand and then added to the aqueous protein solution. For proteins not tolerating organic solvents, there is a water-soluble analogue of SMCC, namely sulfo-SMCC. However, sulfo-SMCC is negatively charged leading to possible unwanted interactions with proteins. My predecessor used sulfo-SMCC. [53] I chose to assemble plasmon rulers with SMCC because our protein tolerates a small content of DMSO ($< 5\,vol\%$) and I hypothesize that the uncharged linker reduces unspecific binding of the protein.

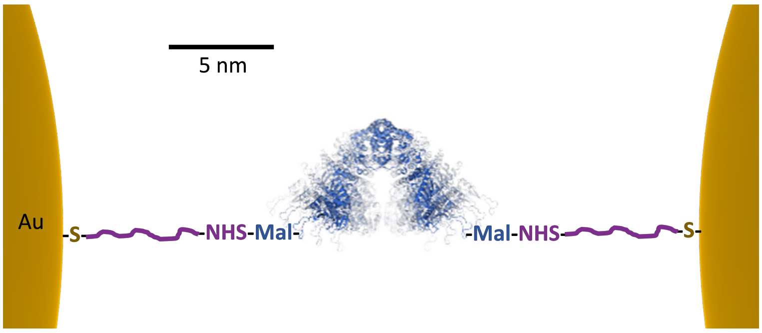

Figure 3.6: **Strategy for Hsp90 plasmon ruler with PEG.** Gold nanospheres are functionalized with thiolated polyethylene glycol containing an amine on the outer end ($5\,nm$, in violet). The thiols in the cysteines of Hsp90 are reacted with SMCC (consisting of a maleimide and a NHS-group). The NHS-group will then bind to the amine of the PEG and form the dimer. Hsp90 sketch adapted with permission from [60].

Specifically, I coated the nanospheres obtaining an amine at their outer end to which the carboxylic acid active ester in SMCC can bind (confer to **Section 6** and **Figure 3.6**). SMCC holds another functionality, a maleimide group, thus, the nanoparticle's most exterior function is then a maleimide readily available for one thiol in Hsp90. Repeating this process with the second Hsp90 thiol, a plasmon ruler linked with a protein is formed for investigation. In general, this strategy requires the genetic mutation of two cysteines at opposite ends of the protein. I recommend using proteins, like Hsp90, that do not contain natural cysteines omitting side-reactions.

In summary, the linking strategy for proteins is highly dependent on the available mutants and their specific attachment points and their unspecific binding to the linker material, for example DNA. Mutants include cysteines requiring maleimide-thiol-chemistry or unnatural amino acid that are specifically designed for the use with click chemistry.

3.1.2 SALT CONCENTRATION CAN AFFECT PLASMON RULER FUNCTIONALITY

After having chosen the linking strategy, covalent crosslinkers, I also need to ensure the functionality of the plasmon rulers. In order to avoid irreversible particle aggregation, the two main forces, electrostatic repulsion and van-der-Waals attraction, need to be balanced creating a potential barrier (confer to DLVO-theory presented in **Section 1.3**). In a higher salt environment, the forces resulting from electrostatic repulsion are decreased without changing the attractive van-der-Waals forces resulting in a decrease of the potential barrier. If the potential barrier is too low (about $1\,k_B T$), particle aggregation occurs leading to a non-fluctuating plasmon ruler. In order to investigate the effect of salt concentration, I show the percentage of fluctuating dimers varying the salt concentration of the measurement solution in **Figure 3.7**.

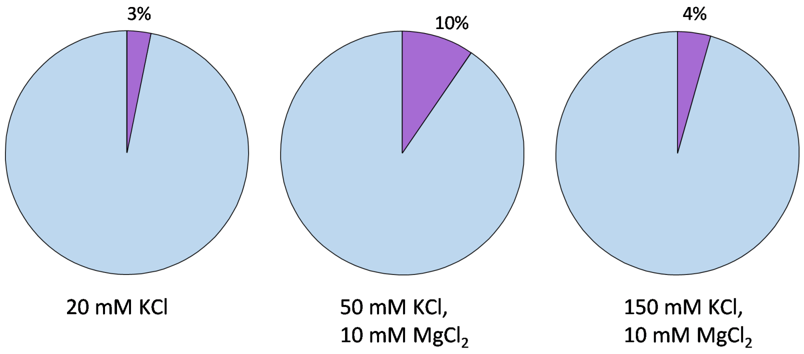

Figure 3.7: **Optimization of salt concentration during dimer measurement.** Percent of fluctuating dimers in violet. In lower salt concentration unspecific attachment of particles is hindered, but protein denaturalization is more likely compared to higher salt concentrations. I observe the optimum salt concentration to be $50\,mM\ KCl$.

Concerning the plasmon ruler technique, I expect a higher amount of fluctuating dimers with lower salt concentration. In higher salt environments, the attractive forces between the two particles of the dimer are increased leading to potential particle aggregation resulting in an non-fluctuating plasmon ruler. For proteins, I expect the opposite trend: The protein should be more stable in higher salt concentrations. Hence, the amount of non-functional protein should decrease with higher salt concentrations and the percentage of fluctuating plasmon rulers increase. From the three different salt environments tested with Hsp90, I indeed observe the medium salt concentration 50 $mM\,KCl$ as the condition with the highest percentage of fluctuating plasmon ruler (see **Figure 3.7**).

Although I observed a maximum percentage of fluctuating plasmon rulers of about 10 % in the experiment shown in **Figure 3.7**, this result was not reproducible. Repeating the experiment with 50 $mM\ KCl$ resulted in a variation of fluctuating dimers from 1 % to 18 % with a mean value of 8 % (for seven experiments, see **Figure 3.8**).

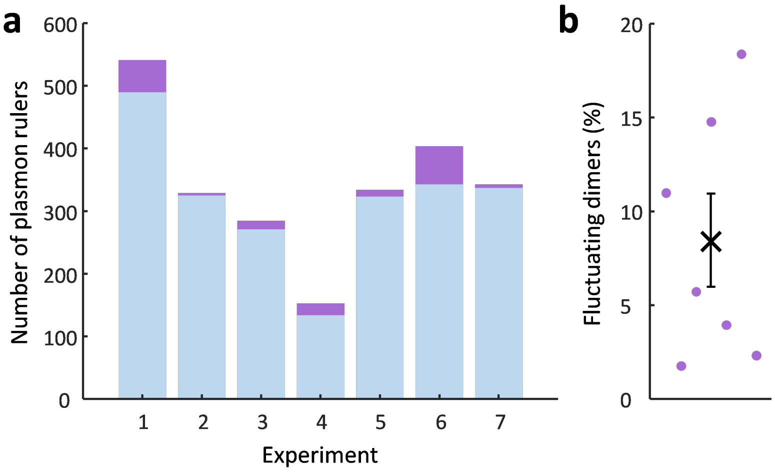

Figure 3.8: **Experimental variation of the amount of dimers and fluctuating dimers.** a) Bar diagram of the number of formed plasmon rulers for seven different experiments with the number of fluctuating dimers shown in violet. b) Fraction of the fluctuating dimers compared to the formed dimers in percent for each experiment with mean and standard error of the mean.

3.2 MULTIPLE LINKAGES MUST BE AVOIDED

Plasmon rulers are supposed to investigate single molecules. However, plasmonic nanoparticles can potentially have more than one attachment site, since multiple ligands fit on the nanoparticle surface leading to unwanted multiply linked dimers. Preparing monovalent particles would overcome this problem enabling a controlled assembly in the next step.

Similar to nanoparticles, multiple molecules fit on the probe of other single-molecule techniques (confer to **Section 1.1.2**), like optical tweezers and atomic force microscopy (AFM). [10] One possibility for single molecule AFM is the unspecific adsorption of proteins to the surface of the flow chamber and the AFM-tip picks up the single molecule while pushing against the surface. Moving the tip away from the surface and monitoring the unfolding curve reveals, if indeed only a single molecule has been linked between surface and tip. To increase the chance of single molecule linkage, the proteins are immobilized in a low concentration on the surface. However, only 1 % of the trials lead to a single molecule linkage. [66] The application of force to link molecules is not adaptable to plasmon ruler assembly, a force-free technique. Another possibility is the modification with specific recognition elements, like streptavidin-biotin (confer to **Section 3.1.1.4**), where a fraction of the binding sites is blocked before attachment to ensure single linkage. [55] This concept could, in principle, be adapted to plasmon rulers: first the nanoparticles should be coated with streptavidin, then a fraction of streptavidin could be blocked with free biotin and the unblocked streptavidin could bind to a biotinylated second nanosphere. Another approach is the formation of mixed self-assembled monolayer (SAM) on a gold tip containing shorter nonreactive ligands and reactive ligands. The distribution of the reactive ligand is adjusted to yield predominantly single molecules, here 26 % of the measured curves. [67] A mixed SAM can be assembled on a nanoparticle surface as well as on the AFM-tip and I will use this approach throughout my thesis. Optical tweezers mainly rely on the biological tags (confer to **Section 3.1.1.4**) as attachment points on the two beads forming the tweezers and single molecule linkage is ensured by a low concentration of the linker. [10] First one bead is modified with the linker and then the second bead is approaching the first bead with the help of an optical trap while a solution is flown through the chamber to stretch the linker. [68] In plasmon ruler assembly, the second nanoparticle can not be moved towards the first one, but we have to rely on diffusion. When flow would be used to stretch the linker, the nanoparticles would be washed out of the flow chamber because they are not trapped.

From the concepts presented above, I chose the mixed SAM formation on the nanoparticles forming plasmon rulers. The complete ligand shell around a nanoparticle can consist of multiple ligands of different kinds, e.g. a mixture of an 'active' ligand that is reactive and can be coupled to another particle and a 'passive' ligand that is nonreactive and will not take part in any coupling reaction. Only if there is just one single active ligand within the whole nanoparticle ligand shell, the nanoparticle is considered monovalent. This can be achieved by functionalizing the nanoparticle with excess of passive ligand compared to the active ligand

The proportions of the functionalization mixture might differ from the actually assembled functionalization layer on the nanoparticle surface, because of different reaction rates of the individual ligands. For example, alkane thiols will assemble more quickly than PEG thiols and also remove PEG thiols. [69, 70] To minimize different reaction rates, I use similar ligands with just a variation of the outward functional group, for example methoxy PEG as passive ligand and biotin PEG as active ligand.

In this chapter, I will first elaborate on the theoretical distribution of valencies in a nanoparticle dispersion depending on the functionalization ratio according to Poisson statistics. In the next subsection, I will present techniques to separate monovalent nanoparticles from a dispersion containing nanoparticles with multiple valencies, like gel electrophoresis, HPLC and pull-down assay. Within this work, I will not employ these techniques because I was not able to expand them to nanoparticle sizes needed for plasmon rulers.

3.2.1 Poisson Statistics Describes Valency Distribution

In the functionalization procedure, one can add a certain ratio of linkers to particles, I call the functionalization ratio λ. However, the nanoparticles in the resulting dispersion will only contain on average the number of linkers given by the functionalization ratio λ while each individual nanoparticle in the dispersion contains a discrete number of linkers k. The probability to find a discrete number of linkers per particle k depending on the functionalization ratio λ follows a Poisson distribution P. The probability $P(k)$ to obtain the number of linkers k for varying functionalization ratio λ is shown in **Figure 3.9**.

$$P = \frac{\lambda^k e^{-\lambda}}{k!} \tag{3.1}$$

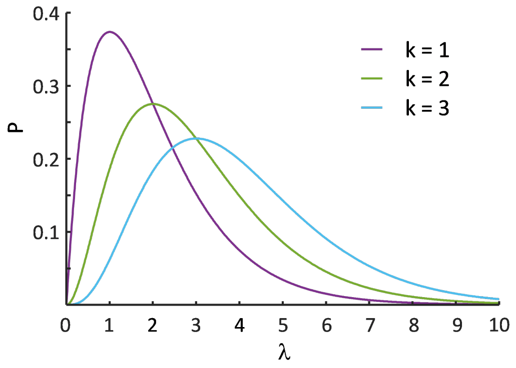

Figure 3.9: **Poisson distribution of valencies in nanoparticles.** The Poisson distribution P against the functionalization ratio λ for the chosen number of linkers per particle $k = 1, 2$ and 3 is shown in violet, green and blue, respectively.

For functionalization of nanospheres, a number of linkers per particle of $k = 1$ (monovalent) is the optimum to ensure single linkage. However, in a functionalization procedure aiming for $k = 1$, the highest probability to actually obtain monovalent nanoparticles is only about 37 % (for $\lambda = 1$). Increasing the functionalization ratio to $\lambda = 1.5$, the probability to obtain exactly a single linker on the nanoparticle ($k = 1$) decreases to 33 % (from 37 % for $\lambda = 1$). Thus, it it impossible to purely obtain monovalent nanoparticles, but a mixture of valencies will be created.

In this work, the functionalization ratio λ was mostly greater than one ($\lambda > 1$) because I perform the assembly on a surface where half of the nanosphere is blocked (confer to **Section 3.3.2**). For plasmon rulers connected by polyethylene glycol (PEG) the functionalization ratio was adjust to $\lambda = 6$ (confer to **Section 5**). Although $P(k = 1)$ for $\lambda = 6$ is only 0.01 %, I do not observe multiple linker formation (see Appendix **Figure 8.5**). I hypothesize that the multiple functional groups the nanoparticle contains are spatially distributed resulting in a lack of multiple linker formation (see sketch in Appendix **Figure 8.3**). Lowering the functionalization ratio by a factor of 10 to $\lambda = 0.6$ with a probability $P(k = 1)$ of 33 %, only plasmon rulers with single linkage are formed (as expected) whereas the dimerization efficiency decreased only by a factor of 3 (see Appendix **Figure 8.6**). This lower dimerization efficiency with lower λ is caused by a higher probability of non-functional particles ($P(k = 0)$ for $\lambda = 0.6$ is 55 %) that are unable to assemble into dimers. 55 % of the immobilized monomers should not assemble and stay monomers where 33 % should form dimers, 10 % trimers and 2 % tetramers. However, I observe only 6 % of dimers and no trimers and tetramers. I hypothesize steric reasons (e.g. contribution from the substrate surface) and/or lack of incubation time (see **Section 3.3.2**) for this lower than expected dimerization efficiency.

For the plasmon rulers linked by Hsp90, I use a functionalization ratio of $\lambda = 3.6$ (where $P(k = 1)$ is 10 %). Since the PEG plasmon rulers can serve as a model system because of similar functionalization procedure, I hypothesize that this functionalization ratio ($\lambda = 3.6$) would ensure single linkage. However, only few of the Hsp90 plasmon rulers fluctuate (up to 10 %) although all PEG plasmon rulers with similar λ fluctuate according to a single molecule. From the difference, I conclude the lack of fluctuating Hsp90 plasmon rulers must be caused by other reasons despite multiple linker formation, for example protein denaturation.

3.2.2 SOME TECHNIQUES CAN ISOLATE MONOVALENT NANOPARTICLES

Functionalizing nanoparticles to directly obtain purely monovalent nanoparticles is impossible (confer to **Section 3.2.1**). A distribution of different valencies will be created in a functionalization procedure.

However, monovalent nanoparticles can be isolated from polyvalent or nonvalent ones by the following appropriate techniques:

- Gel electrophoresis
- HPLC (high performance liquid chromatography)
- Pull-down-assays

Gel electrophoresis is a technique able to separate nanoparticles depending on their size and charge. [71] The charge separation is based on the movement of charged particles in the gel according to the applied electric field, whereas a sieving mechanism is responsible for the size sorting moving the smaller particles faster than the larger ones. Thus, the combination of size and charge affects the electrophoretic mobility of particles.

In consideration of the rising distance sensitivity with increasing nanosphere diameter (confer to **Section 2**), for many applications at least 40 *nm* particles are desirable. However, the larger a nanoparticle gets, the lower the chance that a single functionality outweighs the electrophoretic mobility. Presently, this technique is limited to particle sizes in the range of 20 *nm*. [72]

The separation of a mix of monovalent and polyvalant nanospheres with the help of gel electrophoresis is shown in **Figure 3.10A**. [72] The visual impression suggests that the bands in the gel corresponding to the different nanoparticle fractions are well separated, but an analysis with extinction spectroscopy of the gel piece reveals that the bands overlap, especially the mono-functional and the dual-functional fraction. This separation is insufficient and will likely require an additional purification step after dimer formation. Thus, in this work, this technique was not considered.

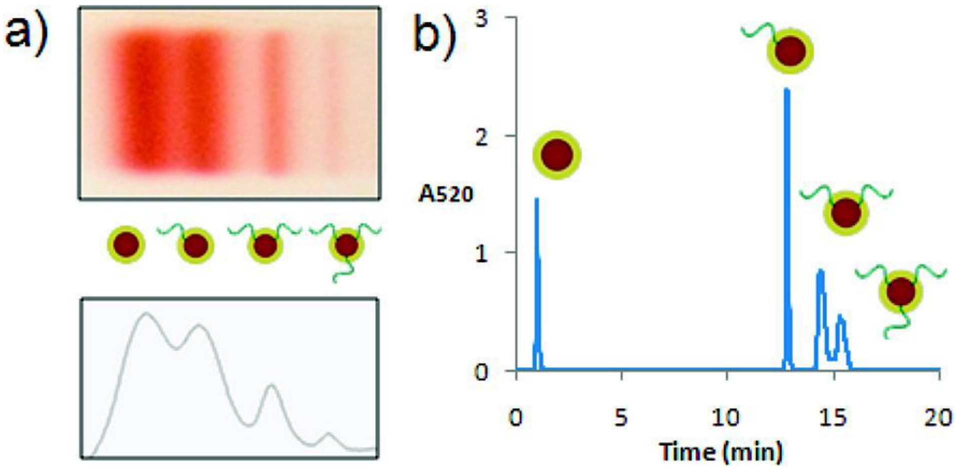

Figure 3.10: **Isolation of monovalent nanospheres by gel electrophoresis and HPLC.** a) Separation of a mix of mono- and polyvalent nanospheres by gel electrophoresis. Although the different bands are visually well-separated (top), the extinction spectroscopy (bottom) reveals overlapping bands. b) With the help of HPLC the same mix of nanoparticles can be separated with a clear sharp peak (starting and finishing at the baseline) for the monovalent fraction of nanoparticles. Figure reprinted with permission from [72].

In high performance liquid chromatography (HPLC) the nanoparticles are first bound to a column and then eluted fraction-wise. The fraction of nanoparticles with the least affinity to the column will be eluted first, next the fraction with the second highest affinity will be washed off the column and so on. In **Figure 3.10B**, I show an exemplary chromatogram illustrating the elution order dependent on time of the different fractions of nanoparticles. First a fraction containing nanoparticles functionalized solely with inactive ligands is eluted, next appears the fraction with monofunctional, then bifunctional and last trifunctional nanoparticles. In contrast to gel electrophoresis, the mono-functional nanoparticle fraction is well-separated from the other fractions, shown by the baseline resolution of the peak. [72] Isolation of monovalent nanospheres by HPLC has been shown for nanoparticles of diameter up to 30 *nm* for longer DNA-strands (70 base pairs). [28]

A method without the need for advanced instrumentation is the so-called pull-down assay. Here, large polymeric micro-spheres are coated with a layer that has a high affinity to the active ligand of the nanoparticle. The crucial step is to lower the ratio of active to inactive ligand so far, that only monofunctional and non-functional nanoparticles are created. The monovalent nanoparticles will then attach to the microsphere, whereas the non-functional will stay in solution (see **Figure 3.11A**). Since the microspheres are much heavier than the nanoparticles, the microspheres will sediment over time and can be easily (without the need of centrifugation) separated from the nanoparticle dispersion.

This particular assay has been performed in the literature for nanoparticles of a diameter of 5 *nm* (see **Figure 3.11B**). [73] The fraction of pulled-down nanoparticles is plotted against the ratio of active to inactive ligand. If 100 % of the nanoparticles are pulled down, these nanoparticles are not monovalent, but a population of many valencies was created with this functionalization ratio. The most suitable functionalization ratio is chosen, when about 20 % of the nanoparticles are pulled down because then the population of bi-functional nanoparticles is negligible.

I tried to expand this idea to bigger nanoparticles suitable for dark-field microscopy. In **Figure 3.11C**, I show photographs of particles functionalized with an increasing ratio of active to inactive ligands with diameters of 10 *nm*, 15 *nm* and 40 *nm*, respectively. Despite of the successful functionalization and pull-down assay for the 10 *nm* and the 15 *nm* particles, I observed irreversible aggregation of the 40 *nm* nanoparticles.

All in all, pull-down assays are fast and easy to conduct without the need for advanced instrumentation, but in order to continue with these kind of assays, an optimization of the functionalization would be necessary. While the pull-down assay presented here relies on sedimentation, another very common pull-down assay is based on magnetic separation. Here, one would bind the monovalent nanoparticles to a magnetic bead, that can be separated by the dispersion of non-functional nanoparticles by applying an external magnetic field (e.g. with a magnetic stir bar). [25]

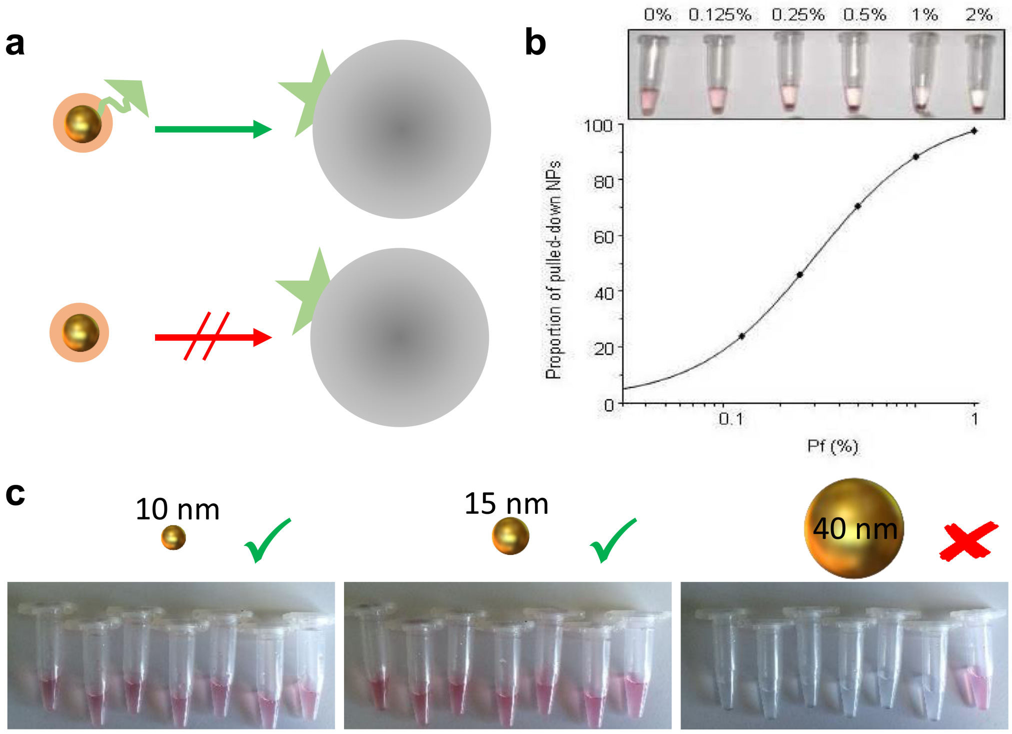

Figure 3.11: **Isolation of monovalent nanospheres by pull-down assay.** a) Functionalized gold nanoparticles are incubated with polymeric microbeads with an anchor point for the nanoparticles functionalization. Only the nanoparticles containing the functionality (top) will be pulled down by the microsphere and the inactive nanoparticles (bottom) will stay in solution b) Gold nanoparticles (diameter of 5 nm) functionalized with increasing ratios of active to inactive ligands resulting in a higher percentage of functionalized nanoparticles pulled-down by the beads. Figure reprinted with permission from [73]. c) Repetition of the experiment presented in b) for nanoparticle with diameters of 10 nm (left), 15 nm (middle) and 40 nm (right). 40 nm particles are not stable for smaller ratios.

Techniques for isolating monovalent nanoparticles from a mixture of particles include gel electrophoresis, HPLC and pull-down assays. Here, I tested gel electrophoresis and pull-down assays. I was not able to extend these strategies to bigger nanoparticles that are necessary for the plasmon ruler sensitivity. From literature, it is suggested that also HPLC is not suitable to separate bigger nanoparticles. [72, 28] In this work, I therefore omit the purification before assembly. Thus, the nanoparticles contain to some extend multiple functionalities, but I rely on the statistic distribution meaning the individual active ligands are so far away from each other to not form multiple linkages. I use on surface assembly (see **Section 3.3.2**) where one could say that only nanoparticles containing a functional group will react and be pulled down to the surface.

3.3 ASSEMBLY PROCESS IS TIME-CRITICAL

The assembly process by itself should be fast and efficient. The efficiency is limited by Poisson statistics to a maximum of 27 % (see **Figure 3.9**, $\lambda = 2, k = 2, P = 27\,\%$). Regarding the time, there are two main assembly strategies. Either the two types of nanoparticles are assembled in solution and the byproducts are separated from the dimers before the immobilization in the flow cell for the investigation with dark-field microscopy. Or the first particle type is immobilized directly in the flow cell and the second type is then coupled to the first type in a second step.

3.3.1 BATCH ASSEMBLY

The assembly in solution has the big advantage of producing plasmon rulers in an amount lasting for several experiments. One can prepare a stock of dimers at once, store them and later immobilize an aliquot of the dimers in a flow cell. To create a stock of dimers, one has to get rid of the reaction by-products.

For the separation of dimers assembled in solution from higher-order aggregates or monomers, the following two main separation techniques are common:

- Gel electrophoresis
- Density gradient centrifugation

The fundamental principle of gel electrophoresis is explained in the previous section. After coupling the two nanoparticle batches in stoichiometric ratio, the dispersion containing monomers, dimers, trimers and higher-order aggregates is separated with gel electrophoresis according to their size. This means, the gel band moving the fastest consists of the monomers and the second band is the dimer band that is then cut out of the gel. By applying an electric field to this piece of gel the dimers will be dragged out of the gel and a dispersion containing only dimers is created.

This separation method is widely used for plasmon rulers linked by DNA. [6, 28] I also used the method for assembling DNA based plasmon ruler containing a hairpin, that could be expanded by a complementary strand (see **Figure 3.12** and **Section 4**). The photograph of the gel after the electrophoresis was performed shows, that indeed it is possible to separate the dimer band from unreacted lef-over monomers (confer to lane 4 of the gel). Further the expanded dimers (first band in lane 3) increase in size compared to the unexpanded dimers resulting in a decreased electrophoretic mobility.

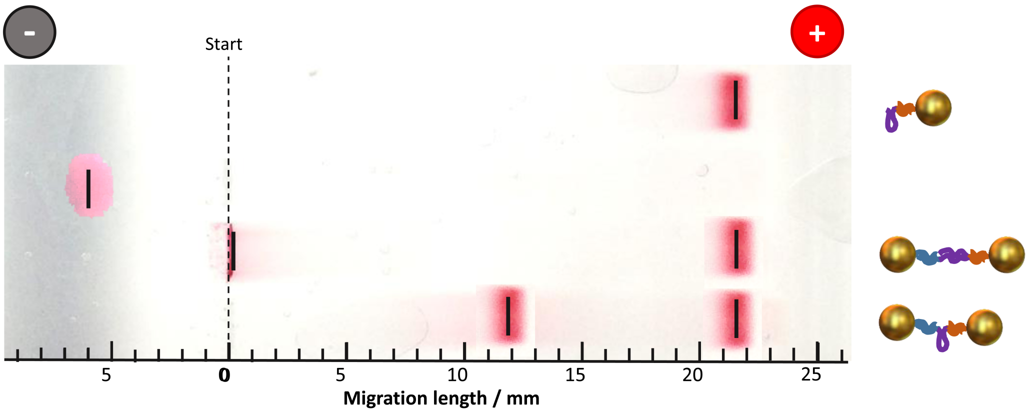

Figure 3.12: **Isolation of dimers with gel electrophoresis.** The first lane shows the electrophoretic mobility of monomers. The second lane is a reference lane filled with vitamin B12. In the third lane two bands are visible: One fraction was not moved within the gel under the conditions used and corresponds to expanded dimers, the other band shows the same electrophoretic mobility as the monomers (lane 1) and consists of unreacted monomers that did not form dimers. The fourth lane also shows two fractions: again one monomer band and an additional band corresponding to unexpanded dimers.

Gel electrophoresis purification works best for DNA plasmon rulers. For polymers and proteins it it not suitable. In case of polymer plasmon rulers, the functionalization layer is less charged and, thus, the mobility in the gel is decreases leading to insufficient separation of the bands in the gel (see **Figure 3.1**).

Proteins are too sensitive for an extraction out of the gels and they are likely not functional anymore.

Another separation technique is density gradient centrifugation that separates particles according to their size and density. The density gradient in a centrifugation tube is created by stacking sugar solutions of different concentrations above one another (highest density at the bottom). After the analyte is loaded on top of the gradient, centrifugal force is applied. Bigger and denser particles sediment faster than smaller ones.

The method has been applied to silica-encapsulated particles (confer to **Figure 3.13A**). [74] The highest fraction corresponds to the monomers, the middle fraction to dimers and the last fraction to trimers. The desired fraction can be easily removed with a pipet.

I transferred the same procedure to our bridged dimers and could observe the same trend (see **Figure 3.13B**). For proteins, this method might not be suitable, if they do not tolerate high concentrations of sugars.

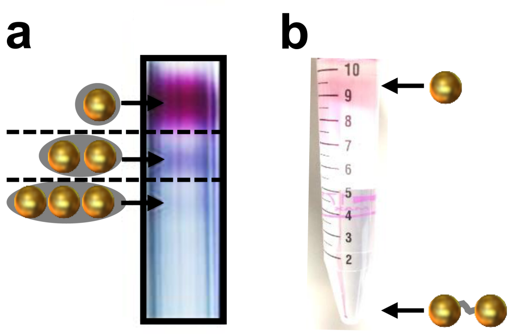

Figure 3.13: **Isolation of dimers with density gradient centrifugation.** a) Density gradient centrifugation performed on silica-encapsulated nanospheres resulting in different fractions: monomers, dimers and trimers (from top to bottom). Figure adapted with permission from [74]. b) Density gradient centrifugation performed on a mix of monomers and dimers linked by a single molecule.

In summary, both methods for isolating dimers out of a mixture of monomers, dimers and trimers, namely, agarose gel electrophoresis and density gradient centrifugation are feasible. Even if monovalent nanoparticles are isolated by pre-dimerization and coupled to dimers, it is still possible that the yield of reaction is not complete and, thus, a post-dimerization purification might be necessary on top. [28]

3.3.2 ON SURFACE ASSEMBLY

Despite the preparation and purification of many dimers in parallel (batch approach), it is also possible to assemble a pair of nanospheres sequentially. First one kind of nanoparticles is immobilized on the glass surface of a flow-cell directly in the microscope (see **Figure 3.14**). Next the second kind of nanoparticles is coupled to the immobilized nanoparticles sandwiching a molecule examinable by the plasmon ruler. The advantage lies in the direct usability of the plasmon ruler for the measurement. Thus, avoiding long storage time for sensitive proteins.

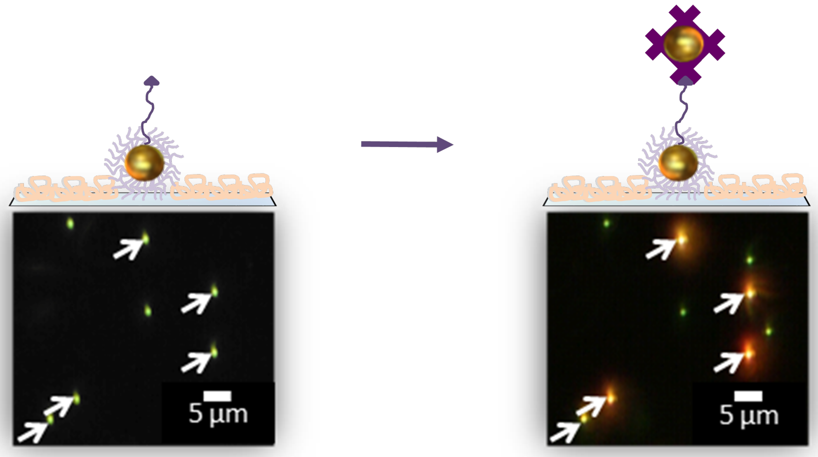

Figure 3.14: **Sequential assembly of dimers on a glass surface.** Sketch of a single nanoparticle immobilized on a microscope glass surface (top left) that is coupled to a second nanoparticle linked by a single molecule forming a dimer (top right). The corresponding real color dark-field images are shown on the bottom (single nanoparticles appear green and dimers yellow).

This assembly technique has been applied to prepare the first demonstrated plasmon ruler. [4] The use of a flow cell enables an effective rinsing of the nanoparticles. Further the observation of the dimer formation in the dark-field microscope is directly possible because one observes a dramatic change in intensity and color from green for single particles to yellow for dimers (confer to **Figure 3.14**). The amount of nanoparticles needed is less than for batch assembly because isolating dimers according to the methods presented in **Section 3.3.1** leads to loss of material. Specifically, the protein concentration is a limiting factor. I chose the on surface assembly in this work because it offers more control of the assembly and the plasmon rulers are directly ready to measure.

Considering efficient coupling, I need to take into account the very low surface concentration of the first immobilized particle set and the diffusion limited reaction rate. The first particle set is distributed on the glass surface to yield approximately one particle on an area of $10^8\,nm^2$. The concentration c of the second set of nanoparticles is typically around $10^{10}\,particles/mL$ or $0.01\,nM$ and the diffusion coefficient D of the second set of nanoparticles is $6 \cdot 10^{-12}\,m^2 s^{-1}$. I assume that a diffusing nanoparticle has to approach an immobilized nanoparticle within a distance of $0.1\,nm$ for a reaction (reaction shell). Using the theory developed for FCS (fluorescence correlation spectroscopy), [75] I can calculate the average time τ_D a nanoparticle spends in a reaction shell with a radius r_0 according to:

$$\tau_D = \frac{r_0^2}{4 \cdot D} \tag{3.2}$$

The radius of the reaction shell r_0 should be in the range of a typical covalent bond because, I assume, if two reactive groups encounter within the distance of a covalent bond, they should react. The radius for a typical covalent bond is $0.1\,nm$ and therefore, I estimate the radius of the reaction shell r_0 to be accordingly $0.1\,nm$. [76] The movement of the reaction shell does not play a role in the calculation of the reaction time. The real size of the reaction shell might be bigger, but I do not account for other factors that might slow down the reaction, such as orientation of the reaction partners or reaction barrier. The lateral movement of $1\,nm/h$ of thiols on a gold surface is negligible, [77] whereas the diffusion coefficient for a PEG molecule fixed with one end to a surface ($10^{-12}\,m^2 s^{-1}$) is smaller compared to the diffusion coefficient of the nanosphere ($6 \cdot 10^{-12}\,m^2 s^{-1}$). For the estimation of the diffusion time t, I only consider the biggest diffusion coefficient, the diffusion coefficient of the sphere, because the biggest diffusion coefficient is dominating in the diffusion process.

In this case, the time spent in the reaction shell is $4 \cdot 10^{-10}\,s$ or $400\,ps$. Since the time it takes for forming a covalent bond is in the femtosecond range, [78] the time the diffusing nanosphere spends in the reaction shell is sufficient for the performance of the reaction. I define the reaction time t as the time it takes on average for a reacting particle to diffuse to the reaction shell with radius r_0 that is dependent on particle concentration c and given by:

$$t = \frac{\tau_D}{\frac{4}{3}\pi \cdot c \cdot r_0^3} = \frac{1}{\frac{16}{3}\pi \cdot c \cdot D \cdot r_0} \tag{3.3}$$

Here, a single individual nanoparticle encounters the reaction shell every $28\,min$ which is the reaction time t it takes for dimer assembly on average. In summary, the reaction time t depends on the temperature T, the concentration of the second nanoparticles c and the size of the nanoparticles with radius r. The temperature is not regarded as an important parameter because an increase in temperature from room temperature (20 °C) to 40 °C only accelerates the reaction speed by a factor of 2. Within the temperature range acceptable for proteins ($0 - 40\,°C$), the reaction time t varies between $15\,min$ for the highest temperature and $43\,min$ for the lowest temperature. The particle concentration c is the most accessible parameter as shown in **Figure 3.15A**. Increasing the particle concentration c from $0.01\,nM$ to $0.1\,nM$ quickens the reaction by a factor of 10. The size of the nanospheres has also a small contribution to the reaction time t (linear relationship as shown in **Figure 3.15A**). The bigger the radius of the nanospheres r, the slower their diffusion coefficient D and, thus, also the reaction time t. The particle size is more or less fixed in the range of $20 - 30\,nm$ in radius r due to signal to noise and plasmon ruler sensitivity with not significant effect on the reaction time t ($\pm 8\,min$).

All in all, the particle concentration c is the parameter that could, in principle, be easily adjusted. When assembling particles on a surface, the particles have two possible reaction partners, the immobilized particles on the surface and the free glass surface. The reaction to the immobilized particles is desired and the binding to the free glass surface must be avoided because a completely covered glass surface would make measurements impossible. For single particle darkfield spectroscopy, the individual nanoparticles need to be distributed approximately 10 μm. However, the reaction rate to the glass surface depends also on concentration (see possibilities for glass surface passivation in **Section 3.4**). Therefore, the particle concentration can not be increased indefinitely. Although the trends shown here, reaction time t decreases with particle concentration c and increases with particle radius r hold true, the determination of the exact reaction time t is only estimated and might not be reliable because the reaction time t is highly dependent on the unknown radius of the reaction shell r_0.

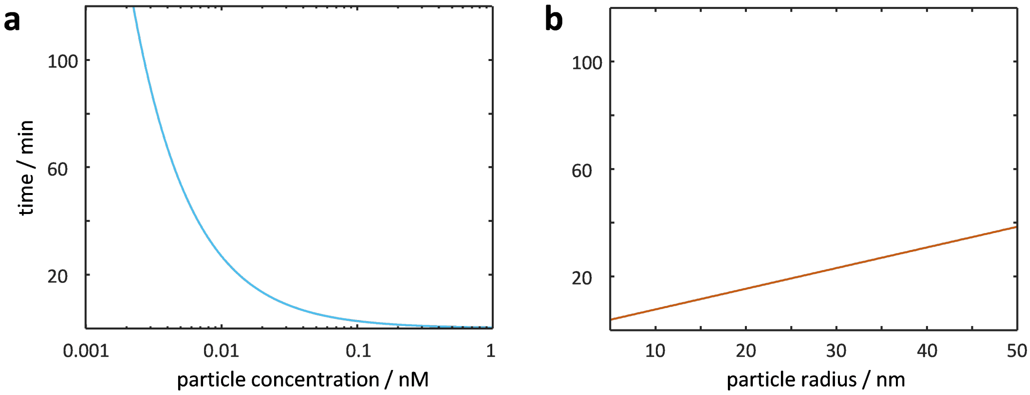

Figure 3.15: **Binding time for diffusing nanospheres.** a) The diffusing time for a sphere of radius $r = 35\,nm$ to a reaction shell with a radius of $r_0 = 0.1\,nm$ at room temperature (20 °C) for varying nanoparticle concentration. b) The diffusing time for spheres with a concentration of $c = 0.01\,nM$ to a reaction shell with a radius of $r_0 = 0.1\,nm$ at room temperature (20 °C) for varying nanoparticle radius.

Table 3.3 summarizes the advantages and disadvantages of the two approaches, batch assembly and surface assembly. In this work, I decided to assemble the dimers on a surface because there are more advantages for this strategy.

Table 3.3: **Advantages and disadvantages of assembly strategies.**

	Advantages	Disadvantages
in batch	higher yield	purification more difficult
on surface	less by-products less amount of sample needed dimers are directly ready to use	glass passivation more difficult

3.4 GLASS SURFACE PASSIVATION IS CRITICAL

For assembling dimers that can function as plasmon rulers, both methods of dimer preparation need to ensure that the second set of nanoparticles should attach only to the first set of nanoparticles, but not to the glass surface. Hence, the nanoparticle stays mobile in solution and its position is controlled by the molecule bridging the plasmon ruler. If both particles stick to the glass surface, the attractive forces between glass and particles are bigger than the molecular motion rendering the plasmon ruler nonfunctional. However, the assembly on a surface requires a higher quality of the glass passivation because the particles are present in a higher concentration and for a longer amount of time.

Instead of using glass as a substrate, it would also be possible to detect plasmon rulers in reflection mode immobilized on not transparent substrates. The transmission mode gives higher light intensities per time unit increasing signal to noise ratio and enabling a higher time resolution. Hence, I use transmission mode in this work and a transparent substrate with passivation is necessary.

Another reason to avoid binding of further nanoparticles to the microscope slide while assembling dimers in a flow-cell is the possibility of crowding the whole surface, thus, causing single-particle dark-field spectroscopy unfeasible (this technique needs to resolve spectroscopically single particles or here dimers).

I call a glass surface hindering binding of nanoparticles a passivated glass. Techniques for passivation of glass surfaces either block the glass surface around the first set of particles after their immobilization or passivate the whole glass surface before any particles are introduced in the flow-cell adding anchor points to which only the first set of nanoparticles can bind (not the second set).

The unspecific blocking of glass can be achieved by surfactants and proteins. [79] Common proteins used include bovine serum albumine (BSA) and milk proteins, such as casein. I use this approach in this work for studying polymer dynamics (confer to **Section 5**) because these protein blocking agents passivate glass fast (within 5 *min* and without high need of expertise and labor effort since only a solution of protein in a buffer needs to be prepared). Although this approach is suitable for studying DNA and polymers, it is not for investigating proteins because proteins tend to bind to other proteins.

PEGylated glass slides commonly used in other single-molecule studies of proteins are also suitable for the passivation of plasmon ruler for proteins, even offering anchor groups for the specific attachment of the first set of particles (see **Figure 3.16**). [80] The glass is coated with silan-PEG creating a self-assembled monolayer of PEG chains hindering proteins to attach. The preparation requires special glass handling equipment, training and is laborious, thus, it only makes sense to use this passivation approach, if necessary for the specific plasmon ruler experiment.

I evaluate the passivation quality of the glass surface by incubating nanospheres to a glass surface in a flow-cell of the dark-field microscope. After washing off the excess of particles, I take real-color images and count the particles that have been bound. The worst quality is attributed when all particles from the solution have been captured by the glass and the best quality is when no additional particle have bound. An example of such an extraordinary quality slide is shown in **Figure 3.16**. Here no extra particles were immobilized even after 24 *h*. With this quality of slides, I was able to study protein dynamics (confer to **Section 6**).

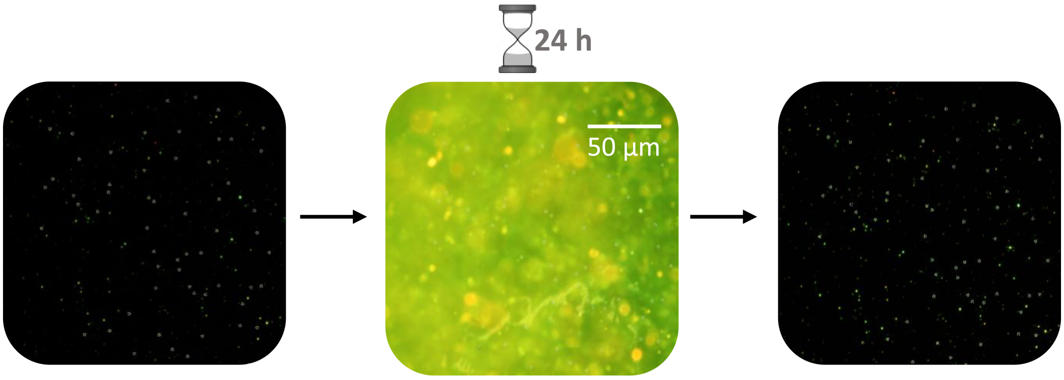

Figure 3.16: **Evaluation of passivated glass with PEG.** Real color picture of the green single nanospheres immobilized to a pegylated glass surface in a flow-cell (left). Additional nanoparticles are introduced to the flow-cell and incubated for 24 *h* (middle picture). After washing the flow-cell, it appears that no additional nanospheres have bound to the glass surface proofing the stability of the passivation for 24 *h*.

In order to compare the PEG coated glass slide to the previously used BSA passivation, I counted the number of immobilized nanoparticles. Therefore, a nanoparticle dispersion with a concentration of $0.01\,nM$ was incubated in the flow cell for $30\,min$. The flow cell consisted of plain glass as a reference or glass coated with BSA according to [53] or glass coated with PEG according to [80]. After washing of the excess of nanoparticles, the immobilized nanoparticles were counted. I define a binding coefficient as number of immobilized nanoparticles on the passivated glass divided by the number of nanoparticles immobilized on plain glass. In **Figure 3.17**, I show the binding coefficient for BSA and PEG coated glass. The mean binding coefficient for BSA is 4.6 % and for PEG 0.2 %. This improvement by a factor of 20 for PEG compared to the BSA passivation implies a decreased affinity of the nanospheres to the passivation. Hence, it is possible to increase the concentration of second nanospheres in the solution for the assembly step on the surface. This possible increase in concentration could lead to a faster assembly (see **Section 3.3.2**). In this respect, we should consider the rate of dimer formation compared to the rate of binding to glass surface. The rate of dimer formation is $\frac{1}{28\,min}$, as discussed in (**Section 3.3.2**. The rate of particle binding to passivation r_{pass} is calculated taking into account a concentration c of 10^{10} $particles/mL$ in the flow cell, a volume V above a single immobilized particle in the flow cell of 10^{-8} mL (10 μm X 10 μm X 100 μm), the above mentioned binding coefficients BC and the incubation time t of 30 min with the following formula:

$$r_{pass} = \frac{c \cdot V \cdot BC}{t} \tag{3.4}$$

The rate of binding to the glass surface is $\frac{1}{150\,min}$ for PEG passivation and $\frac{1}{7\,min}$ for BSA passivation. By the time one dimer assembles (28 min), one particle has been immobilized on a PEG passivated surface on an area where five nanoparticles of the first set of nanoparticles sit compared to 20 particles bound to BSA passivated surface. This decrease of unspecific immobilization of nanoparticles on PEG compared to BSA passivation enables a longer incubation time before the surface is blocked in such a way that measuring becomes impossible.

Further, the reproducibility of PEG passivation is also better compared to BSA: binding coefficients for BSA vary between $1.6 - 6.7\,\%$ and for PEG $0 - 0.5\%$ (see **Figure 3.17**). Hence, I employ the PEG passivation for the investigation of protein dynamics.

In my opinion, glass slide passivation is crucial for the assembly of dimers on a substrate because it hinders the attachment of nanoparticles to the substrate. Crowding of the surface with nanoparticles would render plasmon ruler spectroscopy difficult because the plasmon rulers need to be spread on the substrate above the diffraction limit. Avoiding the surface would eliminate the problem of passivation. In order to investigate the plasmon rulers, they could be hold in place by an optical trap. [81] In optical trapping of plasmon rulers, heating and photo-damage of sensitive samples need to be considered.

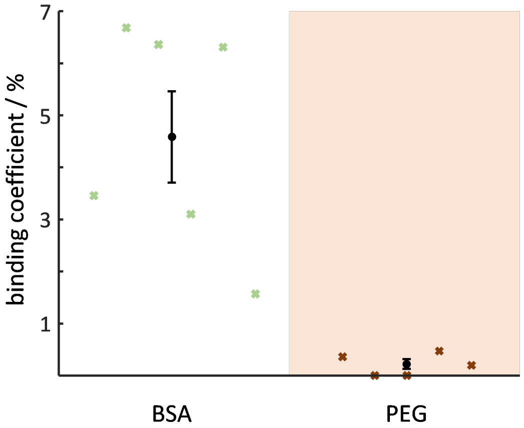

Figure 3.17: **Comparison of passivation strategies, BSA and PEG.** Binding coefficient (number of particles bound to passivated glass compared to plain glass as a reference) after incubation of 30 min to BSA coated glass and PEG coated glass. Each cross represents an individual flow cell with mean and standard error of the mean.

3.5 CONCLUSION

In this chapter, I addressed the major constraints or challenges faced in plasmon ruler assembly. The first constraint is that the assembly conditions must be protein-friendly. For the model protein of this work, Hsp90, this means $pH = 6.7 - 7.4$, $\vartheta < 37\,°C$, content of organic solvent $\varphi < 5\,vol\%$ and salt concentrations of $c\,(KCl) = 20 - 150\,mM$ and $c\,(MgCl_2 = 20\,mM)$.

My improvements were to decrease the pH from 7.4 to 6.7 and using SMCC instead of sulfo-SMCC which requires the addition of a small amount of organic solvent ($\varphi = 5\,vol\%$) to increase the coupling efficiency from 3 % to 20 %. This small amount of solvent is not harmful for the protein as shown by FRET where the fluorescent dyes are also dissolved in organic solvent. [3] The organic solvent will be rinsed off before the measurement of the protein fluctuations, so that it should not influence the dynamics. Further I decreased the salt concentration from $c\,(KCl) = 150\,mM$ to $50\,mM$ to yield decrease the attractive forces between the two nanoparticles forming the dimer.

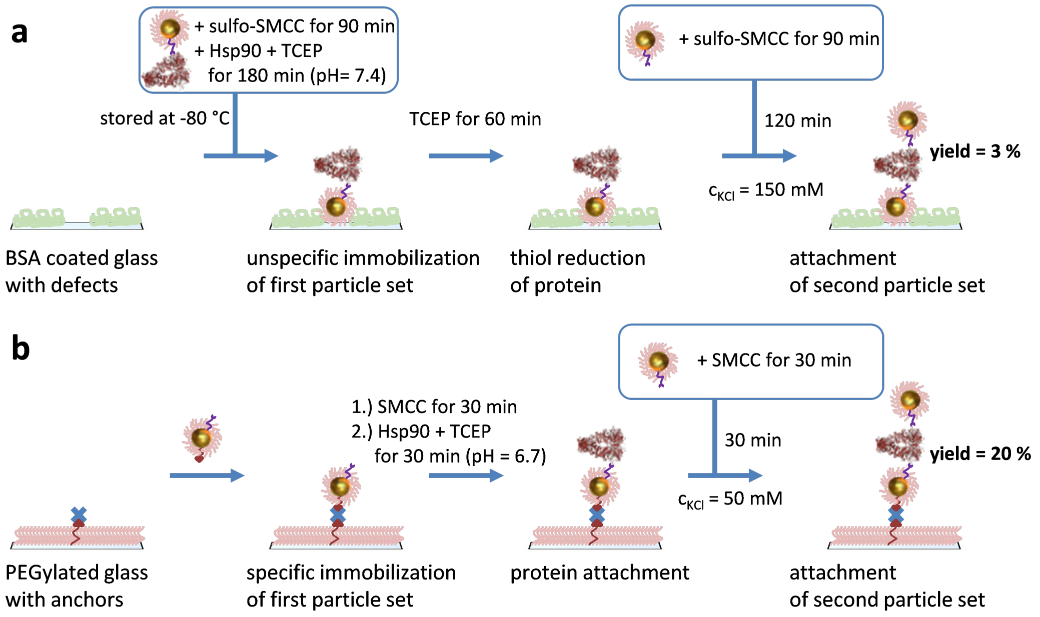

Figure 3.18: **Comparison of assembly strategies for plasmon rulers for Hsp90.** a) Assembly strategy for Hsp90 plasmon ruler previously developed. [53] Hsp90 was coupled to nanoparticles in solution before the unspecific immobilization of the particles in the defects of BSA (shown in green) coated glass. After the reduction of the thiol in Hsp90, the second nanoparticle set was attached. b) Assembly strategy developed in this work. The first particle set is immobilized specifically with the help of anchor groups (streptavidin, shown in blue). Hsp90 is coupled to the nanoparticle in the flow cell and the second particle set attached afterwards.

The second challenge named here is the assurance of single-linked dimers. The nanoparticles are functionalized with a mixture of ligands. These ligands are chemically similar except their outward functional group to yield similar reaction kinetics. I adjusted the ratio of functional ligand to $\lambda = 3.6$ because I use the on surface assembly making half of the nanoparticle not accessible (similar to previous work). [53]

In **Figure 3.19**, I show the Poisson distribution for the functionalization ratio $\lambda = 3.6$ on plasmon rulers. Only 3 % of the immobilized nanoparticles contain no protein and should therefore not form a dimer and stay a monomer. Experiments do not reach this optimal case of 3 %, but additional problems limit it to about 80 %, probably lack of reaction time and steric hindrance by the surface.

Since the proteins are randomly distributed on the nanoparticle, some proteins on the nanoparticles face to the glass camouflaging as nonreactive nanoparticles not forming dimers. Steric hindrance is also caused by the curvature of the nanospheres hindering multiple tether formation as shown by the sketch of dimers drawn to scale in **Figure 3.19**. Since multiple tether formation does not occur in PEG-dimers with a similar functionalization ratio, I hypothesize that multiple tethers are very rare in Hsp90-dimers.

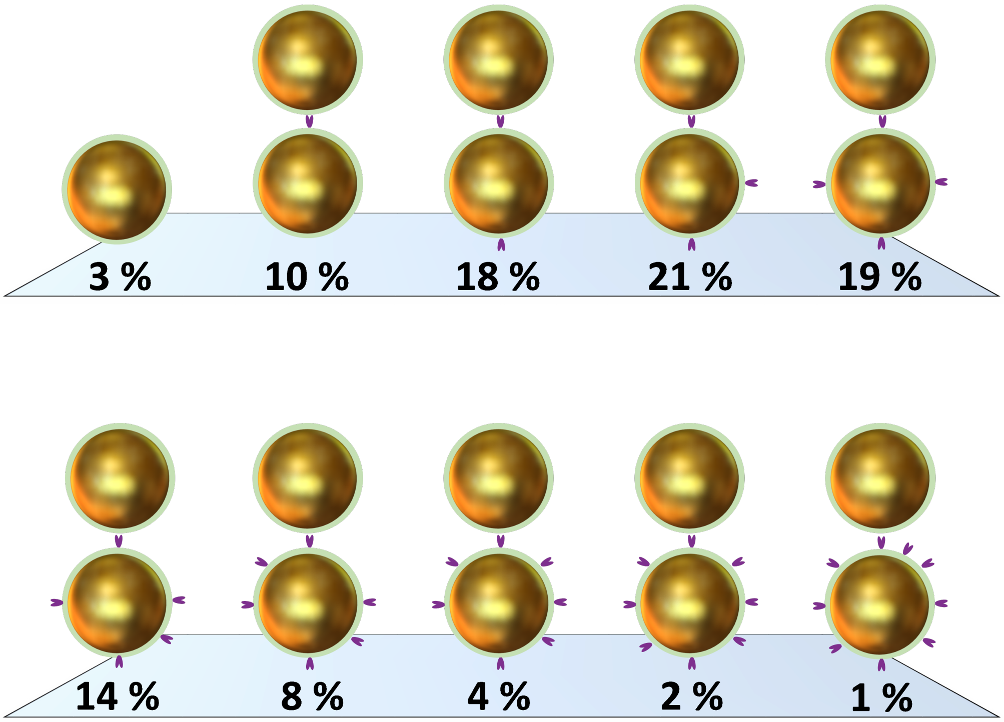

Figure 3.19: **Theoretical estimation of the distribution of the expected number of attached protein per plasmon ruler according to Poisson statistics.** Sketch drawn to scale of plasmon rulers functionalized with Hsp90 (violet) assuming a functionalization ratio of protein to plasmon ruler of $\lambda = 3.6$. The percentages given for each plasmon ruler correspond to the expected occurrence in the distribution (according to Poisson statistics, confer to **Section 3.2**).

Performing the assembly process fast and efficiently is the third challenge. The assembly route can either be carried out in solution or on a surface. Assembling dimers in solution allows the simultaneous preparation of plasmon rulers for many measurements, but purification of dimers from monomers and higher-order assemblies is necessary. It is unclear if a protein stays intact during purification schemes like gel electrophoresis or density gradient centrifugation. The assembly on a surface offers the following advantages compared to the assembly in solution: less by-products are formed because the surface offers steric hindrance, less amount of protein is needed and the prepared plasmon rulers can be directly measured. For these reasons, I choose to assemble plasmon rulers on a surface instead of in solution as in a previous work. [53] Therefore, I adapted the passivation strategy from previously used unspecifically adsorbed blocking protein [53] to covalently bound polymer chains. [80] This strategy enables the specific attachment of the first set of nanoparticles with anchor groups. The use of covalently bound polymer chains instead of adsorbed proteins, that could potentially come off, offers the advantage that less disturbance of the protein is likely.

In that previous work, before the assembly of plasmon rulers on a surface, the protein was coupled to the nanoparticles in solution exposing the protein to room temperature for $3\,h$. The protein was then frozen again and thawed later on the day of the experiment on which the protein was reduced for $1\,h$ before the coupling of the second particle for $2\,h$. In summary, the protein was exposed to room temperature for $6\,h$ with a freezing / thawing step in between before the start of the measurement. In this work, I attach the protein directly in the flow cell so that the protein stays at room temperature for only $1\,h$ before the start of the measurement (instead of $6\,h$).

I improved the dimer yield from previously 3 % to 20 % close to the highest possible yield according to Poisson statistics that is 27 % (see green line in **Figure 3.9**, assuming dimerization I use $k = 2$, where the highest probability is $P = 27\,\%$). I again decreased the salt concentration to $c\,(KCl) = 50\,mM$ during the measurement process in order to try preventing dimer aggregation.

In summary, my modifications of the assembly protocol lead to a higher dimerization efficiency during the assembly (20 % instead of 3 %). However, most of the assembled dimers do not show single-molecule protein fluctuations (similar to previous work, confer to **Figure 3.7**). [53] In this work, it was not possible to find a solution to the problem of non-fluctuating dimers. Possible reasons for the existence of non-fluctuating dimers include denatured proteins, still not optimal passivation, multiple linker formation or non-specific aggregation of particles without protein. I do not rule out the possibility of protein denaturation, but I find it unlikely since the protein is a heat shock protein relatively stable and only exposed to room temperature for 1 *h* before the measurement. Insufficient passivation seems an unlikely reason because optimization of passivation did not increase yield of fluctuating dimers. I cannot exclude multiple linker formation, but given the comparable experiments with PEG linkers, I find it highly unlikely. In my opinion, the non-specific aggregation of particles without protein is the most likely. In order to improve the yield of functioning dimers, future studies need to be carried out. One worthwhile endeavor, in my opinion, could be to modify the PEG linker with a small alkane unit resulting in a hydrophobic core around the nanosphere. [70] This hydrophobic core should be more protein-repellent compared to PEG possibly hindering protein denaturation.

4 DNA-HAIRPINS OPEN BY COMPLEMENTARY DNA

A partly self-complementary single DNA strand can hybridize with itself forming a loop, a so-called hairpin. Thus, the base pairs of the DNA strand are paired only partly leaving a loop of unpaired bases. Adding a short complementary strand will bind to the single-stranded part and, thus, open the loop resulting in an extension.

DNA hybridization, bending, cleavage and stiffness has been extensively studied with plasmon rulers (confer to **Section 1.2** for more details). [4, 6, 7, 21, 28] Further DNA hairpins were studied with plasmon coupling as core-satellites [82] and as dimers. [83, 84] However, the hairpins used are not specific to a relevant target.

Here I use plasmon rulers to determine the size increase of an opening of a hairpin by a target sequence, namely the gene sequence of the influenza virus subtype $H1N1$ ('Spanish Flu'). [85] My experiments measure the distance change to be 50 % less than the maximum theoretical extension according to the number of base pairs. Since our plasmon ruler measure a time averaged value, this suggests that the hairpin is not all the time folded. Indeed a room temperature melting is highly possible.

This study suggests that plasmon rulers are capable of determining the size increase of a DNA strand upon hairpin opening. Further moving these kind of static experiments into time-dependent dynamics measurement could give new insights on fundamental hairpin folding. Whether a DNA hairpin is folded or opened is crucial for proteins to recognize and bind to the DNA, processes directly related to e.g. replication, transcription regulation. [86]

4.1 PLASMON RULERS LINKED BY DNA CAN BE ASSEMBLED

I assemble DNA-linked plasmon rulers sequentially in a flow cell. DNA sequences are commercially available to be custom-made on individual orders including modification on either end. For the functionalization of the particles, I ordered one end to be thiolated and for the linkage to another particle the other end should be biotinylated.

In order to avoid unspecific binding to the glass surface of our flow cell, I pegylated the glass. Biotin anchors are included in the passivation layer to which nanospheres coated with streptavidin can bind and, thus, be immobilized on the glass surface (see **Figure 4.1A**). Next another batch of nanospheres coated with DNA and containing biotin groups on their exterior are bound to the streptavidin on the first nanosphere (because each streptavidin has four binding pockets for biotin).

The DNA linking the now assembled plasmon ruler is partly self-complementary forming a hairpin (see zoom-in in **Figure 4.1A**). The so arising loop is single-stranded and complementary to the gene sequence of the influenza virus subtype $H1N1$. [85] Hence, this DNA sequence can bind to the loop and open the hairpin.

In **Figure 4.1B**, I show the spectral effect of the comple-mentary strand opening the hairpin. The scattering spectrum of the folded hairpin (shown in yellow) will shift to lower wavelength when the hairpin is opened by its complementary strand (green spectrum) leading to an increase of inter-particle distance followed by the decrease of coupling efficiency.

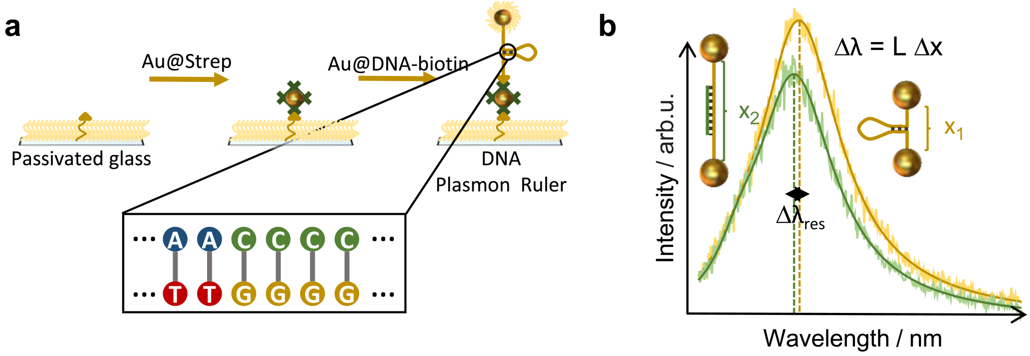

Figure 4.1: **Assembly and measurement principle of DNA-linked plasmon rulers.** a) Au@Strep nanospheres are immobilized on a passivated flow cell pegylated with biotin-anchors. Then Au@DNA-Biotin containing a folded hairpin binds specifically to the streptavidin on the first particle. b) The scattering spectra of the plasmon ruler linked by a folded hairpin (yellow) is shifted to lower wavelength when a complementary strand opens the hairpin (green spectrum).

4.2 THE RESONANCE WAVELENGTH SHIFT FOR DNA-OPENING IS SMALLER THAN EXPECTED

In order to check, if our dark-field microscope is working correctly, I first take a reference measurement of single particle scattering spectra of the immobilized streptavidin coated nanospheres. The resonance wavelength shift is negligible as expected (the first measurement in **Figure 4.2**).

The next measurement is another control to see if our dimer assembly, the plasmon ruler formation, takes place (the second measurement in **Figure 4.2**). Here I expect a red-shift of the plasmon resonance due to plasmon coupling of the pair of nanoparticles linked by DNA. The DNA is already folded in the hairpin structure when it attaches to the first nanoparticle.

When I incubate with the gene sequence of the influenza virus subtype $H1N1$, that is complementary to the single-stranded part of the DNA-hairpin, the loop will open forming double-stranded DNA. A significant size increase is expected accompanying the hairpin unfolding. This size-increase results in the blue-shift of the resonance wavelength of the plasmon ruler (the last measurement in **Figure 4.2**).

The amplitude of the plasmon resonance shift for the hairpin opening can be converted to the end-to-end distance change of the DNA. The conversion factor is the sensitivity of length change L (described in detail in **Section 2**).

In order to estimate L, I need to know the nanosphere diameter of the individual particles forming the plasmon ruler (here 40 nm) and the approximated inter-particle distance. The DNA length depends on the number of base pairs the DNA consist of (here 45 bp), with each base pair estimated to span 3.4 Å. Additionally, the size of the streptavidin that is also located in between the particle dimer needs to be taken into account. The diameter of streptavidin is approximately 6 nm. [87] In sum, I estimate the inter-particle distance to be around 210 Å. This leads to a sensitivity of length change $L = 0.1\ nm/\text{Å}$.

I determine the resonance wavelength shift of the hairpin opening to be 3.7 nm. The DNA length change is given by the following formula:

$$\Delta x = \Delta\lambda / \boldsymbol{L} \tag{4.1}$$

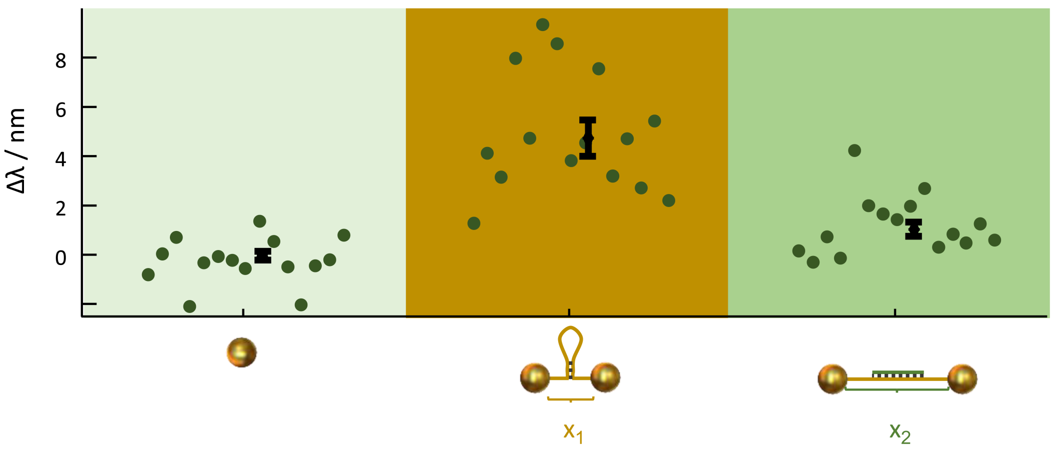

Figure 4.2: **Resonance wavelength shift of the unfolding of a DNA hairpin.** The shift in resonance wavelength against the individual reaction steps: First a reference measurement is recorded to check for instrument stability ($\Delta\lambda = 0.1 \pm 0.7\ nm$), then the dimer formation is conducted proven by a red-shift ($\Delta\lambda = 4.7 \pm 2.9\ nm$), and finally the complementary strand is incubated with the plasmon ruler whose opening is observed by a blue-shift ($\Delta\lambda = -3.7 \pm 1.7\ nm$, $n = 15$). Each dot represents the response of an individual plasmon ruler with the mean and its error (SEM) indicated by black symbols.

The approximate DNA length change upon hairpin opening determined by plasmon rulers is 37 Å. This corresponds to around 11 bp. In fact, there are 22 bp in the small complementary strand opening the hairpin. This disagreement can be explained with the help of the self-complementary part of the hairpin, only 6 bp resulting in a melting temperature of 20 °C. Since our measurement are conducted at room temperature, the hairpin is only folded half of the time. I measured here statically, averaged over time, thus, obtaining a value half the estimated one, is reasonable.

For future studies on DNA hairpins, it would be interesting to collect additionally time-traces to study their dynamic behavior.

4.3 CONCLUSION

I investigated the size extension upon DNA hairpin opening by hybridization with a small complementary strand with single-molecule plasmon rulers. The plasmon rulers were assembled in a flow cell with the help of the streptavidin biotin system.

The hairpin I used was complementary to the gene sequence of the influenza virus subtype $H1N1$. The approximate DNA length change upon hairpin opening determined by plasmon rulers is 37 Å. Here I only performed static measurements upon target binding, the flexibility of hairpins could be studied in timetraces in the future.

Since plasmon rulers have shown binding sensitivity up to single-molecules, [28] it would be possible to create a very sensitive assay. With hairpins reacting towards different targets, for example other influenza subtypes, a multiplexed detection scheme would be imaginable. [27]

5 POTASSIUM TRIGGERS A REVERSIBLE SPECIFIC STIFFNESS TRANSITION OF POLYETHYLENE GLYCOL

Polyethylene glycol (PEG) is a polymer widely used in pharmacy, medicine, and cosmetics by reason of its water solubility and its extraordinary high bio-compatibility. [88, 89, 90] So-called 'in-chain' pseudo-crown structures arise when PEG molecules self-assemble around some specific metal cations, e.g. potassium, in helical conformations, . [90, 91, 92]

In contrast to PEG, polyelectrolytes respond mostly unspecifically to ions resulting in a transition between compact and expanded states influenced mostly by the ionic strength of the solvent. [93] However, the reaction of PEG in response to cations it not completely understood, especially in respect to chain stiffness, conformation and hydrodynamic radius, if it responds specifically to definite ions or unspecifically.

In this work, ‡ I use plasmon rulers for observing the cation-generated conformational change and stiffness of PEG molecules. The end-to-end distance of a single PEG molecule is spectroscopically resolved with the help of plasmon rulers consisting of two plasmonic gold nanoparticles linked by PEG. [4, 44] Our results demonstrate that PEG stiffness strongly changes in the presence of potassium but not with sodium, proposing a specific PEG-cation interaction. Generalized intrinsic viscosity measurements support our single-molecule results.. In addition, we perform molecular dynamics simulations revealing that indeed 'in-chain' crown-like structures arrange around potassium ions (but not around sodium ions) leading to the observed reaction towards cations.

---

‡In this project, Dr. Rubén Ahijado-Guzmám synthesized and characterized the gold nanospheres. Weixiang Ye developed the setup and performed BEM simulations. I functionalized the individual nanospheres, assembled the dimers and passivated the glass substrate. I performed the measurements and the data analysis with the help of Weixiang Ye. I conducted the intrinsic viscosimetry measurements at WEE-Solve GmbH, Mainz and evaluated the data with help from Prof. Dr. Bernhard Wolf (Institute of Physical Chemistry, University of Mainz). The molecular dynamic simulations were performed by Dr. Giovanni Settanni and Prof. Friederike Schmid (Institute of Physics, University of Mainz). I coordinated the project and a version of this chapter is published as [51].

This specificity in the response towards potassium ions is an alluring opportunity in respect to the synthesis of 'smart polymers' responding to external environmental stimuli, for example in the context of electro- or opto-mechanical systems, tissue engineering, drug delivery and diagnosis. [94, 95] More generally, the discovered stimuli-responsive performance of PEG could act as model system, foldamer-like, for other more complex macromolecular transitions such as conformational changes and folding of proteins. [96, 97] The method I use here, single-molecule plasmon rulers, is an enticing tool for investigating such systems that has until now not been employed to the full extent possible. Resolving transient intermediate states and alternative folding pathways directly are possibilities for single-molecule plasmon rulers. Further the characterization of complex conformational dynamics of proteins could benefit tremendously from the plasmon ruler technique.

Other typical single-molecule techniques such as optical tweezers, atomic force microscopy (AFM) or fluorescence resonance energy transfer (FRET) can be potentially replaced by plasmon rulers to measure molecular distances. [4, 44] FRET endures from limited monitoring bandwidth (time resolution and total observation time) due to photo-bleaching and the biggest measurable distance is restricted to roughly 10 *nm*. [18, 98] AFM and optical tweezers generate a force on the molecule under investigation and, thus, extrapolation to zero-force is required for extracting equilibrium values. The applicable force spectrum in AFM is restricted due to the cantilever stiffness. The samples could be disturbed or destroyed by heating or photodamage because of the strong light fields applied in optical tweezers. [10, 99]

These drawbacks are likely tackled by plasmon rulers considering the lack of bleaching or blinking in plasmonic light scattering granting, in principle, unlimited observation times. The coupling of two neighboring plasmons in a plasmon ruler is the basis principle of the method. An increase in the interparticle distance results in a shift of the plasmon resonance wavelength of the coupled arrangement to higher frequencies ('blue shift') accompanied by a decrease of total scattering efficiency of the peak. The coupling efficiency of plasmonic particles decreases approximately exponentially as a function of distance with a typical decay length equivalent to around 0.2 times of the particle diameter.

[19] The molecular dynamics of a single macromolecule tether connecting the particle pair governs the plasmon resonance frequency. In principle, all metal nanoparticles exhibit plasmon resonances. Gold is chosen as material for the plasmonic nanoparticles in our plasmon rulers due to its high chemical stability, a resonance frequency in the visible spectrum, and the comparatively low damping.

5.1 PLASMON RULERS RESOLVE POLYMER EXTENSION

The diameter of the spherical gold nanoparticle forming the plasmon ruler is customized to the predicted molecular extensions of interest. Since the particle diameter of the respective single nanospheres also affects the plasmon resonance of the plasmon ruler, a low polydispersity among the nanospheres is necessary in order to convert the plasmon resonance frequency properly into molecular distance. Therefore, I employed a nanosphere synthesis method in our study known to yield a low polydispersity batches of gold spheres (Appendix **Figure 8.2**). [100] I observed a mean particle diameter $< D >= 52\,nm$ with a size diversity of $\sigma_D = 2\,nm$ in our batch. This size diversity amounted to about 4 % of the mean (polydispersity index $PDI = 1 + \sigma^2 / < D >= 1.0015$). This is less than in most nanoparticle synthesis strategies leading commonly to diameter variations of around 10 % (or worse). Further we consider the shape anisotropy dispersity of our sample (aspect ratio variation < 0.1). Both size variation and shape anisotropy culminated in a peculiarly tiny variation of the single particle plasmon resonance wavelengths λ_{res} of only 9 nm (standard deviation) around the median value of $\lambda_{res} = 561\ nm$.

In a plasmon ruler experiment, I need to connect a dimer of gold nanopsheres by a single macromolecule tether, with one of the spheres fixed on a translucent substrate and the second sphere should be mobile in a solution. I decided to form the dimers step-by-step in a microscope flow cell. In this way I was able to observe the assembly process in real time avoiding purification steps and facilitating the selective connection of only the first sphere to the substrate. In order to assemble dimers in a flow cell, I immobilized nanospheres from a first batch of particles on the glass surface (**Figure 5.1A**). After rinsing to get rid of the unbound excess of particles and blocking the remaining substrate surface, I introduced a second set of particles into the flow-cell, functionalized to connect specifically to the first particles. I oversaw the creation of dimers in the microscope, which is easily observable by a strong color change. As soon as an adequate amount of dimers was produced, I washed off the unreacted particles. Subsequently, I was able to exchange the liquid environment around the dimers for the investigation of macromolecular dynamics.

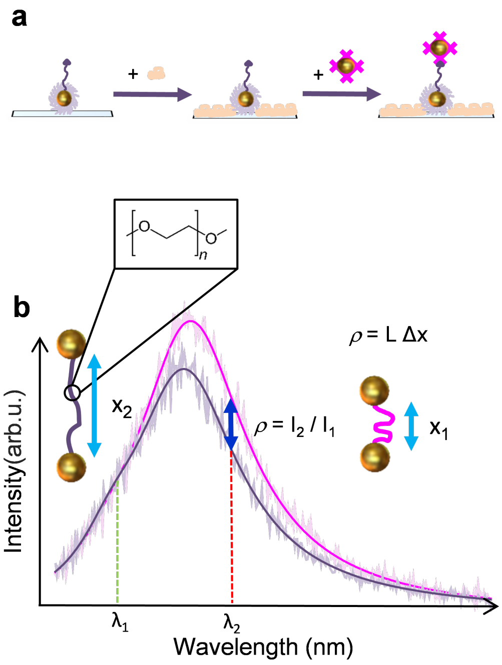

Figure 5.1: **Dimer formation and principle of measurement.** a.) Simplified step-by-step schematic illustration of the deposition strategy for the dimer formation in the flow-cell (cf. Appendix **Figure 8.3** for details). b.) Measured single particle spectra of dimers with a single PEG tether (inset) in a stretched (violet) and compressed (pink) configuration. Compared to the compressed configuration, the stretched configuration shows a red-shifted plasmon resonance of slightly higher intensity. The intensity change (ρ) at wavelength λ_2 (normalized and corrected for the value at wavelength λ_1) is approximately proportional to the change in interparticle distance $\Delta x = x_2 - x_1$ (cf. also Appendix **Figure 2.6** and **Figure 8.1**). Figure included in the manuscript accepted as [51].

I took the two batches of nanospheres forming the dimers from the identical stock of particles as mentioned above. The first particle set was functionalized with thiol-PEG-biotin and the other particle set with the protein streptavidin (see Appendix 8.3.2). [61] The immobilized biotin-PEGylated nanospheres on the substrate caught the streptavidin coated particles from the liquid environment due to the strong affinity of streptavidin to biotin. For the sake of avoiding multiple PEG molecules tethered between the two particles, I functionalized the first particle set with a mixture of biotin functionalized PEG and nonreactive methoxy-PEG, generally yielding a ratio of about $1:19$. To enhance the accessibility of the biotin, the biotin-PEG was somewhat more extended (3 vs 2 kDa) than the nonreactive PEG. Multiple linker formation could be avoided because the curvature of the sphere provided steric hindrance (see sketch drawn to scale Appendix **Figure 8.3**). [101] Due to this deposition strategy I was able to observe stretching and shrinking of single PEG macromolecules linking both nanoparticles in response to varying potassium and sodium ion concentration in the solvent.

In order to investigate the stiffness of the PEG molecule connecting the plasmon ruler (inset, **Figure 5.1B**), I determined the time-dependent distance changes $\Delta x(t)$ read out by the plasmon resonance wavelength. The stiffness of the linker is directly resolved by the measured distance fluctuations. Exemplary light scattering spectra of a single dimer in both stretched (inset left) and shrunk (inset right) configurations of PEG are shown in **Figure 5.1B**. As described before, a shorter tether induces a red-shift in the dimer spectrum with higher maximum scattering efficiency. Resolving the entire spectrum shown in **Figure 5.1B** solely before starting the experiment enables us to accelerate the determination of distance changes by only observing the intensities $I_1(t)$ and $I_2(t)$ at the two wavelengths λ_1 and λ_2 as indicated in **Figure 5.1B**. I exploit the transverse plasmon mode of the dimer, represented by the shorter wavelength (λ_1), as internal reference for the intensity because this mode is not influenced (much) by distance changes. After normalizing the intensities at λ_1 and λ_2 to their initial values $I_{norm}(t) = I(t)/I(t=0)$, I monitored the ratio $\rho(t) = I_{2,norm}(t)/I_{1,norm}(t)$ over time. I extracted interparticle distance changes $\Delta x(t)$ from the normalized intensity changes $\rho(t)$ with the help of a theoretical model similar to the one previously described (see Appendix **Figure 2.6**). [19] I simplified the translation valid for small fluctuations in interparticle distances Δx by introducing a linear conversion factor $L = \Delta\rho/\Delta x$ that is approximately $L \approx 0.03/nm$ in our system.

The experiments described above were carried out with a hyper-spectral imaging setup (shown schematically in Appendix **Figure 8.1**). With this setup, based on a white light laser in connection with an acousto-optical tunable (AOTF), I was able to switch between two operation modes: Alternating between all possible wavelengths, I resolved every spectra of all the particles in the field of view before starting the timetraces. In the next step, I rapidly switched the illumination between two wavelengths λ_1 and λ_2 acquiring fast timetraces in 'dual-line mode'. In this way, I determined the interparticle distance of up to 70 dimers simultaneously for many hours with a time resolution of 50 *ms* continuously.

5.2 DISTANCE FLUCTUATIONS ARE GOVERNED BY POLYMER STIFFNESS

I show an example of a timetrace of a single plasmon ruler tethered by a single PEG molecule in two different salt conditions in **Figure 5.2A** (purple-gray-pink line). In a particular salt concentration, I observed distance fluctuations around an equilibrium value by as much as ±3 *nm* in the graph. Similar timetraces are measured in parallel on dozens of dimers - on some of them no fluctuations were observed, possibly due to the unintended immobilization of both nanospheres on the glass surface. I exploit these 'control dimers' for determining our instrumental noise under the assumption that molecular fluctuations is not taking place in these dimers. The fluctuations monitored on a particle pair with one mobile sphere and one immobilized are much larger (10 *X*) than the fluctuations observed on 'control dimers' (see dark blue timetrace in **Figure 5.2A**). Another indication for a dimer governed by molecular fluctuation is the shrinking of the end-to-end distance of the PEG molecule in higher salt concentration. Therefore, I changed the salt concentration after 30 *min* from 0.1 *mM* to 10 *mM* and observed the shrinking and the fluctuation amplitude decreased simultaneously by a factor of about 2. Both observations substantiate the hypothesis that the shrinking of a PEG molecule is accompanied with higher stiffness. I rule out alternative explanation of fluctuations, for example instrument noise or particle surface coverage fluctuations.

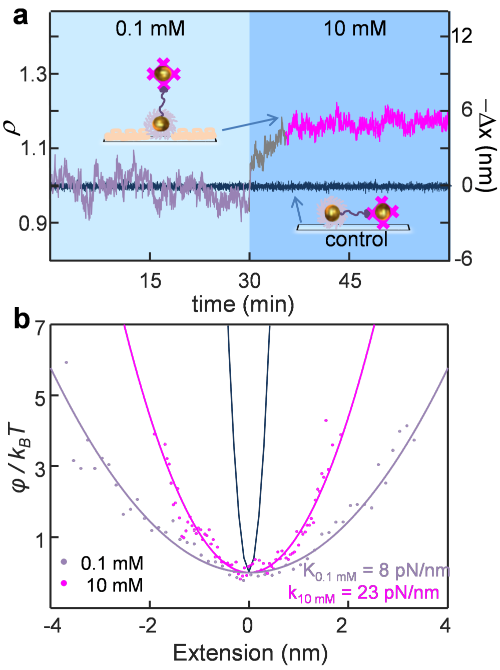

Figure 5.2: **Molecular stiffness from equilibrium fluctuations.** a.) Timetrace (purple, gray and pink line) of the normalized intensity ratio ρ (left axis) and corresponding interparticle distance change Δx (right axis) at two different K_2SO_4 concentrations (shaded areas) for a dimer connected with a single PEG tether. The dark blue line corresponds to the values measured on a 'control dimer' where both particles are immobilized on the substrate. b.) Interparticle potential φ as a function of fluctuation (extension) around the equilibrium value. The values extracted from the probability functions for the particle separation Δx shown in **Figure 5.2A** are shown as dots (color corresponds to the time sequences shown in **Figure 5.2A**). The measured values (dots) clearly follow two different trends as indicated by the fitted parabolas (lines in the corresponding colors). Figure included in the manuscript accepted as [51].

To determine polymer stiffness quantitatively from distance fluctuations, I consider a Boltzmann distribution underlying the probability distribution $P(x)$ of the interparticle distances given by a molecular potential $\varphi(x)$ (contributions from noise are disregarded here). [7, 102] I gained the potential $\varphi(x)$ from the probability distribution $P(x)$ of our timetraces by $\varphi(x)/k_BT = -ln(P(x))$.

The translated potentials for the two different salt concentrations used before (0.1 mM, violet, and 10 mM, pink) are shown in **Figure 5.2B**. A parabolic fit to $\varphi(x)$ yields the spring constant k, if I consider the potential stems purely from the stiffness of the molecular tether. These parabolic fits are represented as solid lines in **Figure 5.2B** together with the matching spring constants. The calculation are in agreement with the qualitative hypothesis presented above: a lower spring constant in the lower salt environment, consistent with a more flexible, extended polymer chain.

In order to demonstrate that the monitored fluctuations are determined by the properties of a single molecular linker, I designed additional control experiments. First, I ensured that the estimated spring constants are undisturbed by the gold nanoparticles' size and shape (as determined from the observed scattering intensity and wavelength) (Appendix **Figure 8.5**). Second, I established that the observed potential is governed by an individual molecular linker by curtailing the amount of thiol-PEG-Biotin on the nanoparticle from 5 to 0.5 %. Although this decrease adequately lowered, as expected, dimerization efficiency, the determined spring constants were not altered (see Appendix **Figure 8.6**).

5.3 K^+ ALTERS PEG STIFFNESS IN CONTRAST TO Na^+

After the ratification of our method, I characterized the stiffness of single PEG molecules as a function of potassium and sodium ion concentration. First, I carried out a step-wise titration of K_2SO_4 from 0.1 mM to 300 mM while monitoring the normalized intensities $\rho_i(t)$ of all 70 dimers in the field of view. In **Figure 5.3A**, I represent an exemplary timetrace $\rho_i(t)$ out of 70 in varying environments of K_2SO_4 concentrations as illustrated by the shaded areas. I checked for reversibility of the shrinking process after each titration step to exclude i.e. irreversible aggregation by a brief reversion to the initial conditions of 0.1 mM K_2SO_4. In fact, the expected signal level was reached after each concentration step, commonly within seconds (this reveals that our solvent exchange time is slower than attaining equilibrium after the appeared transition). The total reversibility was also demonstrated in another experiment, cf. Appendix **Figure 8.7**. I duplicated the titration experiment several times with various salt concentration steps. Since our dimers were notably inert against irreversible aggregation, I conclude that our approach of shorter polymeric spacer molecules passivating the leftover particle surface worked out.

I determined the linker stiffness of every dimer for each of the K_2SO_4 concentrations by evaluating the timetraces as described in **Figure 5.2**. The resulting stiffness values as a function of of K_2SO_4 concentration (small pink open circles) are depicted in **Figure 5.3B**. Averaging over all dimers, I obtained the mean values for each concentration (shown by blue dots) and observed a clear sigmoidal tendency with a transition to a stiffer, less extended state at higher salt concentrations. Approximating a sigmoidal function (blue line) to the mean values, I gained a critical transition concentration of $0.6 \pm 0.2\ mM$ (K^+ concentration $1.2 \pm 0.4\ mM$) and two conformations or 'states' with stiffness of $23.2 \pm 0.2\ pN/nm$ and $8.0 \pm 0.5\ pN/nm$.

In order to assess the soundness of our outcome, I confirmed the transition concentration with the help of literature results and an ensemble measurement (**Figure 5.3C**). Our literature search yielded a value of around 10 pN/nm, measured by single-molecule AFM, which agrees with the value determined in low-salt environment mentioned earlier. [103] In **Figure 5.3C** (see also Appendix **Figure 8.8**), I depicted the results of an ensemble measurement, namely the generalized intrinsic viscosity $\{\eta\}$ (hydrodynamic specific volume) as a function of the K_2SO_4 concentration as described by Xiong et al. [93] The values determined by our single-molecule plasmon rulers are validated by these ensemble data. An increase in the salt concentration induced a decrease in the specific hydrodynamic volumes within the studied concentration range and saturated at concentrations around 0.5 mM, consistent with the value determined above. The Huggings constants further support this (see Appendix **Figure 8.8**) varying as expected with the potassium concentration.

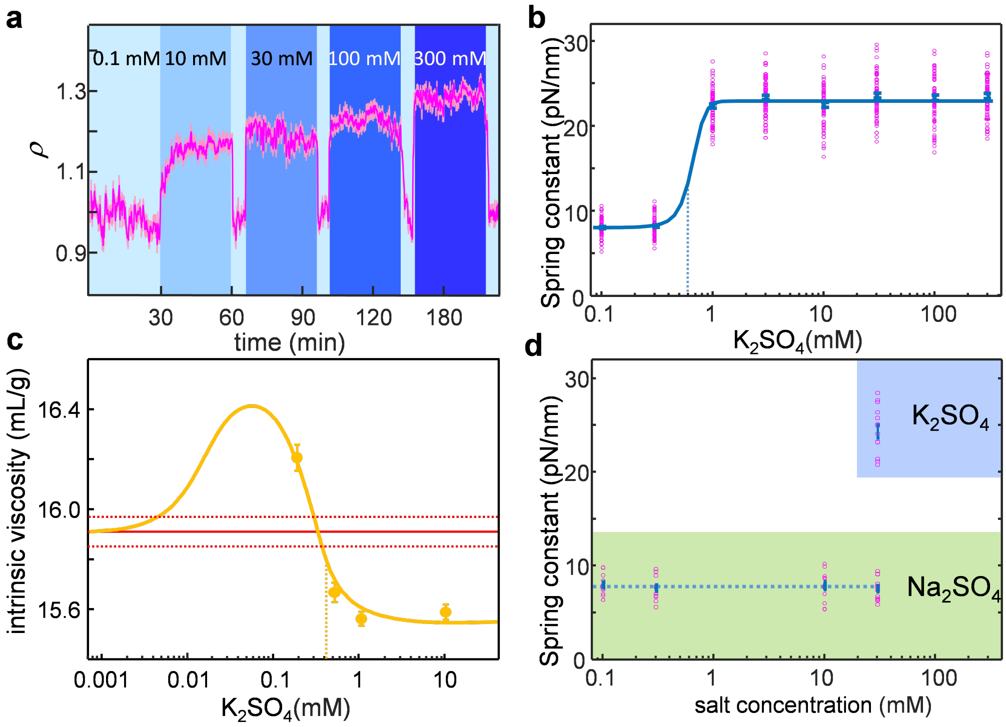

Figure 5.3: **Conformational transitions as function of salt concentration.** a.) Example of a timetrace of the intensity ratio $\rho(t)$ (left axis) and interparticle distance $\Delta x(t)$ (right axis) of a single plasmon ruler (pink line). The salt (K_2SO_4) concentration was changed every 30 min (shaded areas) to the values shown on top. Between every salt titration step I reverted back to 0.1 mM for a short time to test for the reversibility of the PEG shrinking process. I recorded about 70 such timetraces in parallel in each experiment. b.) The spring constants (left axis) calculated from pieces of timetraces shown in 'a' for different salt concentrations are show as small open circles. Their mean value for every salt concentration is shown as solid blue dot with error bars corresponding to the error of the mean. A sigmoidal function fitted to the data (solid blue line) shows a transition at 0.6 ± 0.2 mM (1.2 mM K^+ ion concentration). c.) For comparison, the intrinsic viscosity measured on free PEG molecules in solution. The orange line, to guide the eye, correspond to the expected intrinsic viscosity behavior. The dotted orange line shows approximately the transition in the intrinsic viscosity measurements at a concentration of around 0.5 mM which corroborates our single-molecule data. The red line indicates the intrinsic viscosity value in total absence of salt (pure water) and the dotted red lines correspond to the error of that measurement. d.) Same data as in **Figure 5.3B** but from an experiment with Na_2SO_4. At the end of the experiment, K_2SO_4 was added at 30 mM resulting in the same stiffness as shown before (panel above). Figure included in the manuscript accepted as [51].

Elucidating whether the detected stiffness transition in PEG is based on the ionic strength of the solvent or if it is specific to potassium ions, I contrasted K^+ to Na^+ reiterating the fluctuation experiment by titrating with Na_2SO_4 from low to high concentrations (**Figure 5.3D**). Shrinking of the PEG molecule or a transition of stiffness was completely absent within the investigated variety of concentration (up to 30 mM Na_2SO_4 corresponding to 60 mM Na^+). After the titration with the final Na_2SO_4 solution, I switched to a K_2SO_4 solution of identical concentration to verify the functionality of the plasmon rulers and that they are linked by an individual molecule of PEG as before. Positively, the presence of K^+ instantly induced a shrinking of the PEG accompanied with weaker fluctuations (higher spring constant). In summary, our experimental results propose a specific conformational transition above about 1.2 mM K^+.

5.4 DISTANCE FLUCTUATIONS ARE GOVERNED BY POLYMER STIFFNESS

To shed light on the detailed molecular mechanism underlying this specific potassium-induced PEG shrinking, we carried out atomistic classical molecular dynamics simulations. [§] PEG was simulated in pure water, in a liquid environment of 150 mM of potassium salt, and in the presence of 150 mM of sodium salt. These simulations were conducted for two different length of polymers (PEG18 and PEG36) ruling out effects stemming from varying polymer chain lengths because both polymers reacted similarly. We observed a size decrease of PEG in the proximity to potassium ions but not with sodium ions in the simulations (see the radius of gyration values in Appendix **Table 8.1**).

The structural details detected in the simulations lead to the conclusion of a strong coordination of the potassium cations to the oxygen atoms in the PEG chain, which not present for sodium (**Figure 5.4A**). The simulation snapshots in **Figure 5.4B** showed evidence that this strong coordination induced in-chain pseudo-crown-like patterns in PEG molecules around the potassium cations.

[§] The molecular dynamic simulations were performed by Dr. Giovanni Settanni and Prof. Friederike Schmid (Institute of Physics, University of Mainz). [51].

We do not exclude that sodium could potentially also form such patterns, but much more seldomly. In order to quantify this, we found that the probability to observe more than 3 PEG oxygen atoms around a cation is 100 times larger in the simulations at 150 mM K^+ than in the simulations at 150 mM Na^+ (12 % vs. 0.12 % of the trajectories). We attribute the shrinkage of the effective polymer length as a direct effect of the evolution of pseudo-crown patterns.

One possible explanation for the different reaction of PEG towards the two cations is based on the higher solvation free energy of Na^+ compared to that of K^+. [104] To enable the interaction of the cations with the oxygen atoms in the PEG molecule, the first hydration shell of the cations needs to be stripped off. This is remarkably easier for potassium ions than for sodium ions explaining the absence of the interaction with oxygen in the sodium case. Another contributing factor is related to the steric hindrance stemming from the bending of the polymer around a sodium ion which is smaller than a potassium ion. Thus, a lower degree of bending around potassium is needed favoring this energetically over sodium ion. [90, 105]

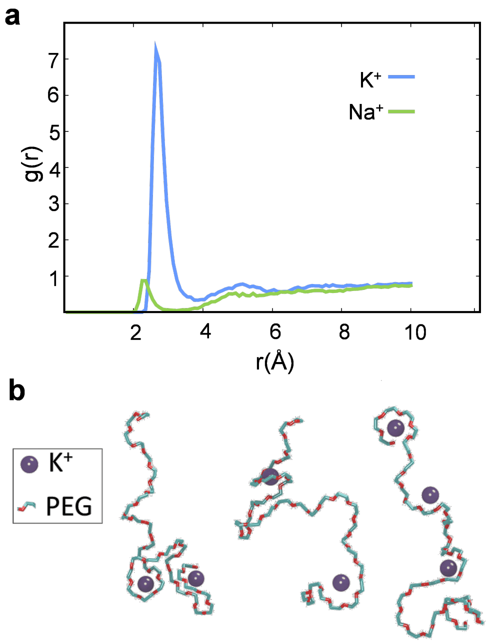

Figure 5.4: **Results from Molecular Dynamics simulations.** a.) The radial distribution functions of potassium (blue line) and sodium (green line) cations as function of distance to the oxygen atoms of the PEG chain. The strong peak at about 2.5 *Å* observed for potassium but not sodium suggests a much stronger coordination to PEG. b.) Coordination of potassium ion in three representative snapshots from the simulations shows the pseudo-crown pattern around the potassium cations. Figure included in the manuscript accepted as [51].

5.5 CONCLUSION

investigated the shrinking and stiffness of polyethylene glycol (PEG) in different salt concentrations with single-molecule plasmon rulers showing their pico-Newton sensitivity, in the same order as other single-molecule techniques like AFM or optical tweezers. [10, 99] An advantage of plasmon rulers in comparison to Förster resonant energy transfer (FRET) is their working range at much farther separations [18, 98] and the possibility to record timetraces with, in principle, indefinite length - without bleaching, blinking, and rotation.

For the validation of our method, I thoroughly proved that our plasmon rulers are linked by single molecules and showed that the polymer equilibrium conformation is unaffected by the nanoparticles. Using plasmon rulers and molecular dynamics simulations, I discovered a potassium-triggered specific transition supported by the underlying molecular mechanism of the evolution of crown-like patterns caused by the binding of potassium ions to the oxygen atoms in PEG. This work will pave the way to install plasmon rulers as a regularly used technique for the investigation of structural dynamics of single macromolecules in polymer, soft-matter, biophysical, biochemical, and bio-medical science.

6 HSP90'S CONFORMATIONAL CYCLE HAS THREE DECAY CHANNELS

The conformational dynamics of proteins are essential to understand their molecular specific role in living organisms. [106] Heat-shock protein 90 (Hsp90) is an essential molecular chaperone regulating important cell processes, e.g. tumor suppressor factors, steroid hormone receptors and protein kinases among others. [59] Its function is attributed to Hsp90's large thermally induced conformational changes (about 4 *nm*) on the timescale of a few seconds. [2, 3, 107, 60]

Ensemble techniques are unable to resolve protein dynamics due to their inherent averaging over many unsynchronized molecules. Thus, single-molecule techniques are necessary to resolve protein dynamics, e.g. using fluorescence resonance energy transfer (FRET). [108] However, this technique suffers from photobleaching limiting the maximum observation time to the lifetime of the employed fluorescent dyes. Hence, conformational transitions lasting longer than the dye lifetime are impossible to resolve.

In this work,[¶] I monitor Hsp90's conformational changes using plasmon rulers. Our plasmon rulers consist of two plasmonic gold nanoparticles linked by a single Hsp90 protein monitoring spectroscopically the end-to-end distance over time.

Our measurements are able to resolve conformations (dwell times) lasting longer because I can monitor a single protein up to 6 *h*. The longest dwell time recorded under thermal conditions was around 10 *min*, one order of magnitude longer than the FRET observation time limit (approx. 3 *min*). Although the events longer than FRET limit are very rare (corresponding to 1 % of all events), these events are not predicted by the proposed four state model con-

---

[¶] In this project, Dr. Rubén Ahijado-Guzmám synthesized and characterized the gold nanospheres. Weixiang Ye and Sirin Celiksoy developed the setups. I developed the functionalization and assembly strategy for the dimers. Glass slide passivation was carried out either by Julia Ricken from the group of Dr. Seraphine Wegner (MPI-P Mainz & University of Heidelberg) or by me. I assembled the dimers for the measurements and performed the measurements and the data analysis with the help of Weixiang Ye and Sirin Celiksoy. The protein (Hsp90) was expressed by Markus Götz from the group of Prof. Thorsten Hugel (University of Freiburg). I coordinated the project and a version of this chapter is in preparation for publication as [109].

sisting of two states corresponding to the closed conformation and two states corresponding to the open conformation. The new discovered long dwell times in my thesis need to be described by adding a third state for each conformation as I propose here.

Understanding the fundamental origin of conformational changes could help in multiple applied research areas like drug design, protein engineering or molecular evolution. For example, the determination of the dynamic conformational changes at the single-molecule level can directly resolve the inhibition of Hsp90 as one potential target for chemotherapeutic drug research. [110, 111] In addition to direct applications, the molecular mechanism of the dynamics is of fundamental interest. [112]

6.1 PLASMON RULERS LINKED BY A SINGLE PROTEIN (HSP90) ARE PREPARED ON A GLASS SURFACE

For the preparation of our plasmon rulers, I need to connect two gold nanospheres by a single Hsp90 protein with only one sphere attached to the microscope glass slide and the other sphere free to move. I assemble the plasmon rulers in a microfluidic flow cell because it helps to avoid purification steps (for a comparison of advantages and disadvantages of the plasmon ruler preparation methods see **Section 3.3**).

One challenge to extend plasmon rulers from simple macromolecules to proteins is the strong tendency of proteins to attach unspecific to unprotected gold and glass surfaces. In addition, proteins are not as chemically robust as DNA and polymers, reducing the choice of coupling schemes and the time available for the assembly process. Furthermore, the total particle separation should be kept at a minimum as the plasmon ruler accuracy decreases quickly with interparticle distance. [19]

In order to avoid denaturalization of the protein on a solid surface, [113] our nanoparticles are covered by a soft layer consisting of PEG. To avoid unspecific binding of the nanospheres to the glass, I pegylated the glass surface with a mixture of methoxy-PEG and biotin-PEG. Here the biotin molecule serves as an anchor point for the specific attachment of the first sphere to the glass surface.

I first deposited nanospheres from a first batch of particles specifically to the glass surface employing the Streptavidin-Biotin-interaction (see **Figure 6.1** and for experimental details confer to Appendix **Section 8.4.1**).

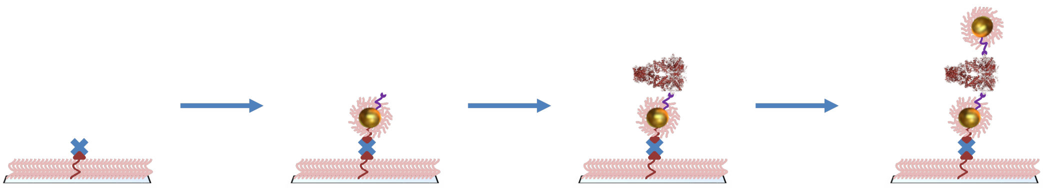

Figure 6.1: **Assembly of Hsp90-linked plasmon rulers.** Simplified step-by-step schematic illustration of the deposition strategy for the dimer formation in the flow-cell. The glass surface of the microscope slide is coated with Si-PEG to avoid unspecific binding of the nanospheres. Streptavidin serves as anchor point for the specific attachment of the first nanosphere. The second nanosphere is then linked to the first via Hsp90. Hsp90 sketch adapted with permission from [60].

Common coupling strategies such as DNA-hybridization or the streptavidin-biotin system are not suitable for Hsp90. Hsp90 binds unspecifically to DNA-coated gold nanospheres (see Appendix **Figure 8.9**). The addition of two streptavidin proteins to the plasmon ruler construct would increase the interparticle distance by 10 *nm* worsening plasmon ruler sensitivity. Instead, I use PEG linkers modified with amino-groups that can be coupled to Hsp90. Hsp90 bears two thiol-functionalities, one of them is coupled to the immobilized nanoparticles with Thiol-Maleimide-chemistry. A second batch of particles is maleimidated, introduced into the flow cell reacting to the second thiol-function of Hsp90. [53] The challenge in this procedure lies in the last step where the second particle is supposed to bind only to the first particle (via a single protein as connector) and not to the glass surface (see **Section 3.3.2**).

The two batches of nanospheres used to create the dimers were taken from the same stock of particles (see Appendix **Section 8.3.1**). Both batches of particles were functionalized with mixtures of different PEG-Thiols. The first batch bears biotin, methoxy and amine-functionalities and the second batch only methoxy and amine-functionalities.

In order to ensure that only a single Hsp90 protein connects the two particles, I have attached a mixture of amino functionalized PEG and nonreactive methoxy PEG to the first batch of particles. I tested different ratios of protein concentrations and chose a concentration where only 20 % of the monomers reacted to form dimers. Further, I also varied the salt concentration of the measurement buffer. Here, I encounter two opposing effects: Lower salt concentration avoids particle aggregation whereas the protein should be more stable in higher salt concentration. Indeed, I find a medium concentration working best (see **Section 3.1.2** and **Figure 3.7**). This deposition strategy allows monitoring the conformational dynamics of a single Hsp90 attached to both nanoparticles.

6.2 CONFORMATIONAL CHANGES ARE DETERMINED FROM THE PLASMON RESONANCE OF THE PLASMON RULER

To study the conformational dynamics of Hsp90 linking the plasmon ruler, I need to record the resonance wavelength as a function of time and convert it to conformational changes through the estimation of the interparticle distance. The resonance wavelength changes are assigned to the two possible conformations of Hsp90. Typical light scattering spectra of a single dimer in both conformations of Hsp90, open (inset left) and closed (inset right), are shown in **Figure 6.2A**. As discussed before, a shorter linker leads to a more red-shifted spectra with higher maximum scattering efficiency. To measure conformational changes quickly, I determined the entire spectrum shown in **Figure 6.2A** only at the beginning of the experiment and then monitored the intensity at a single wavelength (approximately at the line-width of the plasmon resonance peak) as indicated. The setup used here is similar to one previously used in another context [114] and described in more detail in Appendix **Section 8.1**. However, the amount of data recorded in this scheme ($2\,TB$ for a $6\,h$ experiment at $100\,ms$ resolution) quickly becomes a limiting factor for currently available hard drives. To overcome this problem, we reduced the data while recording by saving only the pixels related to particles, resulting in $4\,GB$ of data for a $24\,h$ recording at $20\,ms$. Furthermore, we increased the maximum recording speed by switching from a flexible light source (white light laser coupled to a tunable filter, $8\,mW$) to a fixed wavelength LED with higher intensity ($35\,mW$).

Taken together, the setup and data handling improvements introduced in this work increase the available recording bandwidth more than 3 orders of magnitude compared to previous reports. [7] The performance of the setup is shown in Appendix **Figure 8.10**. [||]

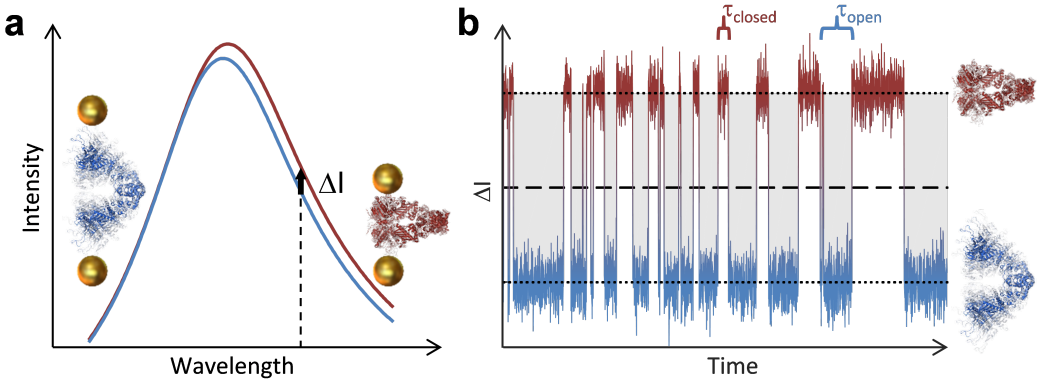

Figure 6.2: **Spectra of Hsp90-linked plasmon rulers in open and closed conformation.** a) Measured single plasmon ruler spectra linked with a single Hsp90 protein (inset) in open (blue) and closed conformation. The closed protein conformation leads to a red-shifted plasmon resonance with higher intensity compared to the open protein conformation. The intensity change (ΔI) is measured at a single wavelength. b) Timetrace (red and blue line) of the intensity change ΔI (left axis) and corresponding protein conformation (right axis). The black dashed line corresponds to the medium value and the two black dotted lines represents the two protein conformations. The time intervals in between conformational transitions are referred to as dwell times, τ_{open} and τ_{closed}, respectively. Hsp90 sketch adapted with permission from [60].

The intensity change ΔI at our measurement wavelength was monitored over time with the respectively higher intensity level corresponding to the closed and the lower level to the open protein conformation. A typical conformational cycle of the protein Hsp90 is shown in **Figure 6.2B**. I define dwell time as the time interval in which the protein stays in a specific conformation. Thus, I can define two dwell times as τ_{open} and τ_{closed}.

[||] Setup developed by Weixiang Ye and Sirin Celiksoy.

6.3 NOT ALL PROTEIN PLASMON RULERS ARE FLUCTUATING

In order to prove that Hsp90's random fluctuations can be monitored by plasmon rulers, I need to show that plasmon rulers linked by Hsp90 fluctuate with higher magnitude than control plasmon rulers. These fluctuation should follow a two state behavior, in which the closed conformation is less frequently occupied compared to the open one.

I first identified dimers in our flow cell by recording the spectra of all nanoparticles in our field of view with a hyper-spectral imaging setup (see **Section 8.1**). I found 325 dimers in our field of view with resonance wavelengths above 570 *nm*.

Then I switched the setup configuration to a single line mode imaging with ten frames per second with the illumination wavelength at 632 *nm*. Thus, I recorded so-called timetraces in parallel for 6 *h*. Many of the investigated dimers did not show typical Hsp90 transitions, but only noise, for example the timetrace shown in **Figure 6.3A** (top, left). A typical timetrace with fluctuations attributed to Hsp90 can be found in **Figure 6.3A** (bottom, left).

Ideally, all of our plasmon rulers should be linked by a single Hsp90 protein and, thus, fluctuate accordingly. A non-fluctuating so-called 'noise' dimer can be formed by various reasons. Two nanoparticles could be linked only by PEG without Hsp90. Hsp90-linked dimers could include a denatured, non-fluctuating protein. If two Hsp90 proteins whose fluctuations are not synchronized bridge the dimer, I would also observe 'noise'. Further either the glass passivation or the nanoparticle surface passivation was not perfect immobilizing both nanoparticles of the dimer on the glass surface or on top of each other hindering fluctuations.

In order to filter the fluctuating dimers from the non-fluctuating dimers, I used the shape of the histograms of the timetrace as a criterion to select dimers showing Hsp90 fluctuations. In case of a dimer only showing measurement noise, the histogram of the timetrace (**Figure 6.3A** (top, right)) is shaped as expected for Gaussian noise. In the other case of a Hsp90 dimer, the obtained histogram (**Figure 6.3A** (bottom, right)) is bisected. I approximated a Gaussian distribution function to the histograms and determined the coefficient of determination R^2. The maximum value of R^2 is 1, meaning the data points are approximated well by the chosen fitting function. Hence, I expect R^2 to be close to 1 for 'noise' dimers because their histograms should be a Gaussian distribution. Dimers with Hsp90-like fluctuations are expected to be skewed resulting in a significantly lower R^2-value. In **Figure 6.3B**, I depict the R^2-values for all possible 325 plasmon rulers, from which 4 are observed with a low R^2-value. These 4 dimers are expected to show Hsp90 fluctuations. Since there are typically a few hundred dimers within the field of view, this low efficiency was still enough to reliably obtain single molecule data.

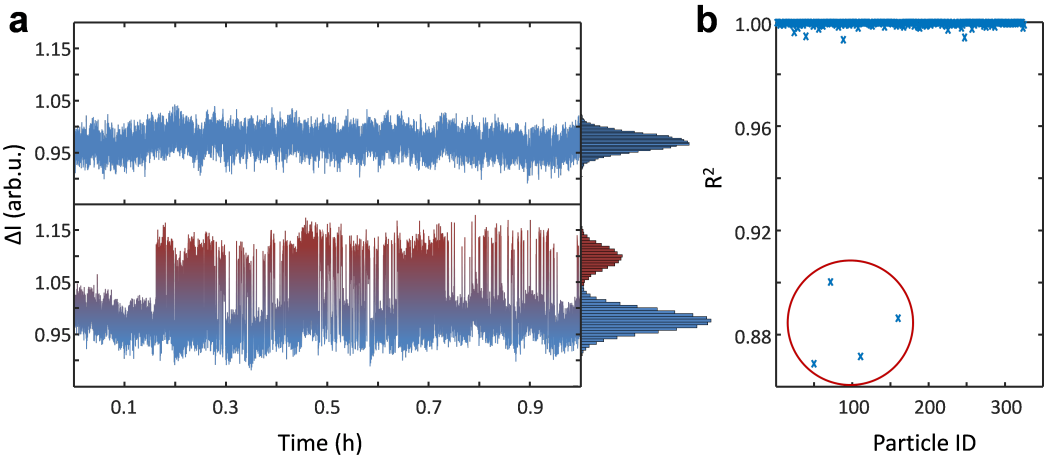

Figure 6.3: **Selection of plasmon rulers for Hsp90.** a) Timetraces (left) of a dimer showing no conformational transitions (top) and of a dimer with typical transitions (bottom). The corresponding histograms (right) show a bisected histogram for the dimer with transitions (bottom) which is not the case for the dimer without transitions (top). b) The histograms shown in **Figure 6.3A** are approximated by a Gaussian function and the respective coefficient of variation (R^2) is determined as a higher value for dimers with no transitions and a lower value for dimers with transitions. Conformational changes of the protein are observed on 4 out of 325 measured dimers.

6.4 SOME PROTEIN PLASMON RULERS ARE FLUCTUATING

Four of the plasmon rulers showed random fluctuations lying above our experimental noise level. I focus on those dimers (usually around 1 %) for further analysis. I monitored the conformational transitions of Hsp90 in apo-configuration (without nucleotide present) for 6 h with 10 fps (frames per second) as depicted in **Figure 6.4**. Additional timetraces recorded for 24 h are shown qualitatively in Appendix **Figure 8.11**. Here, I detect long extended periods of time where the molecule seems to be stuck in either the open or the closed configuration.

As a control experiment, I incubated the same plasmon rulers as above for 10 min with buffer containing 2 mM AMP-PNP (5'-adenylyl-imidodiphosphate), a non-hydrolyzable analog of ATP (adenosine triphosphate).

AMP-PNP is known to lock Hsp90 in its closed conformation. [3] I recorded timetraces for additional 40 min under AMP-PNP conditions and, indeed, I observe the expected clear shift of the equilibrium with Hsp90 occupying predominantly the closed conformation (confer to Appendix **Figure 8.12** and Appendix **Table 8.2**). This result is an essential control proving that the fluctuation stem from the protein because the expected behavior of Hsp90 is observed.

6.5 HSP90 PLASMON RULERS CONFIRM FRET-RESULTS

Previous FRET measurements have suggested a model for Hsp90's conformational cycle consisting of two states describing the closed conformation and two states assigned to the open conformation. [2, 3, 60, 115] The four-state model suggested before described each conformation by a double exponential function (with two dwell times). In our results, I compared double and single exponential and I obtained a better description by using the double exponential model.

In order to confirm the model suggested by FRET, I estimated all dwell times of the open and the closed conformation, respectively, using the Matlab-function 'pulsewidth' (as described in **Figure 6.2B**). I attributed the higher intensity level to the closed conformation of Hsp90 and the lower intensity level to the open conformation, taking the average intensity value as threshold. The

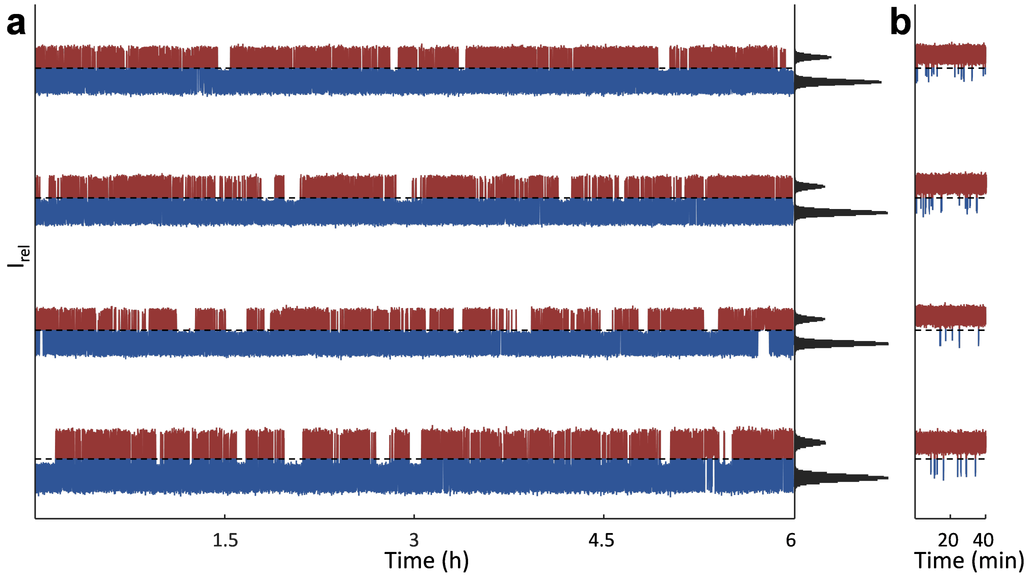

Figure 6.4: **Selected timetraces for Hsp90.** Timetraces of the 4 selected dimers (cf. **Figure 6.3B**) showing typical conformational transitions of Hsp90 that are monitored for 6 h with a time resolution of 10 fps.

time difference between two transitions of the threshold was defined as dwell time. In total, I accumulated over $12,000$ dwell times for each conformation from the four plasmon rulers investigated in apo-condition for 6 h with 100 ms time resolution yielding a total observation time of 24 h.

The dwell times are statistically distributed with no correlation between successive transitions (see Appendix **Figure 8.13**). The most proper way to deduce the underlying states and their transition rates, is the Hidden Markov analysis, [116] which finds the most probable sequence of states and their transition rates describing the observed dataset. However, a Markov analysis needs the number of states as an input parameter. In order to see if the previously described four-state model (two states in the closed and open state, respectively) is able to describe our new data, I look at the cumulative dwell time distribution in **Figure 6.5A**. To extract the rate constants of the conformational changes, I approximated an exponential decay function to the cumulative dwell time distribution. The decay times describing the open conformation are longer in respect to those belonging to the closed conformation, as described before. [3] The obtained decay times are in good agreement (same order of magnitude) with the FRET-values shown in **Figure 6.5B** and Appendix **Table 8.2**. [115]

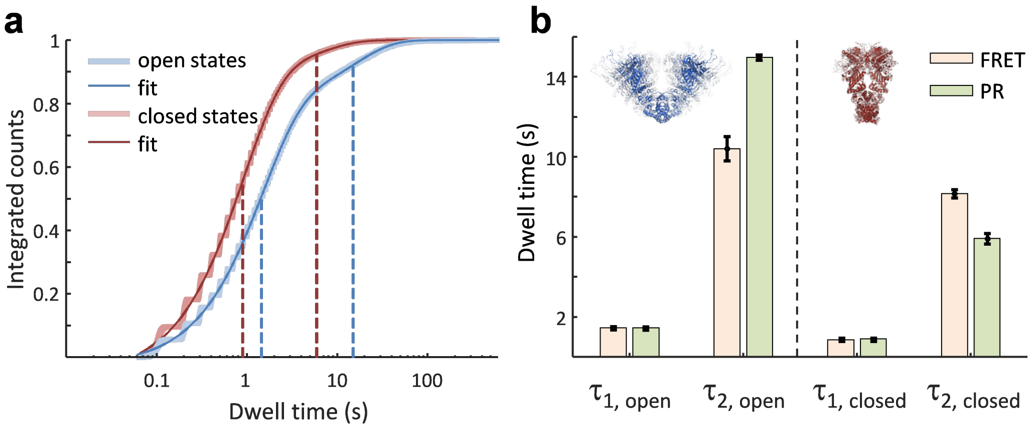

Figure 6.5: **Thermal dwell times of Hsp90 compared with FRET.** a) Cumulative dwell time distribution for open state (blue) and closed state (red). Dwell times are obtained as shown in **Figure 6.2B**. The dwell time distribution is approximated with a double-exponential decay function (lines in the corresponding colors) from which two mean dwell times for each conformation are extracted (dashed lines in the corresponding colors). Individual dwell time distributions for the four measured plasmon rulers are displayed in Appendix **Figure 8.14**). b) Bar plot comparing the extracted dwell times with the plasmon ruler method (green) and FRET (orange, values published). [115] Errorbars represent the uncertainty of the fitted function. Hsp90 sketch adapted with permission from [60].

Compared with FRET, the use of plasmon rulers offers more advantages, for example, the study of a single protein within a population of proteins with high statistics. For FRET-measurements the observation time and, thus, the amount of data from a single protein is limited, making necessary to measure a high amount of them. For our method, this is indeed possible, but not a requirement, possibly gaining new insights on the heterogeneity within a population of the same protein.

Since I probed four single proteins each with its equivalent plasmon ruler for 6 *h* with a time resolution of 100 *ms*, I can extract the dwell times from the individual cumulative dwell time distribution (displayed in Appendix **Figure 8.14** and Appendix **Table 8.3**). The first decay dwell times of both (open and closed) conformations are in the range of our time resolution (100 *ms*). These fast processes show no inherent heterogeneity within the population. On the other hand, both time constants for the second decay are in the order of a few seconds.

Although our data does not contradict the four-state model previously suggested, I found additional longer dwells inaccessible by FRET due to its limited observation time. The percentage of individual dwell times above the mean value was 8 % and 5 % for the open state and the closed state, respectively.

6.6 A THIRD DECAY CHANNEL INACCESSIBLE BY FRET IS DETECTED

The biggest advantage of our plasmon rulers compared to FRET is the, in principle, unlimited observation time. To find out, if and how much dwell times are missed studying the conformational dynamics of the molecular machine Hsp90, I searched for dwell times that are not reachable by FRET. The bleaching of the fluorescent dyes in FRET limits the maximum observation time depending on the exposure time. Assuming the same framerate as used in our plasmon ruler experiments, the longest existing dwell time in our data set (623 *s*) is inaccessible by FRET.

The long dwell times of around 10 *min* I found are not very common, thus, are not easy to visualize in the cumulative dwell time probability P (referred to as 'Method 1', confer to **Figure 6.5A**). Hence, I searched for other common ways to represent dwell time distributions.

One possible method is taking the logarithm of the probability ($-ln\,(1-P)$) against the dwell times ('Method 2'). Each decay channel is depicted as a linear function with the slope corresponding to the specific dwell time. In **Figure 6.6A,B**, I applied this method to our dwell time distribution for the closed (**A**) and for the open (**B**) conformation. For the slope of the linear functions describing the first two decay channels (green and violet lines in **Figure 6.6A,B**), I used the values extracted from the double-exponential decay function in **Figure 6.5A**. These two linear functions were not able to describe dwell times longer than about 50 *s*, since the data points clearly deviated from the linear trend lines. Thus, a third linear function was needed indicating a previously undetected third decay channel. The values for the third decay channel were determined by the slope of the third linear function (for values confer to **Table 6.1**).

Another possible method to represent the dwell time distribution is described in the literature. [117] Here, the logarithm of the dwell times is divided in equal bins and the resulting histogram is approximated by **Formula 6.1** ('Method 3'). In our case, *n* value was 3 as depicted in **Figure 6.6C,D**.

$$\sqrt{counts} = \sum_{i}^{n} a_i \cdot exp\left[(t-\tau_i) - exp\left(t-\tau_i\right)\right] \tag{6.1}$$

With Method 2 and Method 3, it was possible to extract long lasting conformations, hidden in Method 1. In **Table 6.1**, I show the obtained dwell times by the three different methods presented above. Using the determined dwell times as input parameters, the data distribution represented as Method 3 for a simulation gives a similar distribution (see Appendix **Figure 8.15**).

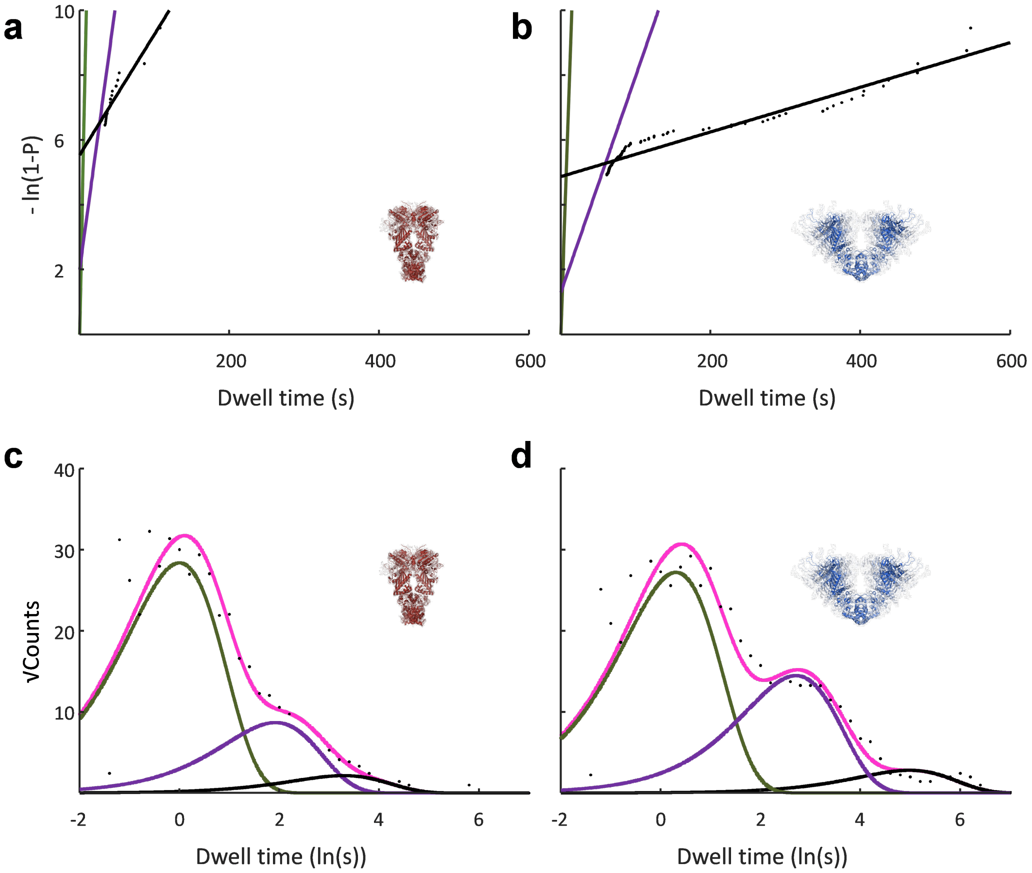

Figure 6.6: **Detection of third dwell time not accessible by FRET.** a,b) Logarithmic cumulative dwell time distribution for closed state (a) and open state (b). The first (green) and the second (violet) dwell time are shown as linear lines with the values from **Figure 6.5A**. The data points shown as black dots clearly deviate from a model with two decay channels. The third dwell time is extracted from the fitted linear function shown as black line. c,d) The square root of counts against logarithmic bins of the dwell time for closed state (c) and open state (d) shown as black dots. Each decay channel is described by the function $\sqrt{counts} = a \cdot exp\left[(t-\tau) - exp\left(t-\tau\right)\right]$. [117] The fitted functions for the first (green), second (violet) and third decay (black) and the sum of the functions (pink) are shown as lines. The data points above $exp\left(4\right)\ s \approx 55\ s$ are not represented by the functions for the first two dwell times, thus, the third fitted function is required. Hsp90 sketch adapted with permission from [60].

Table 6.1: **Comparison of dwell time extraction methods for apo-conditions.**

	open			closed		
	τ_1 / s	τ_2 / s	τ_3 / s	τ_1 / s	τ_2 / s	τ_3 / s
Method 1	1.44	15.0	-	0.90	5.90	-
Method 2	-	-	145	-	-	26.9
Method 3	1.36	15.0	146	1.00	6.83	26.8

6.7 ATP Accelerates Hsp90’s Transitions

Although Hsp90 is known to hydrolyze ATP (adenosine triphosphate), the energy supplier in cells, it is unclear how the hydrolysis of ATP influences the conformational cycle of Hsp90. [3, 107] Previous studies suggest a mild speed increase of the transitions for the employed four state model (dwell times are decreased by a few seconds).

Since I have now confirmed that a third previously undetected third state for each conformation exists (’six state model’), the influence of ATP on our new model is unknown. Therefore, I incubated a Hsp90 plasmon ruler with 5 mM ATP and monitored the conformational transitions for a total of 3 h (see **Figure 6.7A**). The dwell time analysis was carried out according to the three methods described in the previous section.

I used Method 1 to compare with the FRET-values from literature (confer to **Figure 6.7B** and Appendix **Table 8.2**). [115] The dwell times obtained by FRET and plasmon rulers matched except $\tau_{2,closed}$, that was significantly longer in the FRET measurement.

With the help of Method 2 (**Figure 6.7C,D**) and Method 3 (**Figure 6.7E,F**), I found that the six state model describes the dwell time distribution better than the four state model. This is for example evident in **Figure 6.7D**, where the black linear function clearly deviates from the violet one which is not able to describe the dwells shown as black dots. This result suggest, that the presence of ATP increases the conformational dynamics velocity. Thus, I found that the longer dwell times in the presence of ATP are around 180 s, while in the absence of ATP these were around 600 s. In both cases, I observed a six states, indicating that ATP is not hindering state transitions. The effect of ATP on the transition times was an overall decrease, especially for the states with the longer transition times. The stronger response of the long-living states to ATP could indicate a connection of the long lived third state with ATP hydrolysis. A complete molecular model of the Hsp90 dynamics will require a systematic investigation of mutants with different ATPase activity.

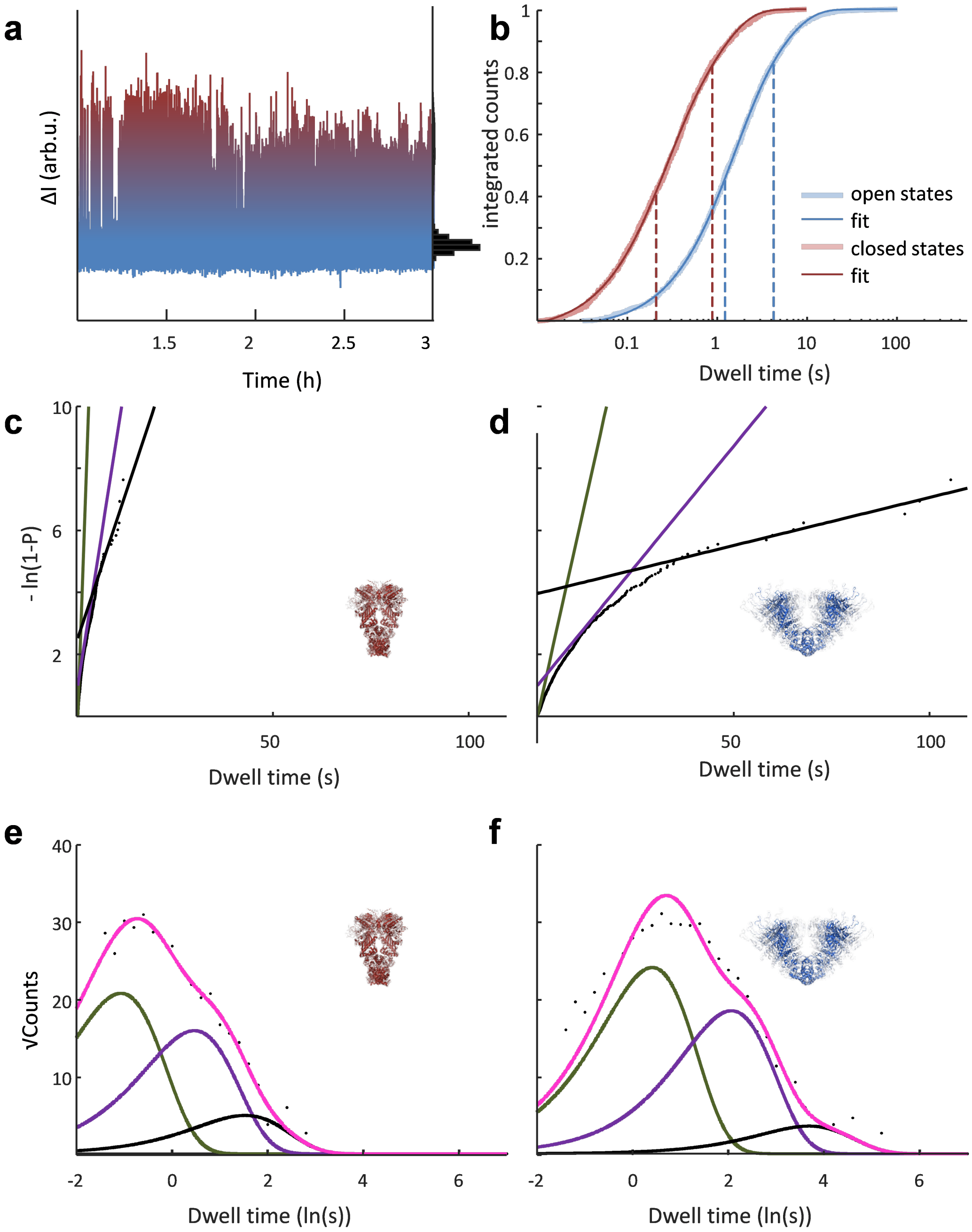

Figure 6.7: **Influence of ATP.** a) Timetraces of a dimer incubated with 5 mM ATP showing typical conformational transitions of Hsp90 that is monitored for 3 h with a time resolution of 30 fps.

b) Cumulative dwell time distribution for open state (blue) and closed state (red) under ATP-conditions. Dwell times are extracted as shown in **Figure 6.2B**. The dwell time distribution is approximated with a double-exponential decay function (lines in the corresponding colors) from which two mean dwell times for each conformation are extracted (dashed lines in the corresponding colors). c,d) Logarithmic cumulative dwell time distribution for closed state (a) and open state (b). The first (green) and the second (violet) dwell time are shown as linear lines with the values obtained from 'b'. The data points shown as black dots clearly deviate from a model with two decay channels. The third dwell time is extracted from the fitted linear function shown as black line. e,f) The square root of counts against logarithmic bins of the dwell time for closed state (c) and open state (d) shown as black dots. Each decay channel is described by the function $\sqrt{counts} = a \cdot exp\left[(t-\tau) - exp\left(t-\tau\right)\right]$. [117] The fitted functions for the first (green), second (violet) and third decay (black) and the sum of the functions (pink) are shown as lines. The data points above $exp\left(4\right)\ s \approx 55\ s$ for the open state and above $exp\left(2\right)\ s \approx 7\ s$ for the closed state are not represented by the functions for the first two dwell times, thus, the third fitted function is required. Hsp90 sketch adapted with permission from [60].

Table 6.2: **Comparison of dwell time extraction methods for ATP-conditions.**

	open			closed		
	τ_1 / s	τ_2 / s	τ_3 / s	τ_1 / s	τ_2 / s	τ_3 / s
Method 1	1.76	6.50	-	0.28	1.25	-
Method 2	-	-	32.4	-	-	2.62
Method 3	1.50	7.85	39.9	0.34	1.59	4.58

6.8 CONCLUSION

I have used plasmon rulers as a new approach to resolve protein conformational changes and to determine the time constants that govern the process. The obtained time constants are in good agreement with the previous obtained by FRET: the decay times are in the order of seconds and the open conformation is more frequent than the closed conformation. In addition, I discovered a new long lasting conformational state out of range to be resolved by FRET spectroscopy. This unexpected discovery of a third state with a transition time of about 150 s shows the power of the plasmon ruler method: Transitions from this state correspond to less than 1 % of the observed transitions, emphasizing the need of a large observation bandwidth. Also, the transition lifetime is well beyond what is commonly observed in single molecule fluorescence at room temperature. However, when the conformational changes of the protein are inhibited by AMP-PNP, the closed conformation is more frequent than the open one. This inhibition is described by decay times in the order of minutes not accessible by FRET. Thus, I show that plasmon rulers can resolve decay times that could not be determined before.

Our plasmon ruler preparation technique, while still somewhat inefficient, is easily adaptable to most proteins of interest. As a molecular chaperone, Hsp90 is a 'sticky' molecule, so I am optimistic that other molecules might proof easier to handle. I believe that the plasmon ruler method will be eventually able to observe single-molecule conformational dynamics from μs to days, which will provide a unique window to single molecule conformational dynamics. The ability to follow a single molecule for an extended period of time allows studying slow processes such as protein denaturing or the complex conformational changes after or during the interaction with other proteins or small molecules. More fundamentally, it will be possible to investigate the variability of protein conformational dynamics within nominally identical protein species, caused for example by small differences on the atomic level, variability in the amino-acid sequence or even the isotopic composition. Especially the possibility to study protein dynamics in different conditions is helpful to identify and characterize the function of potential drug targets in pharmaceutical research.

7 SUMMARY

The results presented in this thesis demonstrated the potential of plasmonic nanosphere dimers as real-time plasmon rulers in single-molecule studies due to their direct plasmon coupling. Here, I gave an overview about the accomplishments during my PhD, using plasmon rulers for applications such as DNA hairpin hybridization, polymer dynamics and protein dynamics.

First, I summarized the main challenges and constraints I faced during plasmon ruler assembly in **Chapter 3**. The linkage of only a single molecule can be achieved by a mixture of ligands for the nanoparticle functionalization. The assembly can be carried out as two fundamentally different approaches, as assembly in solution or as assembly on a surface. I tried both approaches but ultimately decided to perform the assembly on a surface. The reason for this was that the solution assembly required cleaning procedures that were tough to get to high enough efficiency and, due to the time and chemical steps needed, increased the likelihood of non-functioning proteins. During my work, it turned out that non-functioning dimers are the main issue in plasmon rulers connected by proteins, therefore I focused my assembly strategy to be as "gentle" and fast as possible - which made surface assembly the method of choice. For the assembly on a surface, the surface needed to be repellent to secondary nanoparticles. Main strategies included the unspecific binding of proteins blocking the surface or the covalent attachment of polymer chains to the surface. For polymer investigation, I blocked the surface with protein due to their fast reaction. For protein investigation, I attached a polymer to the surface because of higher efficiency.

In **Chapter 4**, I investigated the hybridization of a complementary DNA strand resulting in an opening of a DNA hairpin. The target strand was the gene sequence of the influenza virus subtype $H1N1$ and can, thus, act as a single molecule sensor for specific gene sequences.

Time-dependent measurement of the equilibrium extension fluctuations in a polymer, here polyethylene glycol, with plasmon rulers were shown in **Chapter 5**. With the extension fluctuations, I obtained the stiffness constant of the polymer under various salt concentrations. Whereas there was a stiffness transition with potassium ions at a concentration of above about 1.2 $mM\ K^{+}$, I did not observe a stiffness change with sodium ions. Therefore, the stiffness transition was specific to potassium and not to sodium.

I used plasmon rulers to show the conformational cycle of the molecular machine Hsp90, that fluctuates between an open and a closed conformation (**Chapter 6**). At the start of my work, a co-worker, Janak Prasad, had already succeeded in making Hsp90 connected dimers and measured a few timetraces. [53] However, the assembly process was slow and the efficiency was poor. Together with a setup that allowed only to measure one particle at a time, this caused insufficient statistics to get meaningful results on single protein dynamics. To overcome these problems, I tried several alternative strategies of dimer formation, both with regards to overall assembly strategy (in solution vs. on surface) as well as the linking chemistry. I tried to optimize these assembly processes using simple tethers, like PEG or DNA. In parallel, my co-workers, Sirin Celiksoy and Weixiang Ye, optimized the measurement process such that it became possible to measure hundreds of dimers in parallel - which greatly reduced the pressure to have efficient dimer assembly. These technical advances - together with the slightly improved assembly procedure - led to the successful observation of single protein dynamics with enough statistics that it is possible to perform tests like changing the dynamics with additives (AMP-PNP) and to discover previously hidden long-term dynamics. Together with my co-workers, we were able to measure the up to now longest single protein timetraces ever recorded (up to $24\,h$) - with the length of the measurement only limited by the patience of the observer and data storage considerations. Together with an exposure time as low as $10\,ms$, this gives an unprecedented observation bandwidth of 10^6 that will enable to look at rare transitions in proteins. The simultaneous recording of hundreds of single molecules in parallel makes investigations into effects of protein heterogeneity on its conformational dynamics possible.

8 APPENDIX

8.1 MICROSCOPE SETUP MODIFICATIONS

For our setup[**], we equipped an inverted microscope Zeiss Axio Observer Z1 with a PI721 Z-Piezo (Physik Instrumente, 100 μm travel range), and a Plan--Apochromat $40x$ / 1.3 Zeiss objective. The light source used is a SuperK EXTREME supercontinuum laser with a SuperK SELECT multi-line tunable filter (NKT Photonics) controlled with a ADwin-Gold II (Jäger Messtechnik). A home-made MATLAB-based software was used for automated data acquisition and analysis. With our setup configuration the simultaneous investigation of the complete field of view ($1000 - 2000$ nanoparticles) with high temporal resolution was possible. The average exposure time for each wavelength was about 50 ms exposure time plus about 10 μs to switch between the wavelengths. In sum, we needed about 1 s for acquiring a stack of images for the extraction of the spectra of all the nanoparticles in the field of view, and about 100 ms between time-steps of the timetrace in the double-line configuration. For single-line configuration, we can either illuminate constantly with just one wavelength filtered by the AOTF or use a LED as light source [††].

[**] The setup was developed by Weixiang Ye. It was used in double-line configuration in the manuscript accepted as [51] and in single-line configuration in the manuscript in preparation as [109].

[††] A setup with LED as light source was developed by Sirin Celiksoy and also used in the manuscript in preparation as [109].

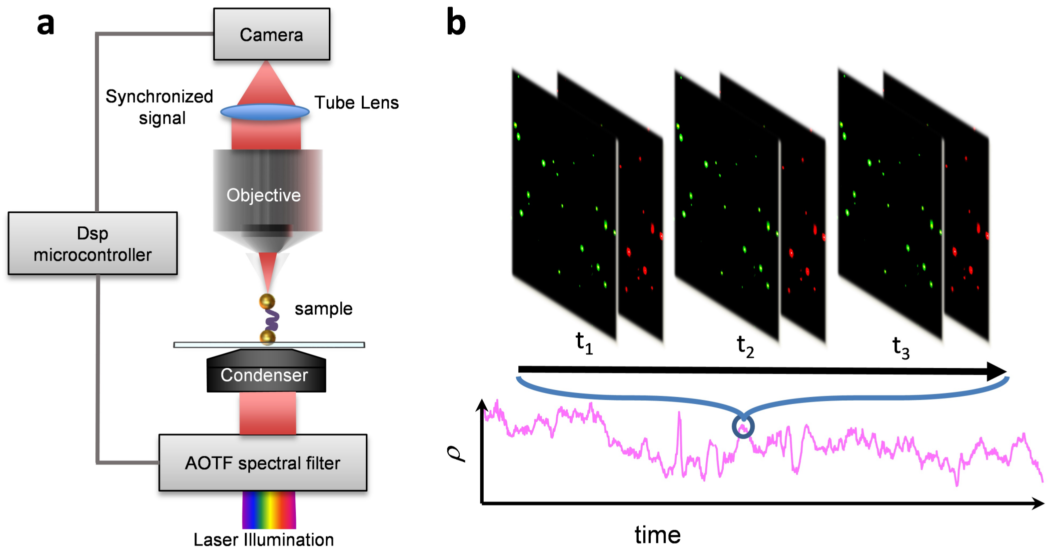

Figure 8.1: **Microscope Setup.** a.) Schematic representation of the dual-line imaging setup used in this work. b.) Two images at two different wavelengths were acquired at each time-step t_1, t_2, t_3, ... (top). From each pair of images, we extracted the parameter ρ, which then forms a time-trace $\rho\,(t)$ (bottom). Figure included in the manuscript accepted as [51].

8.2 DNA-HAIRPINS OPEN BY COMPLEMENTARY DNA

If not specified, all the chemicals and reagents were purchased with analytical grade from Sigma-Aldrich or Merck. Deionized water from a Millipore system ($> 18\ M\Omega$, Milli Q) was used in all experiments.

8.2.1 NANOPARTICLE FUNCTIONALIZATION

- DNA-Biotin coated gold nanospheres (AuNP@DNA-Biotin): DNA was purchased from Biomers GmbH. The DNA-sequence for the Biotin-DNA-SH was CCC TTT AAC CCC TTC TTC ATC GAG AGT GTA GTC GGG GGT TTT TTT dissolved in TE-Buffer to a final concentration of 200 μM. The nanoparticle functionalization was carried out modified from a published procedure. [118] I mixed 500 μL of AuNPs (60 nm, BBI) with a DNA-mixture consisting of 10 μL 100 μM short DNA-SH (T_{10}) and 0.5 μL 200 μM Biotin-DNA-SH. After 30 min of incubation, I added 10 μL Sodium-Citrate-Buffer (500 mM, $pH = 3.0$) and incubated overnight at room temperature. The particle were washed three times with TE-Buffer by centrifugation (7000 g, 5 min).

- Streptavidin coated gold nanospheres (AuNP@Streptavidin): 500 μL of AuNPs (60 nm, BBI) were centrifuged (7000 g, 5 min) and the supernatant removed. I prepared a solution containing 50 μL of 1 mg/mL streptavidin and 50 μL of 0.3 mM DTSSP (3,3´- Dithiobis(sulfosuccinimidylpropionate)) in phosphate saline buffer (PBS). After 30 min of incubation, I desalted the solution in a desalting column and added to the AuNPs pellet. This solution was mixed incubated overnight at 4 °C. To remove the excess of streptavidin, I washed the AuNPs twice with 400 μL of Milli-Q water (by centrifugation as described above) and stored at 4 °C until use.

8.2.2 DIMER FORMATION

I assembled a microfluidic flow cell from glass slides that were pegylated and biotinylated as described. [119] I immobilized the diluted AuNP@Streptavidin (in TE-Buffer) in the flow cell and incubated with the AuNP@DNA-Biotin (in TE-Buffer) for 1 *h*. The extra nanoparticles were removed with TE-Buffer.

8.2.3 MEASUREMENT CONDITIONS

The spectral position of the dimers in TE-Buffer was recorded in a dark-field microscope. [27] Next, a solution containing 100 μM of target-DNA in TE-Buffer was flushed for 5 *min* and the spectral position was recorded again.

8.3 POTASSIUM TRIGGERS A REVERSIBLE SPECIFIC STIFFNESS TRANSITION OF POLYETHYLENE GLYCOL

If not specified, all the chemicals and reagents were purchased with analytical grade from Sigma-Aldrich or Merck. Deionized water from a Millipore system ($> 18\ M\Omega$, Milli Q) was used in all experiments.

8.3.1 NANOPARTICLE SYNTHESIS AND CHARACTERIZATION

We performed the gold nanoparticle (AuNP) preparation as described in reference [100] with minor modifications. The process has four steps: first seeds are prepared, then grown to a size of 10 nm, then further grown to a larger size, and finally etched down to the desired size. Gold seeds: We added 50 μL of a 0.05 M $HAuCl_4$ solution to 5 mL of a 0.1 M $CTAC$ solution, then injected 200 μL of a freshly prepared 0.02 M $NaBH_4$ solution under vigorous stirring. After 5 min, we diluted the mixture 10 times with 100 mM $CTAC$. To grow AuNPs with 10 nm diameter, we added 900 μL of the gold seeds (prepared as described above) and 40 μL of 0.1 M ascorbic acid to 10 mL of 25 mM $CTAC$ solution. Then, we injected 50 μL of 0.05 M $HAuCl_4$ under vigorous stirring. AuNP growth: We mixed 200 μL of 10 nm AuNPs and 400 μL of 0.1 M ascorbic acid with 100 mL of a 25 mM $CTAC$ solution. Then, we added 50 μL of a 0.05 M $HAuCl_4$ solution under stirring. This growth solution was left undisturbed for 1 h. Oxidative etching: We used oxidative etching to smooth the nanoparticle surface, make them more spherical and decrease the degree of polydispersity. [100] We injected 100 μL of a dilute $NaClO$ solution (1.5 wt% of available chlorine) under stirring and then left undisturbed for 30 min. The 10 nm AuNP were grown into the final nanospheres as described in reference [100] using the growth and etching solutions described above.

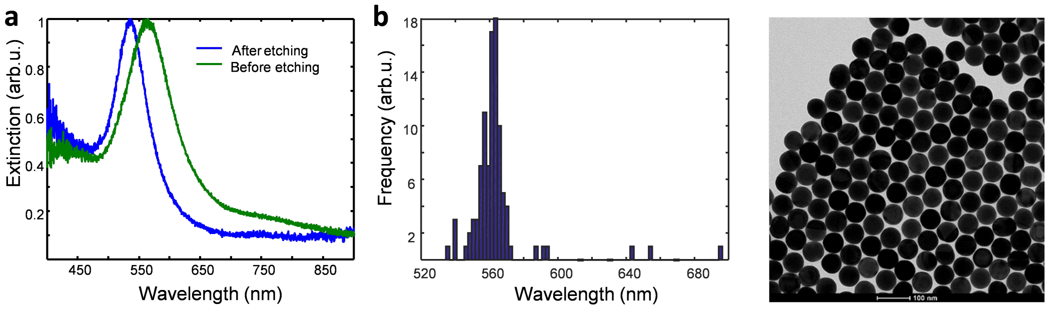

Figure 8.2: **Nanoparticle Synthesis.** a.) Extinction spectrum measured in a conventional optical spectrometer for UV, VIS and NIR wavelength before and after the etching process. The final nanospheres showed a plasmon wavelength centered at 532 nm. b.) Distribution of the plasmon resonance wavelengths of single particles immobilized on a flowcell surface (in water). The distribution (of around 1000 nanoparticles) shows a Gaussian distribution around maximum at $\lambda_{max} = 561\ nm$ with a scattering of about $\pm 9\ nm$ around this value (standard deviation). c.) Transmission electron microscopy image of the gold nanoparticles used in this work. These nanoparticles have a mean diameter of $52\ nm \pm 2\ nm$ (standard deviation). Figure included in the manuscript accepted as [51].

8.3.2 NANOPARTICLE FUNCTIONALIZATION

- PEG-Biotin coated gold nanospheres (AuNP@PEG-Biotin): I centrifuged 500 μL AuNPs (7000 g, 5 min), removed the supernatant and resuspended the pellet in 100 μL freshly prepared 2 mM PEG solution (mix of Thiol-PEG-Biotin with 3317 Da and Thiol-PEG-OMe with 1981 Da (5 : 95 molar ratio), Iris Biotech GmbH). I incubated the mixture for 2 h at room temperature under stirring. I repeated the process and incubated overnight at 4 °C. To remove excess of Thiol-PEG-Biotin, I washed the AuNP@PEG--Biotin twice with 400 μL of Milli-Q water (by centrifugation and resuspension as described above) and stored the particles at 4 °C until use.

- Streptavidin coated gold nanospheres (AuNP@Streptavidin): 500 μL of AuNPs were centrifuged (7000 g, 5 min) and the supernatant removed. I prepared a solution containing 50 μL of 1 mg/mL streptavidin and 50 μL

of 0.3 *mM* DTSSP (3,3´- Dithiobis(sulfosuccinimidylpropionate)) in phosphate saline buffer (PBS). After 30 *min* of incubation, I desalted the solution in a desalting column and added to the AuNPs pellet. This solution was mixed incubated overnight at 4°*C*. To remove the excess of streptavidin, I washed the AuNPs twice with 400 *µL* of Milli-Q water (by centrifugation as described above) and stored at 4 °C until use.

8.3.3 DIMER FORMATION

The microfluidic flow cell was first washed with 'Hellmanex II special cleaning concentrate' and then rinsed with 1 *mL* of Milli-Q water.

I flushed AuNP@PEG-Biotin through the flow cell for 3–4 *min*. For their immobilization on the flow cell surface, I used a 1 *M NaCl* solution. Then, I passivated the glass-surface for 10 *min* with a mixture of 'superblock' (Pierce) and conjugation buffer (2.5 *mM* Tris-HCl pH 7.5, 0.25 *mM* EDTA, 0.5 *M NaCl*, 0.025 % Tween 20) in a 60 : 40 ratio. After the passivation, I injected a solution containing AuNP@Streptavidin in a 60 : 40 mixture of superblock and conjugation buffer into the flow cell and incubated for 10 *min*. I removed unbound particles by rinsing 10 *min*with a 60 : 40 mixture of superblock and conjugation buffer.

8.3.4 DIMER SKETCH

We use the curvature of the nanoparticles, the approximated diameter of streptavidin (5 *nm*) and PEG (12 *nm*) [50] to rationalize that the chance of finding a particle dimer connected by two PEG molecules is very low. A sketch of the particle gap is shown in Appendix **Figure 8.3** with the molecules shown to scale. The sketch shows that steric hindrance is the main factor preventing multiple linkers - in accordance to previous experiments with bi-functional PEG mixtures in our group. [101]

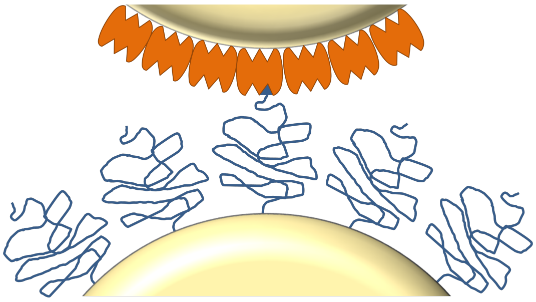

Figure 8.3: **Sketch of a particle dimer linked with a single PEG molecule** (approximately to scale). The streptavidin molecule is shown in orange, the PEG molecule in blue. Figure included in the manuscript accepted as [51].

8.3.5 MATLAB SCRIPT FOR SPRING CONSTANT EVALUATION

The evaluation of spring constants as shown in **Figure 5.2** and **Figure 5.3** was carried out with a MATLAB script (see Appendix **Figure 8.4**).

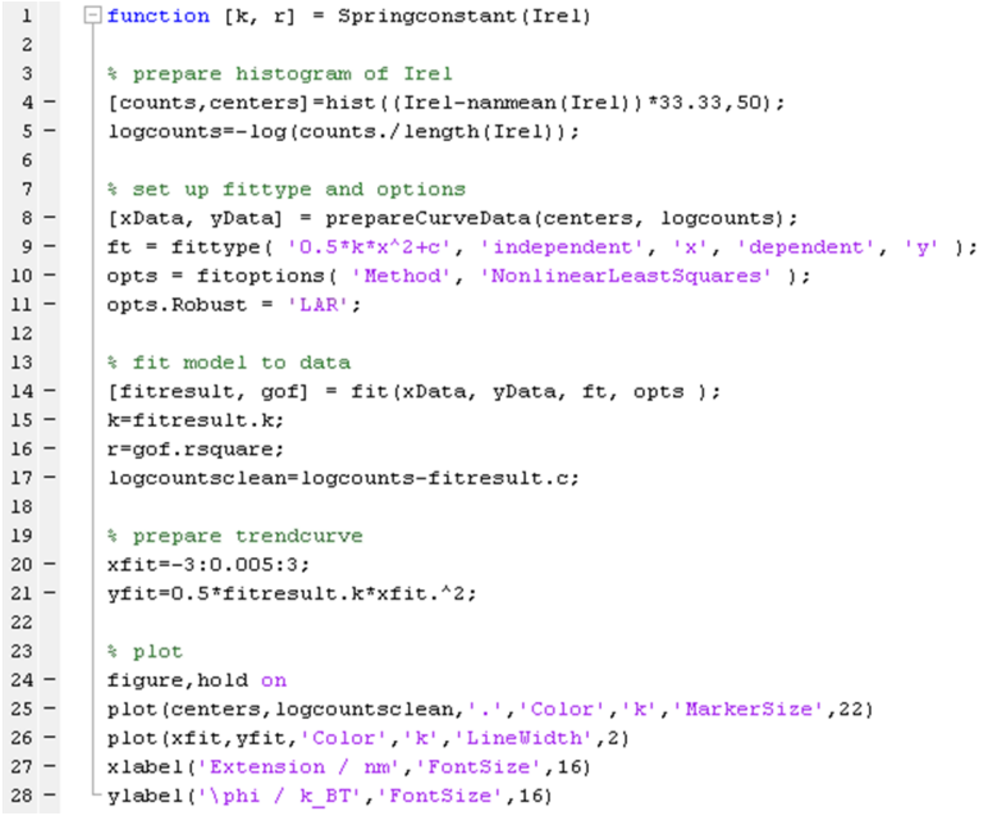

```
function [k, r] = Springconstant(Irel)

% prepare histogram of Irel
[counts,centers]=hist((Irel-nanmean(Irel))*33.33,50);
logcounts=-log(counts./length(Irel));

% set up fittype and options
[xData, yData] = prepareCurveData(centers, logcounts);
ft = fittype( '0.5*k*x^2+c', 'independent', 'x', 'dependent', 'y' );
opts = fitoptions( 'Method', 'NonlinearLeastSquares' );
opts.Robust = 'LAR';

% fit model to data
[fitresult, gof] = fit(xData, yData, ft, opts );
k=fitresult.k;
r=gof.rsquare;
logcountsclean=logcounts-fitresult.c;

% prepare trendcurve
xfit=-3:0.005:3;
yfit=0.5*fitresult.k*xfit.^2;

% plot
figure,hold on
plot(centers,logcountsclean,'.','Color','k','MarkerSize',22)
plot(xfit,yfit,'Color','k','LineWidth',2)
xlabel('Extension / nm','FontSize',16)
ylabel('\phi / k_BT','FontSize',16)
```

Figure 8.4: **MATLAB script for spring constant evaluation.** Input parameter is a vector containing the relative Intensity I_{rel} and output is the spring constant k and the coefficient of determination (goodness of fit) r.

8.3.6 SINGLE MOLECULE DIMER

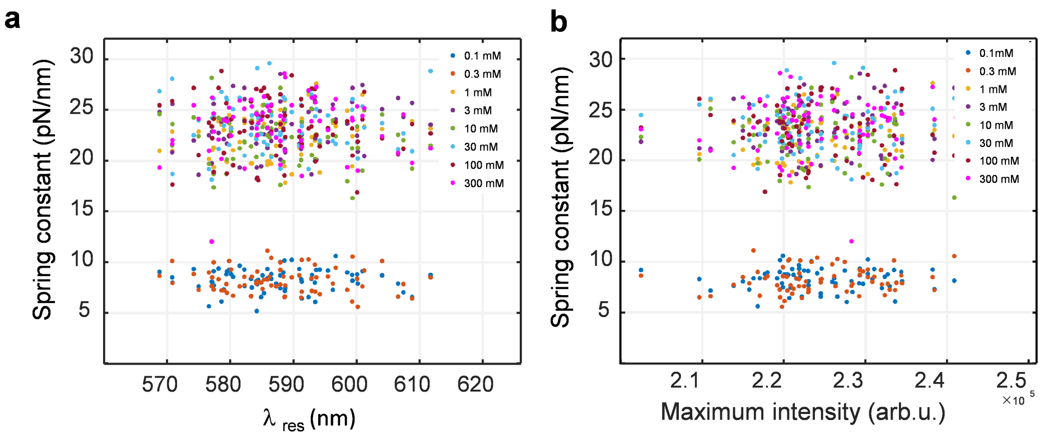

Figure 8.5: **Controls regarding particle size effects.** a.) Spring constants obtained as function of the resonance wavelength of the nanoparticle dimer λ_{res}. b.) Spring constants as function the maximum intensity of the nanoparticle dimer. In both cases (a, b), the contracted and expanded state are clearly distinguishable. Since resonance wavelength and maximum intensity are both functions of the nanoparticle size, the absence of any trend in 'a' and 'b' shows that the particles themselves do not influence the spring dynamics of the equilibrium fluctuations. Figure included in the manuscript accepted as [51].

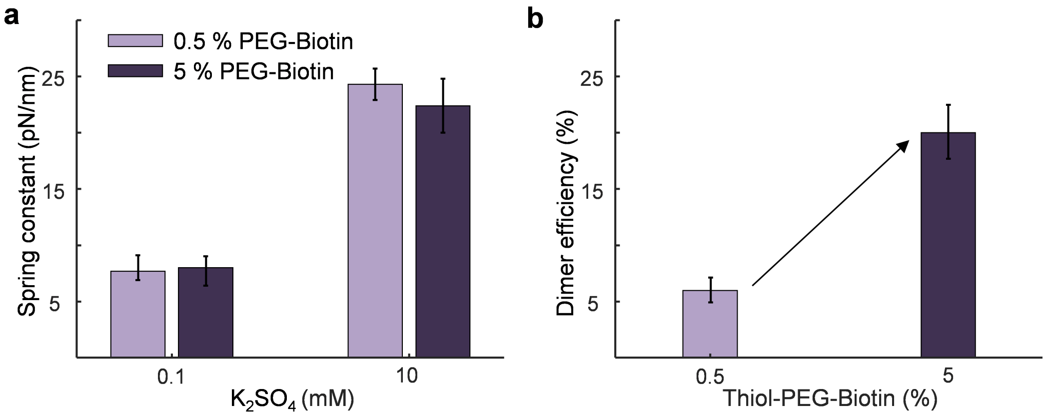

Figure 8.6: **Control regarding the possible formation of double linkers.** a.) Spring constant values obtained with plasmon rulers containing 0.5 % PEG-Biotin and 5 % PEG-Biotin for 0.1 mM and 10 mM K_2SO_4 yield the same values. b.) Dimer efficiency for 5 % PEG-Biotin is three times higher than for 0.5 % PEG-Biotin. Both results together indicate that there is indeed one linker. If there were multiple linkers, the graph in 'a' should show different values and the graph in 'b' should show more or less equal efficiencies. Figure included in the manuscript accepted as [51].

8.3.7 CONTROL AND REAL DIMERS

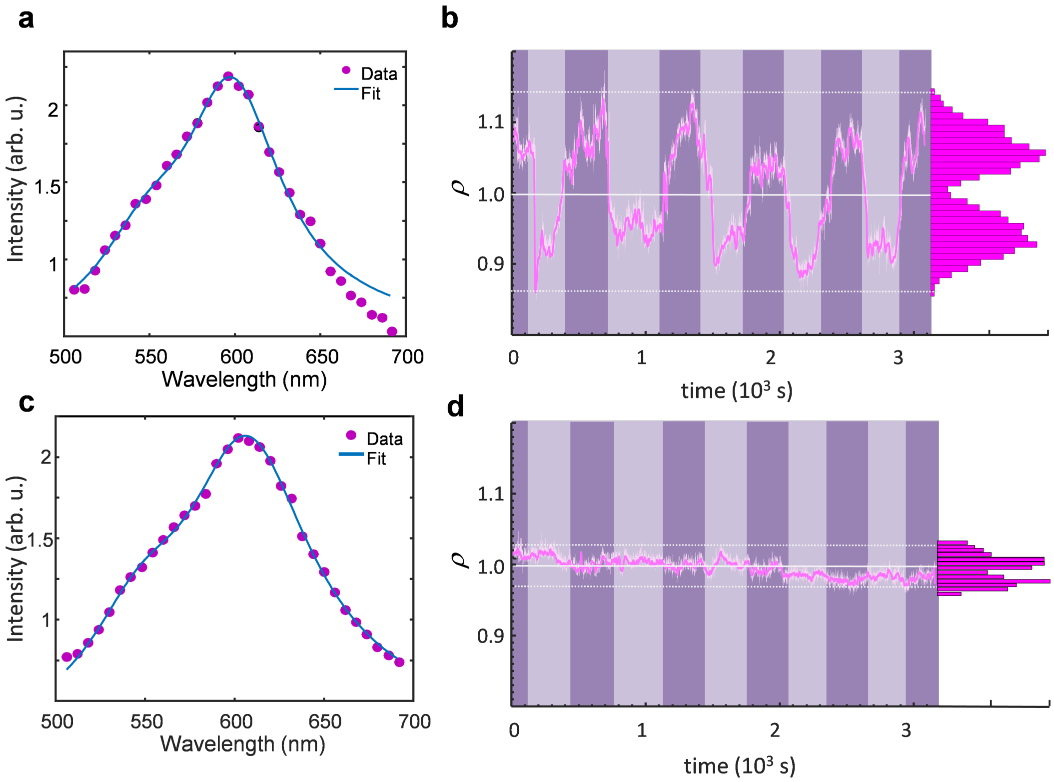

Figure 8.7: **Control and real dimers.** a and c: Two representative spectra of two different nanoparticle plasmon rulers. Dots represent the measured data, the blue line shows the best fit to a double Lorentzian. b and d: Timetraces corresponding to the plasmon rulers shown in 'a' and 'c', respectively. The clear/dark regions correspond to an environment with 0.1 mM / 10 mM K_2SO_4, respectively. On the right side of the panels, the histogram shows the total time spend in each configuration. In 'b', the PEG molecule shrinks at higher salt concentrations and expands again at lower salt concentration. This process is fully reversible for more than 10 changes. d.) The timetrace of this dimer does not react on salt concentration changes, most likely because the second particle attaches to the surface as well. I refer to such dimers as 'control dimer' because it is useful to estimate our setup noise. Figure included in the manuscript accepted as [51].

8.3.8 INTRINSIC VISCOSITY MEASUREMENTS

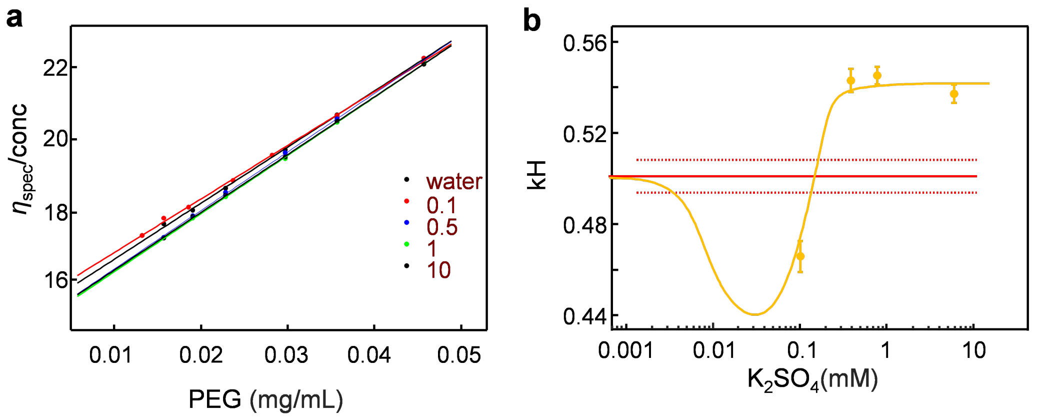

Figure 8.8: **Intrinsic viscosity measurements.** a.) Huggins plot representing the specific viscosity as function of the PEG concentration at the K_2SO_4 concentrations indicated in the inset (mM). From this plot we obtained the specific intrinsic viscosity values which are plotted in the **Figure 5.3C** of **Section 5**. b.) Huggins constant 'kH' as function of the salt concentration. Thermodynamically, the situation described here (and in **Figure 5.3C** of **Section 5**) correspond to a 'deterioration' of the water quality (as solvent) by the presence of K_2SO_4. This situation is revealed by the dependence of the Huggins constant on the salt concentration: As the solvent power gets worse, kH increases because polymer segments are progressively forced to move conjointly ('pull along effect'). [120] Figure included in the manuscript accepted as [51].

8.3.9 MOLECULAR DYNAMICS SIMULATIONS

The program NAMD9 and the charmm27 force field [121, 122] with the extension for PEG [123] was employed in our simulations. ‡‡ We modeled water with the help of Tip3p. [124] Across the simulations, each of the integration time steps was 1 fs long. Periodic boundary conditions were set for our simulations. We carried out the simulations using periodic boundary conditions. We provided constant pressure and temperature at 1 atm and 300 K, respectively, during the simulations using the Langevin piston algorithm and Langevin thermostat. [125, 126] For the non-bonded interactions, we employed a cutoff of

---

[‡‡] The simulations were conducted by Dr. Giovanni Settanni and Prof. Friederike Schmid (Institute of Physics, University of Mainz) and are presented in the manuscript accepted as [51].

1.2 nm with a switch function. Long ranging electrostatic interactions could be approximated with the smooth particle mesh Ewald (PME) [127] method with a grid spacing of about 0.1 nm. The cubic box was 7.2 nm long containing water molecules and a PEG molecule ($H - [O - CH_2 - CH_2]_n - OH$, with n either 18 or 36). The respective PEG molecules were placed in three different systems: one with no ions, one including 0.15 M $NaCl$ and one including 0.15 M KCl. Employing the steepest descent algorithm, we could minimize the complete systems individually for 10000 steps. After equilibrating the systems at room temperature and pressure for 1.0 ns, we carried out replica exchange molecular dynamics with solute tempering (REST2). [128, 129] Each replica ran for 100 ns with a total of 10 replicas where the temperature of PEG (the solute), varied between 300 and 650 K with replica swap attempts every 1 ps. We analyzed the replica with the lowest temperature. In this way, we ensured an efficient sampling of the conformational space of PEG. The convergence criterion was reached with our determined replica swap acceptance rates of 25 to 50 % for PEG18 and around 20 % for PEG36, resulting in a uniform distribution of the 10 walkers over the 10 temperatures. The analysis was carried out with the help of the programs VMD and WORDOM. [130, 131] With these programs, we were able to extract the radius of gyration, the radial distribution function of the oxygen atoms of PEG and the ions, the persistence length and the number of contacts between ions an PEG.

Table 8.1: **Average radius of gyration (in nm) of PEG 18 and PEG 36 obtained by molecular dynamics simulations in water, 150 mM K^+ and 150 mM Na^+.**

	H_2O	$c(Na^+) = 0.15\ M$	$c(K^+) = 0.15\ M$
$r(PEG18)\ /\ nm$	8.72 ± 0.02	8.77 ± 0.03	8.52 ± 0.03
$r(PEG36)\ /\ nm$	12.84 ± 0.08	12.53 ± 0.10	12.34 ± 0.15

8.4 HSP90'S CONFORMATIONAL CYCLE HAS THREE DECAY CHANNELS

If not specified, all the chemicals and reagents were purchased with analytical grade from Sigma-Aldrich or Merck. Deionized water from a Millipore system ($> 18\ M\Omega$, Milli Q) was used in all experiments.

8.4.1 NANOPARTICLE FUNCTIONALIZATION

- AuNP@PEG-Biotin. 500 μL AuNPs (60 nm, BBI) were centrifuged (7000 g, 5 min), the supernatant removed and the pellet resuspended in 100 μL freshly prepared 2 mM PEG mixture (Thiol-PEG-OMe 2 kDa, Thiol-PEG-Biotin 3 kDa, Thiol-PEG-NH_2 3 kDa in a ratio of $87 : 10 : 3$, Iris Biotech GmbH) solution and incubated for 2 h at room temperature. To remove the excess of Thiol-PEG, I washed the AuNP@PEG-Biotin twice with 400 μL of Milli-Q water and stored at 4 °C until use.

- AuNP@PEG-NH_2.500 μL AuNPs (60 nm, BBI) were centrifuged (7000 g, 5 min), the supernatant removed and the pellet resuspended in 100 μL freshly prepared 2 mM PEG mixture (Thiol-PEG-OMe 2 kDa, Thiol-PEG-NH_2 3 kDa in a ratio of $97 : 3$, Iris Biotech GmbH) solution and incubated for 2 h at room temperature. To remove the excess of Thiol-PEG, I washed the AuNP@PEG-NH_2 twice with 500 μL of Milli-Q water and stored at 4 °C until use.

8.4.2 DIMER FORMATION

For assembling our microfluidic flow cell I used glass slides that were pegylated and biotinylated as described. [80] I flushed the flow cell with streptavidin solution (250 $\mu g/mL$ in PBS) for 15 $,min$ and rinsed with PBS.

I immobilized a diluted AuNP@PEG-Biotin solution (in PBS) and rinse with PBS. The immobilized particles were reacted with 1 mM SMCC (succinimidyl 4-(N-maleimidomethyl)cyclohexane-1-carboxylate) in PBS $pH = 7.4$ for 30 min and rinsed with PBS $pH = 6.7$. Next, a solution containing 0.24 nM Hsp90 and 200 nM TCEP (tris-(2-carboxyethyl)-phosphin) in PBS $pH = 6.7$ was incubated in the flow cell and the immobilized particles were rinsed again with PBS $pH = 6.7$. Meanwhile, AuNP@PEG-NH$_2$ has been incubated for 20 min with 1 mM SMCC, and washed four times with water by centrifugation. After the last round of centrifugation, the pellet was resuspended in PBS $pH = 6.7$ and introduced into the flow cell for 30 min. Unbound particles were removed by HEPES (4-(2-hydroxyethyl)-1-piperazineethanesulfonic acid) buffer (40 mM HEPES, 50 mM KCl, 50 mM $MgCl_2$, $pH = 7.4$).

8.4.3 MEASUREMENT CONDITIONS

First the thermal fluctuations of HSP90 in the apo-state were investigated by recording a timetrace in HEPES buffer. Next, 2 mM AMP-PNP (β,γ-imido-adenosine 5´-triphosphate) in HEPES buffer was flown for 10 min and another timetrace of this configuration was recorded. Timetraces under ATP-conditions were recorded in the presence of 5 mM ATP (adenosine triphosphate) in HEPES buffer.

8.4.4 UNSPECIFIC BINDING OF HSP90 TO DNA-LINKERS

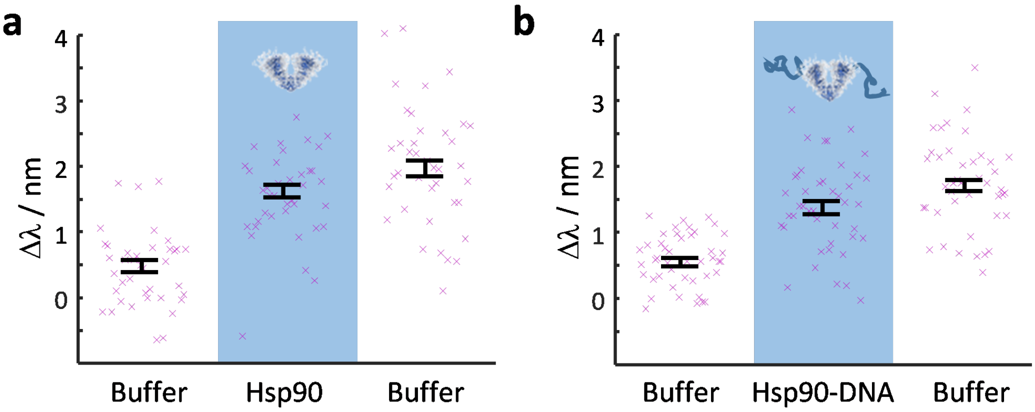

Figure 8.9: **Unspecific binding of Hsp90 to DNA.** Shift in resonance wavelength for individual nanoparticles (each cross) functionalized with DNA incubated with Hsp90 (a) or Hsp90 coupled to complementary DNA (b). Hsp90 can not be washed off indicating unspecific binding.

8.4.5 SETUP PERFORMANCE

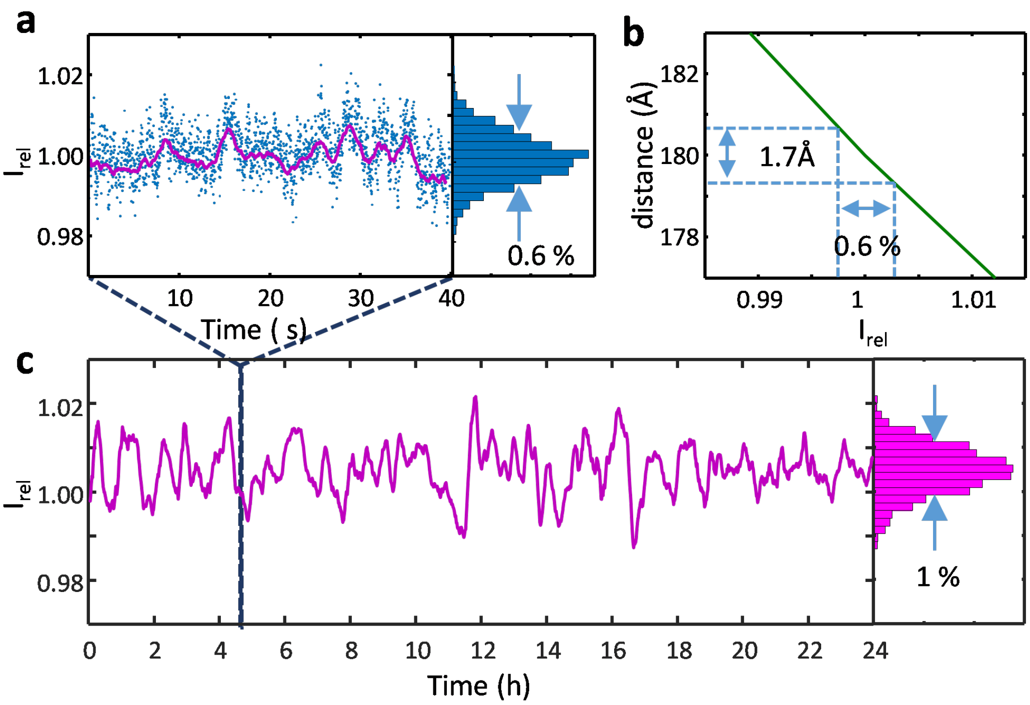

Figure 8.10: **Setup performance.** a) Short piece of a time-trace recorded at 20 *ms* of a non-fluctuating dimer (blue dots). The intensity varies around 0.59 % around its mean value. b) This intensity variation translates to an error in the interparticle distance of about 1.7 *Å* (assuming pure setup noise) Reducing the time resolution to 1.2 *s* (pink line in a) reduces the intensity variations to 0.33 %, enough to record 1 *Å* conformational changes in the linker. c) Typical example of a long timetrace (24 *h*), again for a non-fluctuating dimer. The pink line shows that the intensity variations on a 10 *min* (average 30000 data point) timescale is about 1 %, which implies that slow conformational changes need to be larger than 3.2 *Å* to be resolved.

Our realization of the plasmon ruler technique (setup development by Sirin Celiksoy and Weixiang Ye), even if many orders of magnitude improved from previous work, has not yet reached the maximum possible observation bandwidth. There should be no fundamental limit for the total observation time except for the lifetime of the molecule under investigation and the patience of the observer. On the other extreme, the speed of data acquisition is fundamentally limited for two different reasons (besides technical limitations due to readout and data transfer speed): One limit is that conformational dynamics faster than the diffusion time of the sphere cannot be measured. In our case, this time resolution would be0.1 μs (calculated for a distance change Δx of 1 nm and a spheres of 60 nm diameter). The other limit is the heating associated with the increase of illumination power necessary to yield an equivalent signal to noise ratio as in our measurements. I calculate the temperature increase ΔT for a sphere with a radius of $r = 30\,nm$ and an absorption cross section of $c_{abs} = 1.5 \centerdot 10^{-14} m^2$ immersed in water with a thermal conductivity $\kappa = 0.591 W m^{-1} K^{-1}$ with our laser intensity $I = 1.1 \centerdot 10^4 W m^{-2}$ with the following formula: [114]

$$\Delta T = c_{abs} \cdot I / 4 \pi \kappa r \tag{8.1}$$

If I tolerate a temperature increase of 1 K, I could reduce the time to about 7 μs. Technical improvements like a more efficient light collection, detectors with higher quantum yield, or lower read-out noise could reduce this time further. Both calculations indicate that with sufficiently fast detectors, protein conformational dynamics should be possible to observe with μs time resolution.

8.4.6 ADDITIONAL HSP90 TIMETRACES MONITORED FOR 24 HOURS

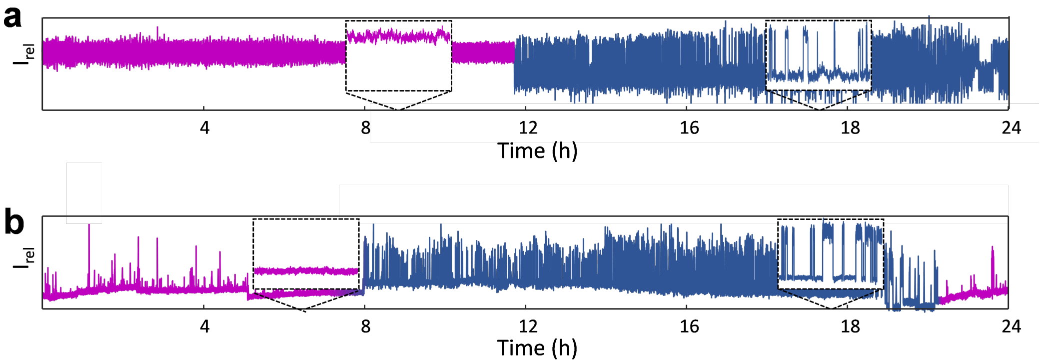

Figure 8.11: **Additional Hsp90 Timetraces Monitored for 24 Hours.** a) Exemplary 24 *h* timetrace with a long dwell (12 *h*) of Hsp90 in its closed conformation with a zoom-in of both parts of the timetrace: locked conformation (pink) and fluctuations (blue). b) Exemplary 24 *h* timetrace with a long dwell (6 *h*) of Hsp90 in its open conformation with a zoom-in of both parts of the timetrace: locked conformation (pink) and fluctuations (blue).

8.4.7 MEASUREMENT CONTROL

It has been assumed, that Hsp90 inhibited with the slowly hydrolyzable AMP-PNP is locked in the closed conformation. Since I can now record longer dwell times (above FRET-cutoff) with plasmon rulers, it is possible to characterize this inhibition with decay times. In Appendix **Figure 8.12B** and Appendix **Table 8.2**, I show how far the equilibrium is shifted by AMP-PNP: The second decay time of the closed state in the locked-configuration is 30 times bigger than it would be in apo-condition. The inhibition with AMP-PNP increases the energy barrier by $3k_BT$ (calculated by $\Delta G^* = k_BT \cdot \ln(A \cdot \tau)$, where A is approximated to $A \approx 10^8 s^{-1}$). [132]

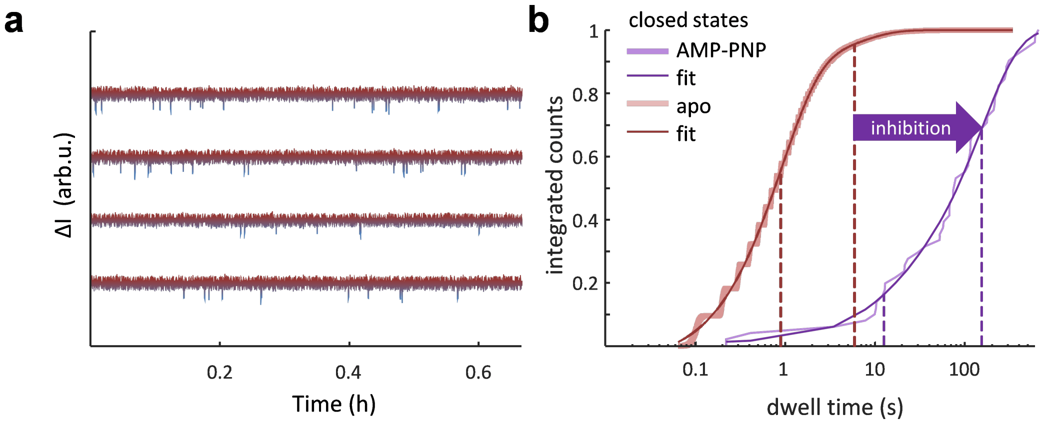

Figure 8.12: **Inhibition of Hsp90 with AMP-PNP.** a) Timetraces of the same dimers as in **Figure 6.4** that have been incubated with AMP-PNP (known to inhibit transitions) monitored for 40 min with 10 fps. b) Cumulative dwell time distribution for the closed state under apo-conditions (red) and inhibited conditions (violet). Dwell times are extracted as shown in **Figure 6.2B**. The dwell time distribution is approximated with a double-exponential decay function (lines in the corresponding colors) from which two mean dwell times for each conformation are extracted (dashed lines in the corresponding colors). The inhibition caused a prolonged stay in the closed conformation.

Table 8.2: **Decay times of Hsp90 obtained by plasmon rulers compared to FRET.**

		open		closed	
		FRET	PR	FRET	PR
apo	τ_1 / s	1.45 ± 0.04	1.45 ± 0.01	0.85 ± 0.03	0.90 ± 0.01
	τ_2 / s	10.4 ± 0.6	15.0 ± 0.1	8.2 ± 0.2	5.9 ± 0.3
AMP-PNP	τ_1 / s	-	0.9 ± 0.7	-	12 ± 8
	τ_2 / s	-	2 ± 3	-	153 ± 11
ATP	τ_1 / s	0.79 ± 0.05	1.76 ± 0.02	1.54 ± 0.04	0.28 ± 0.01
	τ_2 / s	5.46 ± 0.15	6.50 ± 0.08	20.6 ± 10.5	1.25 ± 0.02

8.4.8 DWELL TIMES ARE STATISTICALLY DISTRIBUTED

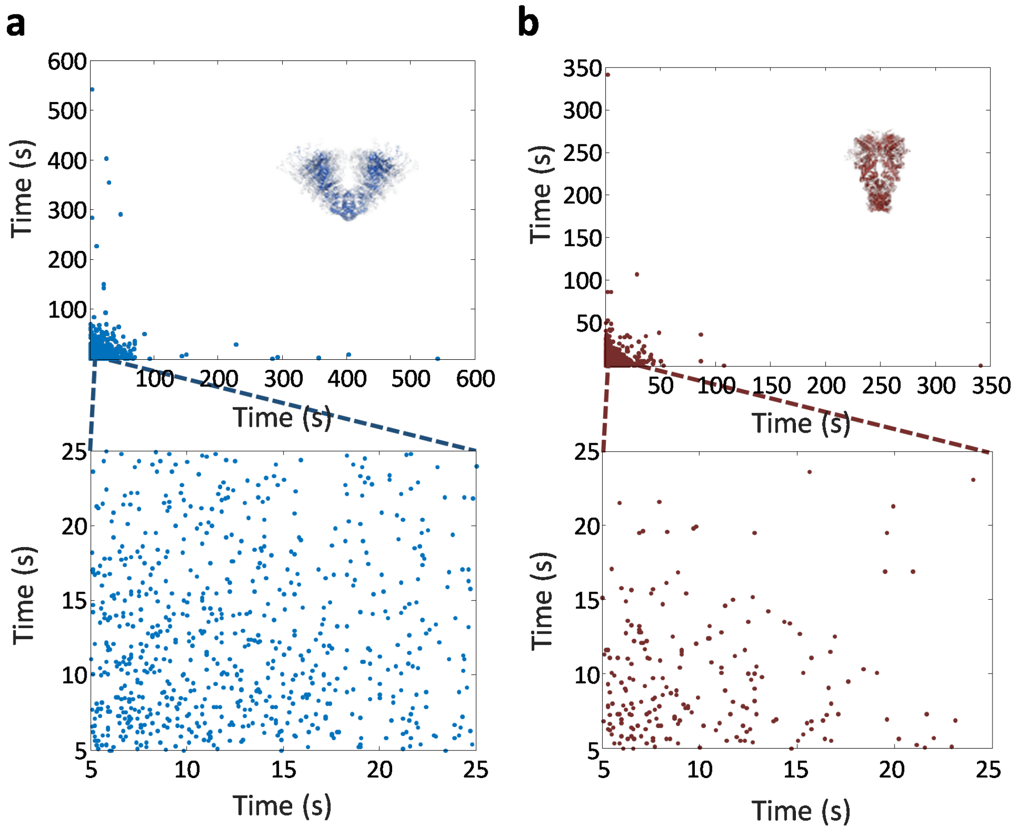

Figure 8.13: **Statistical distribution of the dwell times.** Each dwell time is represented against its successive value showing random distribution for the open (a) and closed (b) conformation.

8.4.9 HETEROGENEITY WITHIN HSP90 POPULATION

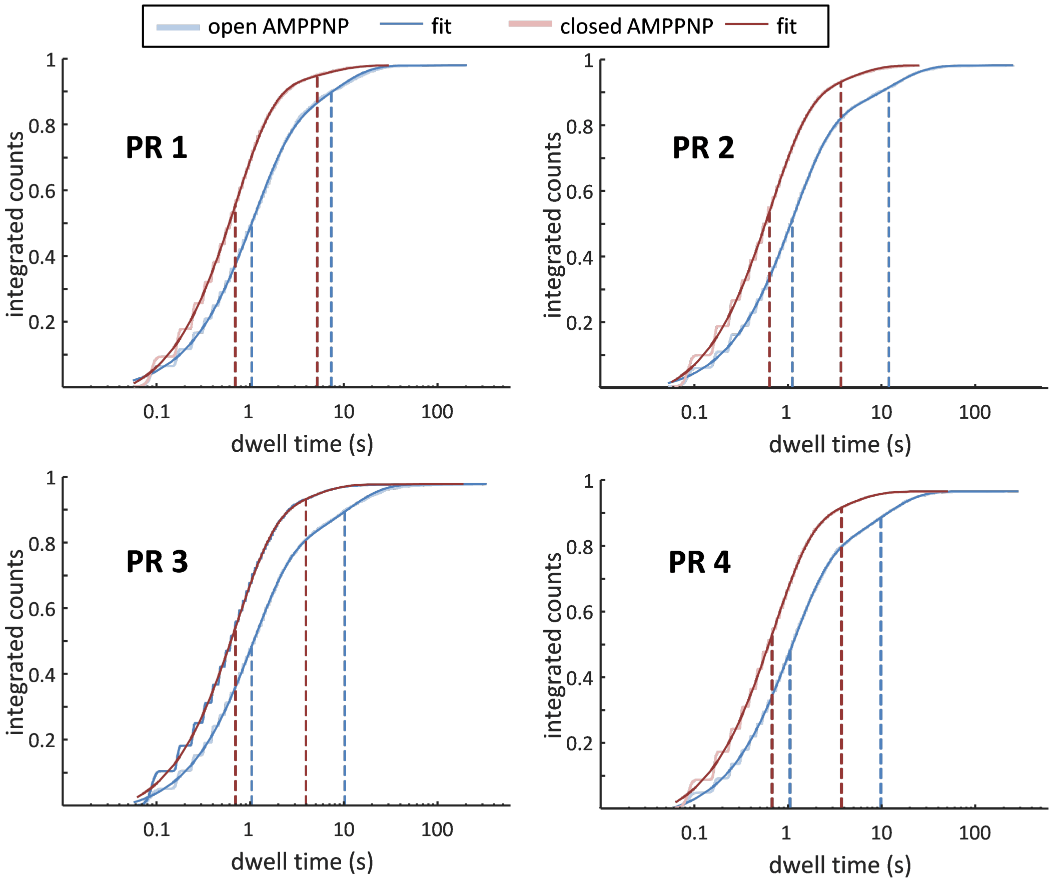

Figure 8.14: **Thermal dwell times of Hsp90 for individual plasmon rulers.** Cumulative dwell time distribution for open state (blue) and closed state (red) for individual plasmon rulers (mean of the four plasmon rulers shown in **Figure 6.5B**). The dwell time distribution is approximated with a double-exponential decay function (lines in the corresponding colors) from which two mean dwell times for each conformation are extracted (dashed lines in the corresponding colors).

Table 8.3: **Decay times of Hsp90 obtained by individual plasmon rulers.**

	open		closed	
	τ_1 / s	τ_2 / s	τ_1 / s	τ_2 / s
PR 1	1.40	11.1	0.91	7.66
PR 2	1.53	18.8	0.84	5.38
PR 3	1.39	15.7	0.92	5.34
PR 4	1.43	15.2	0.90	5.43
all	1.45	15.0	0.90	5.90

8.4.10 Simulated Dwell Time Distribution

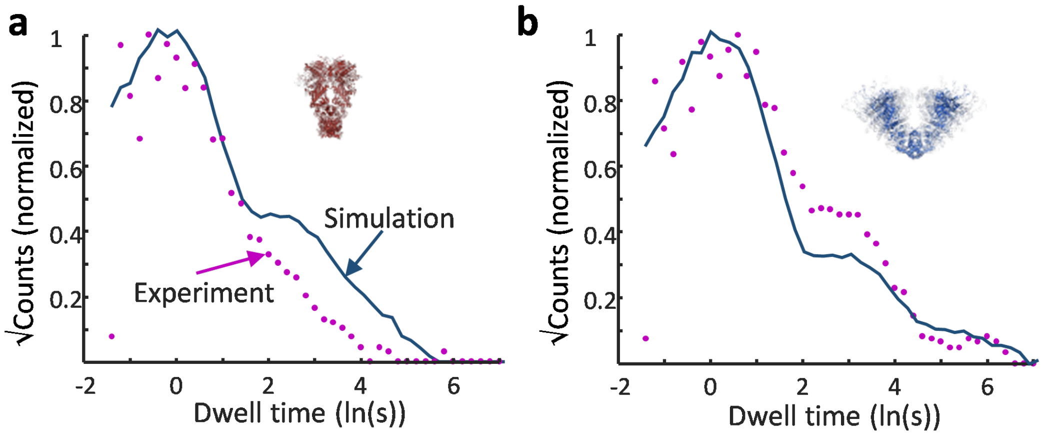

Figure 8.15: **Comparison of experimental and simulated dwell time distribution.** The experimental dwell time distribution is shown as pink dots and the dwell times from a 7-day simulation is shown as blue line for the closed (a) and the open state (b). The observed trends agree.

8.4.11 STIFFNESS OF HSP90

I have described the kinetic transitions between the two global conformations, namely an open and a closed conformation. However, these global conformations depend on local dynamics within the respective global conformation. For Hsp90, it has been proposed that the closed conformation is rigid, but the open conformation might consist of an ensemble of several minor sub-conformations with fluctuations in the order of 2.5 *nm*. [60]

A bigger ensemble of sub-conformations in one global conformation would result in a wider distribution of extension profiles. This is inherent in our data because I can analyze the distance fluctuations within a global conformation. These fluctuation can then be quantified using the approach explained in **Section 5**. Briefly, I convert the fluctuation amplitude of the intensity signal to an extension potential that can be described by a Hookean function.

Since I have two global conformations, I first need to separate the fluctuations corresponding to each state. I perform this by using the threshold calculated by the Matlab function 'pulsewidth' (see Appendix **Figure 8.16A,B**).

For obtaining the fluctuations of the closed state, I delete all frames below the threshold (confer to red timetrace in Appendix **Figure 8.16B**) and for the open state (blue timetrace) I delete all fluctuations above the threshold. Strikingly, there are no extensions of Hsp90 in our timetrace in between the two global conformations confirming our model.

The corresponding extension potentials of the two conformations are shown in Appendix **Figure 8.16C**. Indeed, I clearly see, that the potential of the open conformation (blue) is wider than that of the closed conformation (red). Thus, the closed conformation is the stiffer conformation as expected. The stiffness constants for four individual Hsp90 proteins are extracted by parabolic fits to the individual potentials (see Appendix **Figure 8.16D**). Quantitatively, the spring or stiffness constant for Hsp90 is $12.7 \pm 0.2\, pN/nm$ in open conformation and $18.8 \pm 0.4\, pN/nm$ in closed conformation.

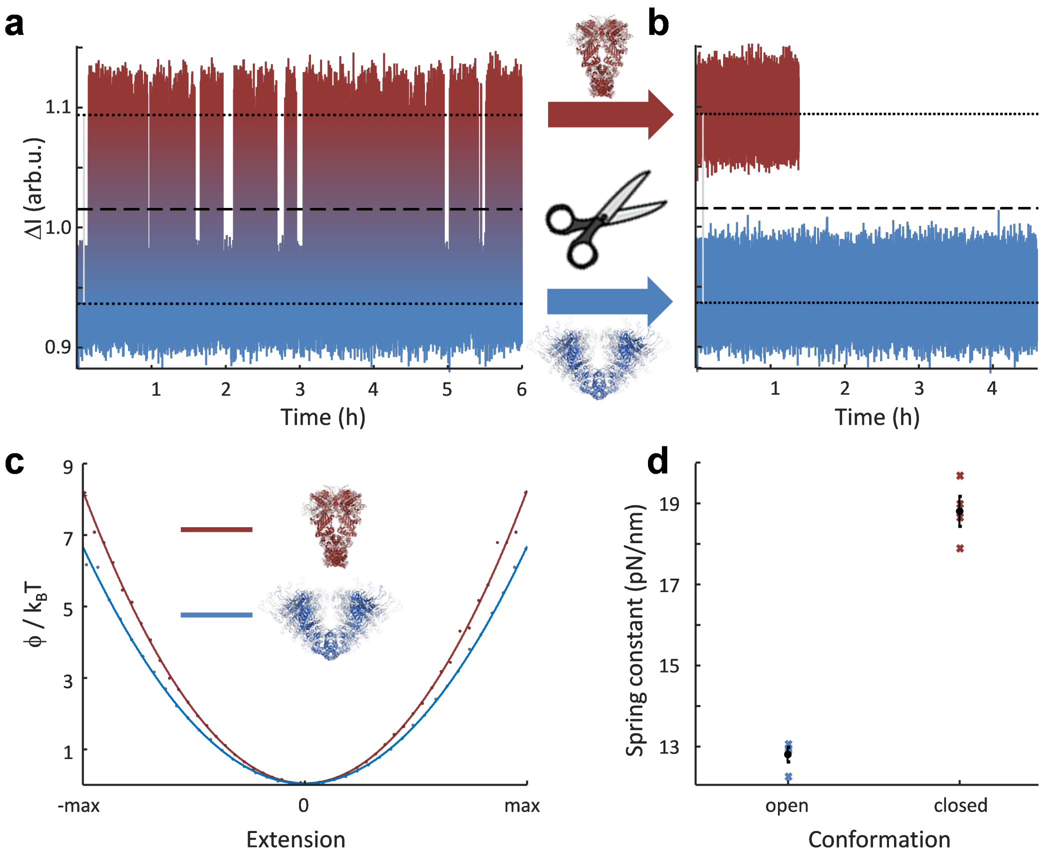

Figure 8.16: **Stiffness for Hsp90's closed and open conformation.** a) Timetrace of a fluctuating dimer. b) The extension fluctuations within each conformation, closed (red) and open (blue), are cut in two separate timetraces. c) Interparticle potential ϕ as a function of fluctuation (extension) around the equilibrium value. The values extracted from the probability functions for the particle separation are shown as dots, open conformation in blue and closed conformation in red. The measured values (dots) clearly follow two different trends as indicated by the fitted parabolas (lines in the corresponding colors). d) The spring constants calculated from the cut timetraces shown in 'b' for the two conformations measured on four individual plasmon rulers are shown as crosses. Their mean value solid is represented by a black dot with error bars corresponding to the error of the mean. Hsp90 sketch adapted with permission from [60].

9 REFERENCES

[1] Henzler-Wildman, K., and Kern, D. (2007) Dynamic personalities of proteins. *Nature 450*, 964.

[2] Jahn, M., Buchner, J., Hugel, T., and Rief, M. (2016) Folding and assembly of the large molecular machine Hsp90 studied in single-molecule experiments. *Proceedings of the National Academy of Sciences 113*, 1232.

[3] Mickler, M., Hessling, M., Ratzke, C., Buchner, J., and Hugel, T. (2009) The large conformational changes of Hsp90 are only weakly coupled to ATP hydrolysis. *Nature Structural and Molecular Biology 16*, 281.

[4] Sönnichsen, C., Reinhard, B. M., Liphardt, J., and Alivisatos, A. P. (2005) A molecular ruler based on plasmon coupling of single gold and silver nanoparticles. *Nature Biotechnology 23*, 741.

[5] Schultz, S., Smith, D. R., Mock, J. J., and Schultz, D. A. (2000) Single-target molecule detection with nonbleaching multicolor optical immunolabels. *Proceedings of the National Academy of Sciences 97*, 996.

[6] Reinhard, B. M., Sheikholeslami, S., Mastroianni, A., Alivisatos, A. P., and Liphardt, J. (2007) Use of plasmon coupling to reveal the dynamics of DNA bending and cleavage by single EcoRV restriction enzymes. *Proceedings of the National Academy of Sciences of the United States of America 104*, 2667.

[7] Chen, T., Hong, Y., and Reinhard, B. M. (2015) Probing DNA Stiffness through Optical Fluctuation Analysis of Plasmon Rulers. *Nano Letters 15*, 5349.

[8] Neher, E., and Sakmann, B. (1976) Single-channel currents recorded from membrane of denervated frog muscle fibres. *Nature 260*, 799.

[9] Sakmann, B. (1992) Elementary Steps in Synaptic Transmission Revealed by Currents through Single Ion Channels (Nobel Lecture). *Angewandte Chemie International Edition 31*, 830.

[10] Neuman, K. C., and Nagy, A. (2008) Single-molecule force spectroscopy: optical tweezers, magnetic tweezers and atomic force microscopy. *Nature Methods 5*, 491.

[11] Jarzynski, C. (1997) Nonequilibrium Equality for Free Energy Differences. *Physical Review Letters 78*, 2690.

[12] Rief, M., Gautel, M., Oesterhelt, F., Fernandez, J. M., and Gaub, H. E. (1997) Reversible Unfolding of Individual Titin Immunoglobulin Domains by AFM. *Science 276*, 1109.

[13] Tskhovrebova, L., Trinick, J., Sleep, J. A., and Simmons, R. M. (1997) Elasticity and unfolding of single molecules of the giant muscle protein titin. *Nature 387*, 308.

[14] Yu, H., Siewny, M. G. W., Edwards, D. T., Sanders, A. W., and Perkins, T. T. (2017) Hidden dynamics in the unfolding of individual bacteriorhodopsin proteins. *Science 355*, 945.

[15] Förster, T. (1948) Zwischenmolekulare Energiewanderung und Fluoreszenz. *Annalen der Physik 437*, 55.

[16] Förster, T. (1949) Experimentelle und theoretische Untersuchung des zwischenmolekularen Übergangs von Elektronenanregungsenergie. *Zeitschrift für Naturforschung A 4*, 321.

[17] Ha, T., Enderle, T., Ogletree, D. F., Chemla, D. S., Selvin, P. R., and Weiss, S. (1996) Probing the interaction between two single molecules: fluorescence resonance energy transfer between a single donor and a single acceptor. *Proceedings of the National Academy of Sciences 93*, 6264.

[18] Roy, R., Hohng, S., and Ha, T. (2008) A practical guide to single-molecule FRET. *Nature Methods 5*, 507.

[19] Jain, P. K., Huang, W., and El-Sayed, M. A. (2007) On the Universal Scaling Behavior of the Distance Decay of Plasmon Coupling in Metal Nanoparticle Pairs: A Plasmon Ruler Equation. *Nano Letters 7*, 2080.

[20] Jain, P. K., and El-Sayed, M. A. (2010) Plasmonic coupling in noble metal nanostructures. *Chemical Physics Letters 487*, 153.

[21] Skewis, L. R., and Reinhard, B. M. (2008) Spermidine modulated ribonuclease activity probed by RNA plasmon rulers. *Nano Letters 8*, 214.

[22] Morimura, H., Tanaka, S.-I., Ishitobi, H., Mikami, T., Kamachi, Y., Kondoh, H., and Inouye, Y. (2013) Nano-Analysis of DNA Conformation Changes Induced by Transcription Factor Complex Binding Using Plasmonic Nanodimers. *ACS Nano 7*, 10733.

[23] Qian, G.-S., Zhang, T.-T., Zhao, W., Xu, J.-J., and Chen, H.-Y. (2017) Single-molecule imaging of telomerase activity via linear plasmon rulers. *Chemical Communications 53*, 4710.

[24] Jun, Y.-W., Sheikholeslami, S., Hostetter, D. R., Tajon, C., Craik, C. S., and Alivisatos, A. P. (2009) Continuous imaging of plasmon rulers in live cells reveals early-stage caspase-3 activation at the single-molecule level. *Proceedings of the National Academy of Sciences of the United States of America 106*, 17735.

[25] Tajon, C. A., Seo, D., Asmussen, J., Shah, N., Jun, Y.-W., and Craik, C. S. (2014) Sensitive and Selective Plasmon Ruler Nanosensors for Monitoring the Apoptotic Drug Response in Leukemia. *ACS Nano 8*, 9199.

[26] Ament, I., Prasad, J., Henkel, A., Schmachtel, S., and Sönnichsen, C. (2012) Single Unlabeled Protein Detection on Individual Plasmonic Nanoparticles. *Nano Letters 12*, 1092.

[27] Rosman, C., Prasad, J., Neiser, A., Henkel, A., Edgar, J., and Sönnichsen, C. (2013) Multiplexed Plasmon Sensor for Rapid Label-Free Analyte Detection. *Nano Letters 13*, 3243.

[28] Lee, S. E., Chen, Q., Bhat, R., Petkiewicz, S., Smith, J. M., Ferry, V. E., Correia, A. L., Alivisatos, A. P., and Bissell, M. J. (2015) Reversible Aptamer-Au Plasmon Rulers for Secreted Single Molecules. *Nano Letters 15*, 4564.

[29] Rong, G., Wang, H., Skewis, L. R., and Reinhard, B. M. (2008) Resolving Sub-Diffraction Limit Encounters in Nanoparticle Tracking Using Live Cell Plasmon Coupling Microscopy. *Nano Letters 8*, 3386.

[30] Rong, G., Wang, H., and Reinhard, B. M. (2010) Insights from a Nanoparticle Minuet: Two-Dimensional Membrane Profiling through Silver Plasmon Ruler Tracking. *Nano Letters 10*, 230.

[31] Aaron, J., Travis, K., Harrison, N., and Sokolov, K. (2009) Dynamic Imaging of Molecular Assemblies in Live Cells Based on Nanoparticle Plasmon Resonance Coupling. *Nano Letters 9*, 3612.

[32] Wang, J., Yu, X., Boriskina, S. V., and Reinhard, B. M. (2012) Quantification of Differential ErbB1 and ErbB2 Cell Surface Expression and Spatial Nanoclustering through Plasmon Coupling. *Nano Letters 12*, 3231.

[33] Derjaguin, B., and Landau, L. (1941) Theory of the Stability of Strongly Charged Lyophobic Sols and of the Adhesion of Strongly Charged Particles in Solutions of Electrolytes. *Acta Phyicochimica URSS 14*, 633.

[34] Verwey, E. J. W., Overbeek, J. T. G., and van Nes, K. *Theory of the stability of lyophobic colloids : the interaction of sol particles having an electric double layer*; Elsevier: New York, 1948.

[35] Hamaker, H. (1937) The London-van der Waals attraction between spherical particles. *Physica 4*, 1058.

[36] Biggs, S., and Mulvaney, P. (1994) Measurement of the forces between gold surfaces in water by atomic force microscopy. *The Journal of Chemical Physics 100*, 8501.

[37] Moore, T. L., Rodriguez-Lorenzo, L., Hirsch, V., Balog, S., Urban, D., Jud, C., Rothen-Rutishauser, B., Lattuada, M., and Petri-Fink, A. (2015)

Nanoparticle colloidal stability in cell culture media and impact on cellular interactions. *Chemical Society Reviews 44*, 6287.

[38] Schneider, C. The Surface Charge of Soft and Hard Sphere Colloidal Particles - Experimental Investigation and Comparison to Theory. Ph.D. thesis, Bayreuth, 2010.

[39] Israelachvili, J. N. *Intermolecular and Surface Forces*, 3rd ed.; Academic Press: New York, 2011.

[40] Grahame, D. C. (1947) The Electrical Double Layer and the Theory of Electrocapillarity. *Chemical Reviews 41*, 441.

[41] Zheng, Y., Rosa, L., Thai, T., Ng, S. H., Gomez, D. E., Ohshima, H., and Bach, U. (2015) Asymmetric gold nanodimer arrays: electrostatic self-assembly and SERS activity. *Journal of Materials Chemistry A 3*, 240.

[42] López-Esparza, R., Balderas Altamirano, M. A., Pérez, E., and Gama Goicochea, A. (2015) Importance of Molecular Interactions in Colloidal Dispersions. *Advances in Condensed Matter Physics 2015*, 8.

[43] Prodan, E., Radloff, C., Halas, N. J., and Nordlander, P. (2003) A Hybridization Model for the Plasmon Response of Complex Nanostructures. *Science 302*, 419.

[44] Reinhard, B. M., Siu, M., Agarwal, H., Alivisatos, A. P., and Liphardt, J. (2005) Calibration of Dynamic Molecular Rulers Based on Plasmon Coupling between Gold Nanoparticles. *Nano Letters 5*, 2246.

[45] Lambertz, C., Martos, A., Henkel, A., Neiser, A., Kliesch, T.-T., Janshoff, A., Schwille, P., and Sönnichsen, C. (2016) Single Particle Plasmon Sensors as Label-Free Technique To Monitor MinDE Protein Wave Propagation on Membranes. *Nano Letters 16*, 3540.

[46] Khalavka, Y., Becker, J., and Sönnichsen, C. (2009) Synthesis of Rod-Shaped Gold Nanorattles with Improved Plasmon Sensitivity and Catalytic Activity. *Journal of the American Chemical Society 131*, 1871.

[47] Hohenester, U., and Trügler, A. (2012) MNPBEM - A Matlab toolbox for the simulation of plasmonic nanoparticles. *Computer Physics Communications 183*, 370.

[48] Johnson, P. B., and Christy, R. W. (1972) Optical Constants of the Noble Metals. *Physical Review B 6*, 4370.

[49] Kuzuya, A., Numajiri, K., Kimura, M., and Komiyama, M. (2008) Single-molecule accommodation of streptavidin in nanometer-scale wells formed in DNA nanostructures. *Nucleic Acids Symposium Series 52*, 681.

[50] Beskorovaynyy, A. V., Kopitsyn, D. S., Novikov, A. A., Ziangirova, M., Skorikova, G. S., Kotelev, M. S., Gushchin, P. A., Ivanov, E. V., Getmansky, M. D., Itzkan, I., Muradov, A. V., Vinokurov, V. A., and Perelman, L. T. (2014) Rapid Optimization of Metal Nanoparticle Surface Modification with High-Throughput Gel Electrophoresis. *ACS Nano 8*, 1449.

[51] Tüting, L., Ye, W., Settanni, G., Schmid, F., Wolf, B. A., Ahijado-Guzmán, R., and Sönnichsen, C. (2017) Potassium Triggers a Reversible Specific Stiffness Transition in Polyethylene Glycol. *Journal of Physical Chemistry C 121*, 22396.

[52] Alberts, B. (1998) The Cell as a Collection of Protein Machines: Preparing the Next Generation of Molecular Biologists. *Cell 92*, 291.

[53] Prasad, J. Sensing Applications of Biofunctionalised Plasmonic Gold Nanoparticles. Ph.D. thesis, Mainz, 2014.

[54] Häkkinen, H. (2012) The gold-sulfur interface at the nanoscale. *Nature Chemistry 4*, 443.

[55] Hinterdorfer, P., and Dufrêne, Y. F. (2006) Detection and localization of single molecular recognition events using atomic force microscopy. *Nature Methods 3*, 347.

[56] Hermanson, G. T. *Bioconjugate Techniques;* Academic Press: San Diego, 1996.

[57] Cha, H., Yoon, J. H., and Yoon, S. (2014) Probing Quantum Plasmon Coupling Using Gold Nanoparticle Dimers with Tunable Interparticle Distances Down to the Subnanometer Range. *ACS Nano 8*, 8554.

[58] Zhou, Y., Wang, S., Zhang, K., and Jiang, X. (2008) Visual Detection of Copper(II) by Azide- and Alkyne-Functionalized Gold Nanoparticles Using Click Chemistry. *Angewandte Chemie International Edition 47*, 7454.

[59] Bouhouche-Chatelier, I., Chadli, A., and Catelli, M.-G. (2001) The N-terminal adenosine triphosphate binding domain of Hsp90 is necessary and sufficient for interaction with estrogen receptor. *Cell Stress & Chaperones 6*, 297.

[60] Hellenkamp, B., Wortmann, P., Kandzia, F., Zacharias, M., and Hugel, T. (2017) Multidomain structure and correlated dynamics determined by self-consistent FRET networks. *Nature Methods 14*, 174.

[61] Diamandis, E. P., and Christopoulos, T. K. (1991) The Biotin-(Strept)avidin System: Principles and Applications in Biotechnology. *Clinincal Chemistry 37*, 625.

[62] Caswell, K. K., Wilson, J. N., Bunz, U. H. F., and Murphy, C. J. (2003) Preferential End-to-End Assembly of Gold Nanorods by Biotin-Streptavidin Connectors. *Journal of the American Chemical Society 125*, 13914.

[63] Deng, L., Kitova, E. N., and Klassen, J. S. (2013) Dissociation Kinetics of the Streptavidin-Biotin Interaction Measured Using Direct Electrospray Ionization Mass Spectrometry Analysis. *Journal of The American Society for Mass Spectrometry 24*, 49.

[64] Chen, G., Dubrawsky, I., Mendez, P., Georgiou, G., and Iverson, B. L. (1999) In vitro scanning saturation mutagenesis of all the specificity determining residues in an antibody binding site. *Protein Engineering Design & Selection 12*, 349.

[65] Nieba, L., Nieba-Axmann, S. E., Persson, A., Hämäläinen, M., Edebratt, F., Hansson, A., Lidholm, J., Magnusson, K., Frostell-Karlsson, A., and

Plückthun, A. (1997) BIACORE Analysis of Histidine-Tagged Proteins Using a Chelating NTA Sensor Chip. *Analytical Biochemistry 252*, 217.

[66] Tinoco, I., and Gonzalez, R. L. (2011) Biological mechanisms, one molecule at a time. *Genes & Development 25*, 1205.

[67] Berquand, A., Xia, N., Castner, D. G., Clare, B. H., Abbott, N. L., Dupres, V., Adriaensen, Y., and Dufrêne, Y. F. (2005) Antigen Binding Forces of Single Antilysozyme Fv Fragments Explored by Atomic Force Microscopy. *Langmuir 21*, 5517.

[68] Robinson, A., and van Oijen, A. M. (2013) Bacterial replication, transcription and translation: mechanistic insights from single-molecule biochemical studies. *Nature Reviews Microbiology 11*, 303.

[69] Larson-Smith, K., and Pozzo, D. C. (2012) Competitive Adsorption of Thiolated Poly(ethylene glycol) and Alkane-Thiols on Gold Nanoparticles and Its Effect on Cluster Formation. *Langmuir 28*, 13157.

[70] Schulz, F., Dahl, G. T., Besztejan, S., Schroer, M. A., Lehmkühler, F., Grübel, G., Vossmeyer, T., and Lange, H. (2016) Ligand Layer Engineering To Control Stability and Interfacial Properties of Nanoparticles. *Langmuir 32*, 7897.

[71] Hanauer, M., Pierrat, S., Zins, I., Lotz, A., and Sönnichsen, C. (2007) Separation of Nanoparticles by Gel Electrophoresis According to Size and Shape. *Nano Letters 7*, 2881.

[72] Claridge, S. A., Liang, H. W., Basu, S. R., Fréchet, J. M. J., and Alivisatos, A. P. (2008) Isolation of Discrete Nanoparticle-DNA Conjugates for Plasmonic Applications. *Nano Letters 8*, 1202.

[73] Duchesne, L., Gentili, D., Comes-Franchini, M., and Fernig, D. G. (2008) Robust Ligand Shells for Biological Applications of Gold Nanoparticles. *Langmuir 24*, 13572.

[74] Steinigeweg, D., Schütz, M., Salehi, M., and Schlücker, S. (2011) Fast and Cost-Effective Purification of Gold Nanoparticles in the 20-250 nm Size Range by Continuous Density Gradient Centrifugation. *Small 7*, 2443.

[75] Schwille, P., and Haustein, E. *Fluorescence Correlation Spectroscopy: An Introduction to its Concepts and Applications*; Biophysics Textbook online, 2002.

[76] Lide, D. R., Ed. *Handbook of Chemistry & Physics*, 65th ed.; CRC Press, 2002.

[77] Bürgi, T. (2015) Properties of the gold-sulphur interface: from self-assembled monolayers to clusters. *Nanoscale 7*, 15553.

[78] Kim, K. H. et al. (2015) Direct observation of bond formation in solution with femtosecond X-ray scattering. *Nature 518*, 385.

[79] Haycock, J. (1993) Polyvinylpyrrolidone as a Blocking Agent in Immunochemical Studies. *Analytical Biochemistry 208*, 397.

[80] Schenk, F. C., Boehm, H., Spatz, J. P., and Wegner, S. V. (2014) Dual-Functionalized Nanostructured Biointerfaces by Click Chemistry. *Langmuir 30*, 6897.

[81] Osinkina, L., Carretero-Palacios, S., Stehr, J., Lutich, A. A., Jäckel, F., and Feldmann, J. (2013) Tuning DNA Binding Kinetics in an Optical Trap by Plasmonic Nanoparticle Heating. *Nano Letters 13*, 3140.

[82] Sebba, D. S., Mock, J. J., Smith, D. R., LaBean, T. H., and Lazarides, A. A. (2008) Reconfigurable Core-Satellite Nanoassemblies as Molecularly-Driven Plasmonic Switches. *Nano Letters 8*, 1803.

[83] Chen, J. I. L., Chen, Y., and Ginger, D. S. (2010) Plasmonic Nanoparticle Dimers for Optical Sensing of DNA in Complex Media. *Journal of the American Chemical Society 132*, 9600.

[84] Guo, L., Ferhan, A. R., Chen, H., Li, C., Chen, G., Hong, S., and Kim, D. H. (2013) Distance-Mediated Plasmonic Dimers for Reusable Colorimetric Switches: A Measurable Peak Shift of More than 60 nm. *Small 9*, 234.

[85] Zhang, Y., Zhu, C., Zhang, L., Tan, C., Yang, J., Chen, B., Wang, L., and Zhang, H. (2015) DNA-Templated Silver Nanoclusters for Multiplexed Fluorescent DNA Detection. *Small 11*, 1385.

[86] Bikard, D., Loot, C., Baharoglu, Z., and Mazel, D. (2010) Folded DNA in Action: Hairpin Formation and Biological Functions in Prokaryotes. *Microbiology and Molecular Biology Reviews 74*, 570.

[87] Neish, C. S., Martin, I. L., Henderson, R. M., and Edwardson, J. M. (2002) Direct visualization of ligand-protein interactions using atomic force microscopy. *British Journal of Pharmacology 135*, 1943.

[88] Harris, J. *Poly (ethylene glycol) Chemistry: Biotechnical and Biomedical Applications*; Plenum Press: New York, 1992.

[89] Zalipsky, S., and Harris, J. *Poly (ethylene glycol) Chemistry and Biological Applications*; American Chemical Society: ACS Symposium Series 680: Washingtion, DC, 1997.

[90] Chen, J., Spear, S. K., Huddleston, J. G., and Rogers, R. D. (2005) Polyethylene Glycol and Solutions of Polyethylene Glycol as Green Reaction Media. *Green Chemistry 7*, 64.

[91] Rogers, R. D., Bond, A. H., Aguinaga, S., and Reyes, A. (1992) Complexation Chemistry of Bismuth (III) Halides with Crown Ethers and Polyethylene Glycols. Structural Manifestations of a Stereochemically Active Lone Pair. *Journal of the American Chemical Society 114*, 2967.

[92] Terashima, T., Kawabe, M., Miyabara, Y., Yoda, H., and Sawamoto, M. (2013) Polymeric Pseudo-Crown Ether for Cation Recognition Via Cation Template-Assisted Cyclopolymerization. *Nature Communications 4*, 2321.

[93] Xiong, X., and Wolf, B. A. (2014) Intrinsic Viscosities of Polyelectrolytes: Specific Salt Effects and Viscometric Master Curves. *Soft Matter 10*, 2124.

[94] Mura, S., Nicolas, J., and Couvreur, P. (2013) Stimuli-Responsive Nanocarriers for Drug Delivery. *Nature Materials 12*, 991.

[95] Stuart, M. A. C., Huck, W. T. S., Genzer, J., Mueller, M., Ober, C., Stamm, M., Sukhorukov, G. B., Szleifer, I., Tsukruk, V. V., Urban, M., Winnik, F., Zauscher, S., Luzinov, I., and Minko, S. (2010) Emerging Applications of Stimuli-Responsive Polymer Materials. *Nature Materials 9*, 101.

[96] Goodman, C. M., Choi, S., Shandler, S., and DeGrado, W. F. (2007) Foldamers as Versatile Frameworks for the Design and Evolution of Function. *Nature Chemical Biology 3*, 252.

[97] Gellman, S. H. (1998) Foldamers: A Manifesto. *Accounts of Chemical Research 31*, 173.

[98] Weiss, S. (1999) Fluorescence Spectroscopy of Single Biomolecules. *Science 283*, 1679.

[99] Viani, M. B., Schäffer, T. E., Chand, A., Rief, M., Gaub, H. E., and Hansma, P. K. (1999) Small Cantilevers for Force Spectroscopy of Single Molecules. *Journal of Applied Physics 86*, 2258.

[100] Hanske, C., González-Rubio, G., Hamon, C., Formentín, P., Modin, E., Chuvilin, A., Guerrero-Martínez, A., Marsal, L. F., and Liz-Marzán, L. M. (2017) Large-Scale Plasmonic Pyramidal Supercrystals via Templated Self-Assembly of Monodisperse Gold Nanospheres. *Journal of Physical Chemistry C 121*, 10899.

[101] Pierrat, S., Zins, I., Breivogel, A., and Sönnichsen, C. (2007) Self-Assembly of Small Gold Colloids with Functionalized Gold Nanorods. *Nano Letters 7*, 259.

[102] Dill, K. A., and Bromberg, S. *Molecular driving forces: statistical thermodynamics in chemistry, physics, biology, and nanoscience*, 2nd ed.; Garland Science: New York, 2011.

[103] Sulchek, T. A., Friddle, R. W., Langry, K., Lau, E. Y., Albrecht, H., Ratto, T. V., DeNardo, S. J., Colvin, M. E., and Nox, A. (2005) Dynamic Force Spectroscopy of Parallel Individual Mucin1-Antibody Bonds. *Proceedings of the National Academy of Sciences 102*, 16638.

[104] Yizhak, M. (1991) Thermodynamics of Solvation of Ions. Part 5. - Gibbs Free Energy of Hydration at 298.15 K. *Journal of the Chemical Society, Faraday Transactions 87*, 2995.

[105] Pedersen, C. J. (1967) Cyclic Polyethers and Their Complexes with Metal Salts. *Journal of the American Chemical Society 89*, 7010.

[106] Boehr, D. D., Nussinov, R., and Wright, P. E. (2009) The role of dynamic conformational ensembles in biomolecular recognition. *Nature Chemical Biology 5*, 789.

[107] Zierer, B., Rübbelke, M., Tippel, F., Madl, T., Schopf, F., Rutz, D., Richter, K., Sattler, M., and Buchner, J. (216) Importance of cycle timing for the function of the molecular chaperone Hsp90. *Nature Structural & Molecular Biology 23*, 1020.

[108] Zhuang, X., and Rief, M. (2003) Single-molecule folding. *Current Opinion in Structural Biology 13*, 88.

[109] Tüting, L., Ye, W., Götz, M., Celiksoy, S., Ahijado-Guzmán, R., Hugel, T., and Sönnichsen, C. (2017) Conformational Dynamics of a Single Protein Monitored for 24hrs at Video Rate. *in preparation*

[110] Miyata, Y., Nakamoto, H., and Neckers, L. (2013) The therapeutic target Hsp90 and cancer hallmarks. *Current Pharmaceutical Design 19*, 347.

[111] Whitesell, L., and Lindquist, S. (2005) HSP90 and the chaperoning of cancer. *Nature Reviews Cancer 5*, 761.

[112] Richter, K., and Buchner, J. (2006) hsp90: Twist and Fold. *Cell 127*, 251.

[113] Höök, F., Rodahl, M., Kasemo, B., and Brzezinski, P. (1998) Structural changes in hemoglobin during adsorption to solid surfaces: Effects of pH, ionic strength, and ligand binding. *Proceedings of the National Academy of Sciences 95*, 12271.

[114] Beuwer, M. A., Prins, M. W., and Zijlstra, P. (2015) Stochastic protein interactions monitored by hundreds of single-molecule plasmonic biosensors. *Nano Letters 15*, 3507.

[115] Ratzke, C., Mickler, M., Hellenkamp, B., Buchner, J., and Hugel, T. (2010) Dynamics of heat shock protein 90 C-terminal dimerization is an important part of its conformational cycle. *Proceedings of the National Academy of Sciences 107*, 16101.

[116] Schmid, S., Götz, M., and Hugel, T. (2016) Single-Molecule Analysis beyond Dwell Times: Demonstration and Assessment in and out of Equilibrium. *Biophysical Journal 111*, 1375.

[117] Landowne, D., Yuan, B., and Magleby, K. (2013) Exponential Sum-Fitting of Dwell-Time Distributions without Specifying Starting Parameters. *Biophysical Journal 104*, 2383.

[118] Zhang, X., Servos, M., and Liu, J. (2012) Instantaneous and Quantitative Functionalization of Gold Nanoparticles with Thiolated DNA Using a pH-Assisted and Surfactant-Free Route. *Journal of the American Chemical Society 134*, 7266.

[119] Hugel, T., Michaelis, J., Hetherington, C., Jardine, P., Grimes, S., Walter, J., Falk, W., Anderson, D., and Bustamante, C. (2007) Experimental Test of Connector Rotation during DNA Packaging into Bacteriophage 29 Capsids. *PLoS Biology 5*, 558.

[120] Geerissen, H., Schmidt, J. R., and Wolf, B. A. (1982) On the Factors Governing the Pressure Dependence of the Viscosity of Moderately Concentrated Polymer Solutions. *Journal of Applied Polymer Science 27*, 1277.

[121] MacKerell, A. D. et al. (1998) All-atom empirical potential for molecular modeling and dynamics studies of proteins. *Journal of Physical Chemistry B 102*, 3586.

[122] MacKerell, A. D., Feig, M., and Brooks, C. L. (2004) Extending the treatment of backbone energetics in protein force fields: limitations of gas-

phase quantum mechanics in reproducing protein conformational distributions in molecular dynamics simulations. *Journal of Computational Chemistry 25*, 1400.

[123] Lee, H., Venable, R. M., Mackerell, A. D., and Pastor, R. W. (2008) Molecular Dynamics Studies of Polyethylene Oxide and Polyethylene Glycol: Hydrodynamic Radius and Shape Anisotropy. *Biophysical Journal 95*, 1590.

[124] Jorgensen, W. L., Chandrasekhar, J., Madura, J. D., Impey, R. W., and Klein, M. L. (1983) Comparison of simple potential functions for simulating liquid water. *The Journal of Chemical Physics 79*, 926.

[125] Martyna, G. J., Tobias, D. J., and Klein, M. L. (1994) Constant pressure molecular dynamics algorithms. *The Journal of Chemical Physics 101*, 4177.

[126] Feller, S. E., Zhang, Y., Pastor, R. W., and Brooks, B. R. (1995) Constant pressure molecular dynamics simulation: The Langevin piston method. *The Journal of Chemical Physics 103*, 4613.

[127] Essmann, U., Perera, L., and Berkowitz, M. L. (1995) A smooth particle mesh Ewald method. *The Journal of Chemical Physics 103*, 8577.

[128] Wang, L., Friesner, R. A., and Berne, B. J. (2011) Replica Exchange with Solute Scaling: A More Efficient Version of Replica Exchange with Solute Tempering (REST2). *Journal of Physical Chemistry B 115*, 9431.

[129] Jo, S., and Jiang, W. (2015) A generic implementation of replica exchange with solute tempering (REST2) algorithm in NAMD for complex biophysical simulations. *Computer Physics Communications 197*, 304.

[130] Seeber, M., Cecchini, M., Rao, F., Settanni, G., and Caflisch, A. (2007) Wordom: a program for efficient analysis of molecular dynamics simulations. *Bioinformatics 23*, 2625.

[131] Humphrey, W., Dalke, A., and Schulten, K. (1996) VMD: visual molecular dynamics. *Journal of Molecular Graphics 14*, 33.

[132] Yang, W., and Gruebele, M. (2003) Folding at the speed limit. *Nature 423*, 193.